Electronic Thesis and Dissertation Repository

6-18-2013 12:00 AM

Application of RADARSAT-2 Polarimetric Data for Land Use and Land Cover Classification and Crop monitoring in Southwestern Ontario

Qin Ma
The University of Western Ontario

Supervisor
Jinfei Wang
The University of Western Ontario

Graduate Program in Geography
A thesis submitted in partial fulfillment of the requirements for the degree in Master of Science
© Qin Ma 2013

Follow this and additional works at: https://ir.lib.uwo.ca/etd

Part of the Remote Sensing Commons

APPLICATION OF RADARSAT-2 POLARIMETRIC DATA FOR LAND USE AND LAND COVER CLASSIFICATION AND CROP MONITORING IN SOUTHWESTERN ONTARIO

(Thesis format: Integrated Article)

by

Qin <u>Ma</u>

Graduate Program in Geography

A thesis submitted in partial fulfillment
of the requirements for the degree of
Master of Science

The School of Graduate and Postdoctoral Studies
The University of Western Ontario
London, Ontario, Canada

Abstract

Timely and accurate information of land surfaces is desirable for land change detection and crop condition monitoring. Optical data have been widely used in Land Use and Land Cover (LU/LC) mapping and crop condition monitoring. However, due to unfavorable weather conditions, high quality optical images are not always available. Synthetic Aperture Radar (SAR) sensors, such as RADARSAT-2, are able to transmit microwaves through cloud cover and light rain, and thus offer an alternative data source.

This study investigates the potential of multi-temporal polarimetric RADARSAT-2 data for LU/LC classification and crop monitoring in the urban rural fringe areas of London, Ontario. Nine LU/LC classes were identified with a high overall accuracy of 91.0%. Also, high correlations have been found within the corn and soybean fields between some polarimetric parameters and Normalized Difference Vegetation Index (NDVI). The results demonstrate the capability of RADARSAT-2 in LU/LC classification and crop condition monitoring.

Keywords

Acknowledgments

First, I would like to thank my supervisor, Dr. Jinfei Wang. She helped me from the very beginning with developing the research topic, looking for the data and software for the project, planning and conducting the field work, and the final thesis writing. I benefited greatly from her instruction in Remote Sensing courses, her thoughtful advice and constructive criticisms of my research. Her passion in research and education, as well as her modest and nice personality has inspired me to be a better researcher.

Second, thanks to Dr. Jiali Shang from the Agriculture and Agri-food Canada for her support in providing the RapidEye images and RADARSAT-2 data for this research. Her suggestions of research design and valuable comments about paper writing were invaluable.

I would also like to thank all the people in our lab, Chuiqing Zeng, Ting Zhao, Nicholas Lantz, Autumn Gambles, and Francisco Flores de Santiago for supporting and encouraging me over the two years of study and research. The visiting professor Wen Dou from Southeastern University, China provided helpful suggestions and encouragement when I encountered some problems in my research. It was those inspiring and intelligent chatting with him and his family that helped me get through the hard time. Also, thanks to visiting PhD Peng Wang from Chinese Academy of Sciences, who guided me in the study of microwave and SAR data processing techniques. Great appreciate to Autumn Gambles for helping me with thesis final editing. In addition, thanks to Kathy Tang for driving us out to the fields in the hot summer of 2012.

Finally, I would like to thank my family and boyfriend for their support and encouragement throughout my study in a foreign country. Their endless conversations about my study and life from my home country have brought me with warmth and hope. I am very grateful to have such wonderful people in my life. Without your love, I would not have been able to accomplish my Master's Thesis.

Table of Contents

List of Tables

List of Figures

Chapter 1

1   Introduction

1.1   Research Content

Agriculture is an important element of the Canadian economy; as such, Canada has become one of the largest agricultural producers and exporters in the world. However, the proportion of the population and GDP devoted to agriculture has fallen dramatically over the past few decades.

Due to the rapid urban development in Ontario, the impact of urban development on the agricultural economy is evident. In the decade from 1981 to 1990, the net farm income in Ontario was 6,812 million CAD, which was 23% of the net farm income in Canada. In contrast, net farm income decreased to 2,891 million CAD from 2001 to 2010, which occupied merely 11% of the net farm income in the whole country (Statistics Canada, 2012). A report given by Statistic Canada showed that from 2006 to 2011, the number of farms decreased by 9.2%. During this timeframe, the total area occupied by farms also dropped by 4.8%.

In Southern Ontario alone, hundreds of square kilometers of productive agricultural land are lost due to the rapid urban sprawl each year. For example, in the Greater Toronto Area, over 2,000 farms and 500 km^2 of farmland were converted to urban purposes between 1976 and 1996 (OMAFRA, 2011).

The rapid loss of agricultural areas to urban land use in the urban/rural fringe area in regions similar to Southern Ontario, has raised great concern. Increasingly, researchers have focused on assessing the impacts of urban expansion on agricultural and forest ecosystems (Lombard et al. 2003; Pellizzeri 2003; Pellizzeri et al. 2003; Niu and Ban 2010; Zhang et al. 2010; Zhu et al.2011).

Remote Sensing offers an effective solution to detect changes over land surfaces. Satellite sensors are able to collect up-to-date and reliable information about the current state of land surfaces, with such features as wide area coverage and a short revisit interval. This data if then used to further facilitate Land Use and Land Cover (LU/LC) change detection, as well as agricultural condition monitoring.

The complexity of urban/rural fringe environments makes LU/LC mapping very challenging, as they are composed of a wide variety of LU/LC classes. However, optical images have been proven to be promising data sources, due to the rich informational content of multispectral data. Since the launch of Landsat optical satellites, many LU/LC mapping applications have utilized optical remote sensing data. With the advent of advanced optical satellite sensors (i.e. Quickbird, Ikonos, SPOT, Worldview, and RapidEye), the spectral and spatial resolution of images have been highly improved (Corbane et al., 2008). More sophisticated methods, such as object-based classification, have been developed to improve the classification accuracy (Geneletti & Gorte, 2003; Gao et al., 2006; Li et al., 2008; Li et al., 2009; Qi et al., 2012; Watts et al., 2009).

Multi-temporal Remote Sensing information is particularly useful in agricultural applications, such as annual crop inventory and crop condition monitoring (Defries & Townshend, 1994; Friedl et al., 2010; Gopal et al., 1999; Guerschman et al., 2003; Hansen et al., 2000; Tucker et al.,1985; Wolter et al., 1995). The bio-physical characteristics of vegetation, such as pigmentation, internal leaf structure and moisture, vary from crop to crop and reflect crop development over time. The changes in the biophysical characteristics can be directly reflected by the amount of visible and infrared (V-IR) energy recorded on the satellite images (Reese et al., 2002; Guerschman et al., 2003; Turker and Arikan, 2005; Fisette et al., 2005). A large number of vegetation indices (i.e. the normalized difference vegetation index (NDVI), the optimized soil adjusted vegetation index, the enhanced vegetation index, and the modified triangular vegetation index) are derived from multispectral optical data in order to track temporal changes in biophysical characteristics of different vegetation types (Andrés et al., 2011).

LU/LC change detection and crop condition monitoring applications using optical images are successful only when images can be acquired frequently over the entire crop growth period. However, due to the existence of haze and cloud, high quality optical data are not always available under unfavorable weather conditions. Therefore, when time and area gaps in data acquisition occur, the application potentials of optical images are often limited (McNairn et. al., 2009). In contrast, remote sensing satellites using RADAR technology employ microwaves, which are able to transmit through most cloud and haze. Thus, the backscattering signals obtained using RADAR remote sensing satellites are less influenced by weather conditions. The Synthetic Aperture Radar system, which transmits and receives microwave signals, provides complementary information for optical remote sensing. The backscattering signals from SAR are sensitive to the architecture and dielectric properties of land surfaces, such as plant canopy, built-up and soils (McNairn et. al., 2009).

The advantages of SAR images over optical data are more obvious in agricultural applications, as crops change rapidly during their growing seasons. The resulting SAR backscatter signals are primarily a function of the canopy structure such as the size, shape and orientation of leaves, stalks and fruit, the water content of the crop canopy and the soil conditions. However, the structure and water content varies from crop to crop and changes among different stages of crop development. Therefore, SAR images have the potential to not only distinguish different crop types, but also to monitor crop growing conditions. During the past few years, many studies have proved the capabilities of SAR data in crop condition monitoring and biophysical parameter retrieval (Blaes et al., 2005; Chakraborty et al., 2005; Moran et al., 1997; Nicolas et al., 2009; Shao et al., 2001).

Studies show that the sensitivity of SAR backscattering to crop conditions depends on the SAR sensor parameters (wavelength, incidence angles, and polarization). Generally, short SAR wavelengths, such as X-band (~3cm) and C-band (~6cm), are less capable to penetrate through the canopy, and therefore mainly interact with the top part of the canopy layers. In contrast, longer wavelengths such as L-band (~20cm) and P-band (~100cm) can penetrate into the vegetation cover and even reach the soil (Ulaby et al., 1987). The penetration depth achieved depends on the biophysical parameters of the objects causing scatter within a vegetation layer (e.g., water content, size and geometry of the scatter

objects), which might enhance or attenuate the interactions between microwaves and scatter- producing features.

In addition to exploring the frequency dimension of the SAR system, some researchers have investigated the polarimetric properties of SAR data in LU/LC classification and vegetation monitoring. (Pierce et al., 1994; Du & Lee, 1996; Lee et al., 2001; Freitas et al., 2008). Results indicate that, by utilizing polarimetric SAR instead of single polarization data, higher accuracy can be achieved in both LU/LC mapping and crop monitoring. With the recent launch of radar satellites, such as ENVISAT ASAR, ALOS PALSAR, RADARSAT-2 and TERRASAR-X, more polarimetric SAR data are becoming available. Congruently, some polarimetric decomposition theorems have been developed and applied (Cloude & Pottier, 1996; Freeman &Durden, 1998; Yang et al., 1998; Cameron & Rais, 2006), which provide additional information for LU/LC classification and crop monitoring. The decomposition parameters extracted from polarimetric SAR data are related to the physical properties of land surfaces, and are thus sensitive to the structures of different LU/LC types and crops in various stages. However, the potential of polarimetric decomposition parameters in LU/LC classification and crop growing conditions monitoring, is not fully explored in the current research literature (Liu et al., 2012).

1.2 Research Objectives

The objectives of this research are to evaluate the multi-temporal Quadpol RADARSAT-2 data for usage in LU/LC mapping and crop monitoring applications in Southwestern Ontario. As mentioned above, rapid urban sprawl has greatly influenced the agricultural economy and overall crop productivity in this area. However, multitemporal polarimetric SAR data have seldom been used in this agricultural area before. The newly available RADARSAT-2 data provide an opportunity to study the impacts of urban development on agriculture in Southwestern Ontario.

The research objectives of this thesis will seek to provide answers to the following questions:

1. How accurately can LU/LC be classified in this urban/rural fringe area using the fine beam multi-temporal polarimetric RADARSAT-2 satellite images?

2. What is a good classification method for LU/LC classification in urban/rural fringe areas using polarimetric RADARSAT-2 satellite images?

3. What is a suitable multi-date combination of polarimetric RADARSAT-2 images in LU/LC classification?

4. What is the potential of polarimetric RADARSAT-2 data for monitoring crop height changes?

5. How sensitive are RADARSAT-2 polarimetric parameters to crop biophysical parameters, such as NDVI?

The studies presented in Chapter 2 and Chapter 3 answer these questions by addressing these research objectives:

1. To assess the potential of polarimetric RADARSAT-2 data in LU/LC classification in urban/rural fringe areas, from the aspects of classification method, polarimetric parameters selection, and multi-temporal data combination.

2. To analyze the sensitivity of different RADARSAT-2 polarimetric parameters to the temporal changes of crop height and NDVI.

1.3 Study Area and Data

The study area is located in the urban/rural fringe area of London, Ontario (Figure 1.1). The City of London is within the Middlesex County right at the forks of the non-navigable Thames River. London is well-known for its tree-lined boulevards, and is consequently known as the "Forest City" after that. The city is situated along the Quebec City-Windsor Corridor, approximately halfway between Toronto, Ontario and Detroit, Michigan. In 2011, there were approximately 366,151 residents in the city within an area of approximately 420 square kilometers (Statistics Canada, 2012). In terms of economy, London is dominated by high education, medical research, insurance, and information

technology sectors (Service Canada, 2009). The main crops growing in the adjacent rural area are wheat, corn, soybeans, hay, and field peas.
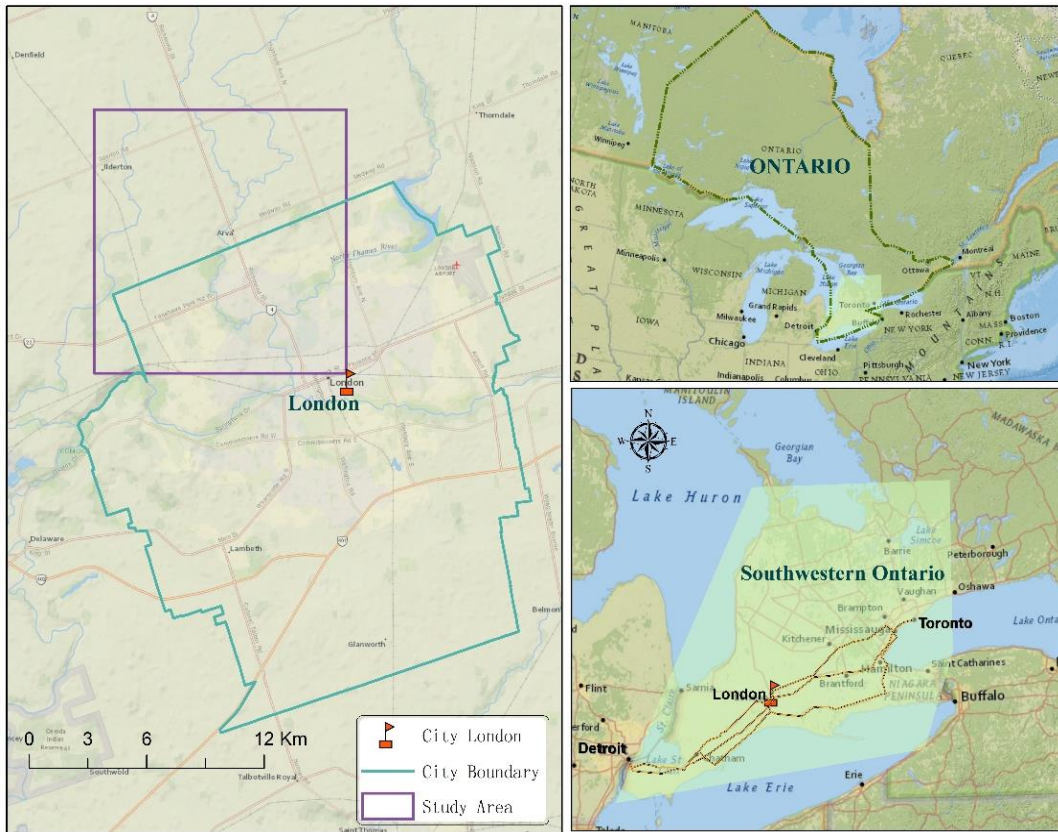
Figure 1.1 Study Area

The satellite images used in the research include RADARSAT-2 SAR images and RapidEye optical images. The boundaries of satellite images and study areas are displayed in Figure 1.2. Other ancillary data, such as images from Google Earth, and air photo images are also used to facilitate the research.
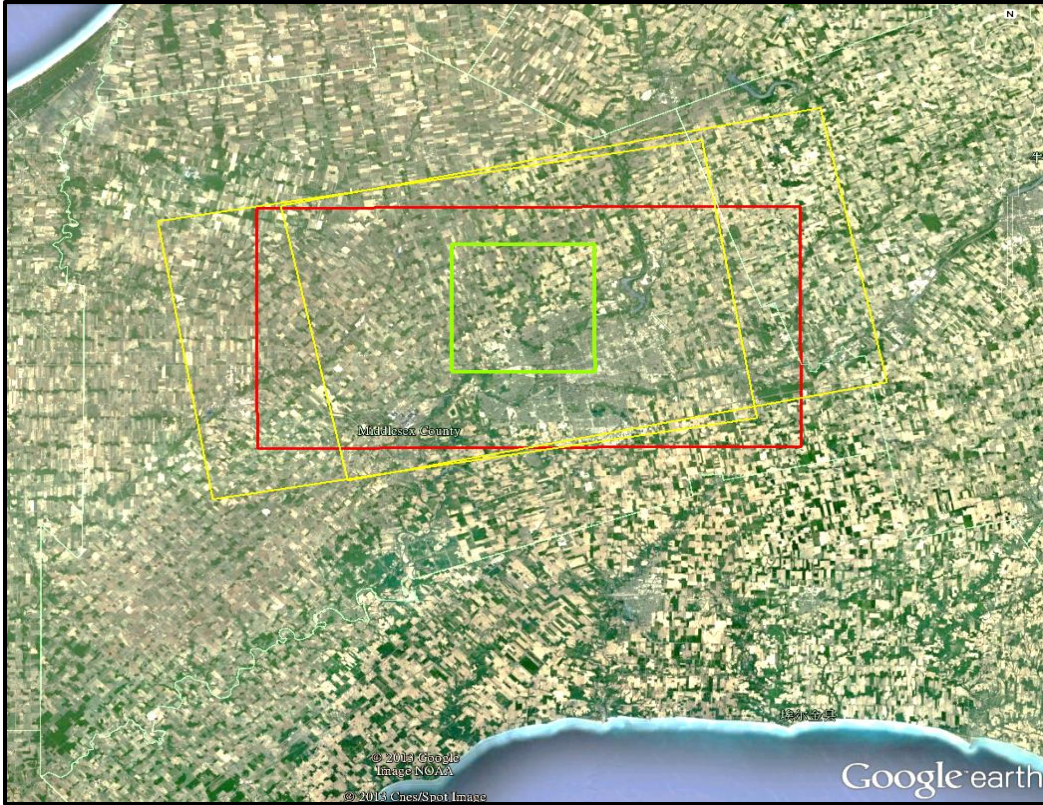
Figure 1.2 The boundaries of RapidEye images (Red), RADARSAT-2 images (Yellow), and study areas (Green) shown on the Google Earth images.

The RADARSAT-2 is a RADAR observation satellite that was successfully launched on December 14th, 2007 by MacDonald Dettwiler & Associates (MDA) and the Canadian Space Agency. As the successor of the earlier RADARSAT-1, the RADARSAT-2 satellite was developed in order to enhance the SAR systems' applications in sea ice mapping, iceberg detection, marine surveillance for ships and pollution detection, geological mapping, wetlands mapping, topographic mapping, land use land cover mapping, and agricultural crop monitoring (Canadian Space Agency, 2007).

Two sets of wide fine beam polarimetric (also called Quadpol) RADARSAT-2 data were acquired for this research (Table 1.1). One set was taken at the steeper incidence angle, between 25° to 28°, while the other set of data were taken at a shallower incidence angle, between 40° to 42°. Both data sets have similar pixel spacing, of approximately 5 meters,

and wide landscape spatial coverage of 50km by 25km. All the data were taken from early May to September, 2012.

Table 1.1 RADARSAT-2 data parameters from data head files

Name	Pixel spacing Pixel×Line	Coverage (km)	Incidence Near edge	Incidence Far edge	Dates (mdd2012)
Wide Fine Quadpol7	4.7m×4.7m	25×50	24.9°	28.3°	504, 528, 621, 715, 901
Wide Fine Quadpol21	4.7m×5.1m	25×50	40.2°	41.6°	507, 624, 718, 811, 904, 928

RapidEye is a commercial optical satellite developed by TÜV NORD of Germany, MDA, and RapidEye AG. The RapidEye system contains five independent satellites, which enable observation of the Earth's surface with high-resolution imagery over large areas. RapidEye images can be used to provide valuable information about land surfaces.

The nadir resolution for these satellite images is 6.5 meters, and the swath width is 77 kilometers. In the RapidEye system, two vegetation sensitive bands, the red edge and the near infrared band are provided to optimize the satellite's potential for vegetation detection . Therefore, RapidEye has great advantages in agricultural applications. Many Vegetation Indices have been derived from the multispectral bands to capture the vegetation characteristics (Andrés et al., 2011).

Although RapidEye seems to be an ideal data source for agricultural applications, its optical nature limits data collection under unfavourable weather conditions. In this study, five scenes of RapidEye images were acquired during the 2012 crop growing season (Table 1.2). Each complete RapidEye dataset were combined from two adjacent scenes. During the 2012 growing season, many days were cloudy or rainy; as a result, it was necessary to

combine multiple images. In order to achieve a cloud free image in the mid- July over the whole study area, images taken on the July 16th and July 24th were combined together. The lack of cloud free optical images makes it difficult to interpret complete and useful information about land surfaces.

Table 1.2 The parameters of RapidEye data

Spectral Band	Blue	Green	Red	Red Edge	Near Infrared
Wavelength(nm)	440-510	520-590	630-685	690-730	760-850
Dates(m_dd_yyy)	6_07_2012	7_16_2012	7_24_2012	8_05_2012	8_25_2012
Scene Location	West&East	West	East	West&East	West&East

1.4   Thesis Format

This research is presented in integrated-article format. Chapter 1 gives a brief review of the literature on the research problems, the objectives of the research, and the study area and data used in this research.

The focus of the thesis is to investigate the potential of polarimetric RADARSAT-2 SAR data in Land Use/Land Cover information extraction and crop condition monitoring. To achieve this goal, different imagery sources and processing methods were used. Chapter 2 focuses on assessing the potential of RADARSAT-2 polarimetric imagery for Land Use/Land Cover classification. Chapter 3 analyzed the sensitivities of polarimetric parameters to the Normalized Difference Vegetation Index and crop height.

1.5 References

Andrés Viña, Anatoly A. Gitelson, Anthony L. Nguy-Robertson, Yi Peng, (2011). Comparison of different vegetation indices for the remote assessment of green leaf area index of crops Remote Sensing of Environment, Volume 115, Issue 12, 15 December, Pages 3468-3478.

Blaes, X., Vanhalle, L., & Defourny, P. (2005). Efficiency of crop identification based on optical and SAR image time series. Remote Sensing of Environment, 96, 52−365.

Cameron, W. L., & Rais, H. (2006). Conservative polarimetric scatterers and their role in incorrect extensions of the Cameron decomposition. IEEE Transactions on eoscience and Remote Sensing, 44, 3506–3516.

Canadian Space Agency (2007). "http://www.asc-sa.gc.ca/eng/satellites/radarsat2/applications.asp"

Chakraborty, M., Manjunath, K. R., Panigrahy, S., Kundu, N., & Parihar, J. S. (2005). Rice crop parameter retrieval using multi-temporal, multi-incidence angle RADARSAT SAR data. ISPRS Journal of Photogrammetry & Remote Sensing, 59, 310−322.

Cloude, S. R., & Pottier, E. (1996). A review of target decomposition theorems in radar polarimetry. IEEE Transactions on Geoscience and Remote Sensing, 34, 498–18.

Corbane C, Faure J. F., Baghdadi N, Villeneuve N, Petit M. Rapid Urban Mapping Using SAR/Optical Imagery Synergy (2008). Sensors. 8(11):7125-7143.

Defries, R. S., & Townshend, J. R. G. (1994). NDVI-derived land cover classification at global scale. International Journal of Remote Sensing, 15(17), 3567–3586.

Du, L., & Lee, J. S. (1996). Fuzzy classification of earth terrain covers using complex polarimetric SAR data. International Journal of Remote Sensing, 17, 809–826.

Fisette, T., Maloley, M., Chenier, R., White, L., Huffman, T., Ogston, R., Pacheco, A., Gasser, P. Y., 2005. Towards a national agricultural land cover classification evaluating decision tree approach. In: 26th Canadian Symposium on Remote Sensing, Wolfville, Nova Scotia, June 14–16 (on CD-ROM).

Freeman, A., & Durden, S. L. (1998). A three-component scattering model for polarimetric SAR data. IEEE Transactions on Geoscience and Remote Sensing, 36, 963–973.

Freitas, C. D., Soler, L. D., Anna, S. J. S. S., Dutra, L. V., dos Santos, J. R., Mura, J. C., & Correia, A. H. (2008). Land use and land cover mapping in the Brazilian Amazon using polarimetric airborne p-band SAR data. IEEE Transactions on Geoscience and Remote Sensing, 46, 2956–2970.

Friedl, M. A., Menashe, D. S., Tan, B., Schneider, A., Ramankutty, N., Sibley, A., et al. (2010). MODIS collection 5 global land cover: Algorithm refinements and characterization of new datasets. Remote Sensing of Environment, 114, 168–182.

Gao, Y., Mas, J. F., Maathuis, B. H. P., Zhang, X. M., & Van Dijk, P. M. (2006). Comparison of pixel-based and object-oriented image classification approaches — A case study in a coal fire area, Wuda, Inner Mongolia, China. International Journal of Remote Sensing, 27, 4039–4055.

Geneletti, D., & Gorte, B. G. H. (2003). A method for object-oriented land cover classification combining Landsat TM data and aerial photographs. International Journal of Remote Sensing, 24, 1273–1286.

Gopal, S., Woodcock, C. E., & Strahler, A. (1999). Fuzzy neural classification of global land cover from a 1 degree AVHRR Data Set. Remote Sensing of Environment, 7, 230–243.

Guerschman, J. P., Paruelo, J. M., Bella, C. D. I., Giallorenzi, M. C., & Pacin, F. (2003). Land cover classification in the Argentine Pampas using multi-temporal Landsat TM data. International Journal of Remote Sensing, 24(17), 3381–3402.

Guerschman, J.P., Paruelo, J.M., Di Bella, C., Giallorenzi, M.C., Pacin, F., (2003). Land cover classification in the Argentine Pampas using multi-temporal Landsat TM data. International Journal of Remote Sensing 24 (17), 3381–3402.

Hansen, M. C., Defries, R. S., Townshend, J. R. G., & Sohlberg, R. (2000). Global land cover classification at 1 km spatial resolution using a classification tree approach. International Journal of Remote Sensing, 21(6 & 7), 1331–1364.

Lee, J. S., Grunes, M. R., & Pottier, E. (2001). Quantitative comparison of classification capability: Fully polarimetric versus dual and single-polarization SAR. IEEE Transactions on Geoscience and Remote Sensing, 39, 2343–2351.

Li, H. T., Gu, H. Y., Han, Y. S., & Yang, J. H. (2008). Object-oriented classification of polarimetric SAR imagery based on statistical region merging and support vector machine. Proceedings of the 2008 International Workshop on Earth Observation and Remote Sensing Applications (pp. 147–152). Beijing, China.

Li, X., Yeh, A. G. O., Qian, J. P., Ai, B., & Qi, Z. X. (2009). A matching algorithm for detecting land use changes using case-based reasoning. Photogrammetric Engineering and Remote Sensing, 75, 1319–1332.

Liu, J., E. Pattey, et al. (2012). Assessment of vegetation indices for regional crop green LAI estimation from Landsat images over multiple growing seasons. Remote Sensing of Environment 123(0): 347-358.

Lombardo, P., M. Sciotti, T.M. Pellizzeri, and M. Meloni. (2003). "Optimum Model-Based Segmentation Techniques for Multifrequency Polarimetric SAR Images of Urban Areas." IEEE Transactions on Geoscience and Remote Sensing 41: 1959–75.

McNairn, H., Champagne, C., Shang, J., Holmstrom, D.A., and Reichert, G. (2009). Integration of optical and Synthetic Aperture Radar (SAR) imagery for delivering operational annual crop inventories." ISPRS Journal of Photogrammetry and Remote Sensing, 64(5), pp. 434-449.

Moran, M. S., Vidal, A., Troufleau, D., Qi, J., Clarke, T. R., Pinter, P. J., et al. (1997). Combining multifrequency microwave and optical data for crop management. Remote Sensing of Environment, 61, 96−109.

Nicolas B., Nathalie B., Pierre T., Mahmoud E. Agnès B., (2009), Potential of SAR sensors TerraSAR-X, ASAR/ENVISAT and PALSAR/ALOS for monitoring sugarcane crops on Reunion Island, Remote Sensing of Environment, Volume 113, Issue 8, Pages 1724-1738.

Niu, X., and Y. Ban. (2010). "Multitemporal RADARSAT-2 Polarimetric SAR Data for Urban Land Cover Classification Using Support Vector Machine." In 30th EARSeL Symposium, 581−8, Paris, 31 May−3 June 2010, edited by R. Reuter. Hannover: EARSeL.

OMAFRA, (2011) Census of Agriculture and Strategic Policy Branch, 2012. Ontario, Canada. Middlesex County at a Glance.

Pellizzeri, T. M. (2003). "Classification of Polarimetric SAR Images of Suburban Areas Using Joint Annealed Segmentation and 'H / A /α' Polarimetric Decomposition." ISPRS Journal of Photogrammetry and Remote Sensing 58: 55−70.

Pellizzeri, T. M., P. Gamba, P. Lombardo, and F. Dell'acqua.(2003). "Multitemporal / Multiband SAR Classification of Urban Areas Using Spatial Analysis: Statistical Versus Neural Kernel-Based Approach." IEEE Transactions on Geoscience and Remote Sensing 41: 2338−53.

Pierce, L. E., Ulaby, F. T., Sarabandi, K., & Dobson, M. C. (1994). Knowledge-based classification of polarimetric SAR images. IEEE Transactions on Geoscience and Remote Sensing, 32, 1081−1086.

Qi, Z., Yeh, A. G. O., Li, X., & Lin, Z. (2012). A novel algorithm for land use and land cover classification using RADARSAT-2 polarimetric SAR data. Remote Sensing of Environment, 118, 21-39.

Reese, H.M., Lillesand, T., Nagel, D.E., Stewart, J.S., Goldman, R.A., Simmons, T.E., Chipmand, J.W., Tessar, P.A., (2002). Statewide land cover derived from

multiseasonal Landsat TM data-A retrospective of the ISCLAND project. Remote Sensing of Environment 82 (2), 224–237.

Service Canada. (2009) "London Labour Market Monitor". London, Ontario.

Shao, Y., Fan, X., Liu, H., Xiao, J., Ross, S., Brisco, B., et al. (2001). Rice monitoring and production estimation using multitemporal RADARSAT. Remote Sensing of Environment, 76, 310−325.

Statistics Canada. (2012). 2011 Census: Population and dwelling counts. Statistics Canada . Ottawa.

Statistics Canada. 2012. Net Farm Income Agriculture Economic Statistics. Ottawa.

Statistics Canada. 2012. Remote Sensing and Geospatial Analysis, Agriculture Division, 2012. Canada Change in number of farms reporting cattle between 2006 and 2011.

Tucker, C. J., Townshend, J. R. G., & Goff, T. E. (1985). African land-cover classification using satellite data. Science, 227(4685), 369–375.

Turker, M., Arikan, M., (2005). Sequential masking classification of multi-temporal Landsat7 ETM+ images for field-based crop mapping in Karacabey, Turkey. International Journal of Remote Sensing 26 (17), 3813–3830.

Ulaby, F. T., A. Tavakoli, and T. B. A. Senior (1987), Microwave propagation constant for a vegetation canopy with vertical stalks, IEEE Trans. Geosci. Remote Sens., 25(6), 714–725.

Watts, J. D., Lawrence, R. L., Miller, P. R., & Montagne, C. (2009). Monitoring of cropland practices for carbon sequestration purposes in north central Montana by Landsat remote sensing. Remote Sensing of Environment, 113, 1843–1852.

Wolter, P. I., Mladenoft, D. S., & Crow, T. R. (1995). Improved forest classification in the northern lake states using multi-temporal Landsat imagery. Photogrammetry Engineering & Remote Sensing, 61(9), 1129–1143.

Yang, J., Yamaguchi, Y., Yamada, H., Sengoku, M., & Lin, S. M. (1998). Stable decomposition of Mueller matrix. IEICE Transactions on Communications, 1261–1268 E81b.

Zhang, L., B. Zou, J. Zhang, and Y. Zhang. (2010). "Classification of Polarimetric SAR Image Based on Support Vector Machine Using Multiple-Component Scattering Model and Texture Features." EURASIP Journal on Advances in Signal Processing 2010: 1–9.

Zhu, Z., C. Woodcock, J. Rogan, and J. Kellndorfer. (2011). "Assessment of Spectral, Polarimetric, Temporal, and Spatial Dimensions for Urban and Peri-Urban Land Cover Classification Using Landsat and SAR Data." Remote Sensing of vironment 117: 72–82.

Chapter 2

2   Assessment of Multi-temporal Polarimetric RADARSAT-2 data for Land Use and Land Cover Classification in an Urban/Rural Fringe Area

2.1   Introduction

2.1.1   Background

Land Use and Land Cover (LU/LC) information provides the basis for many studies, such as carbon modeling, land use change detection, forest management, and crop yield estimation (Jung et al., 2006; Lark & Stafford, 1997; Wolter et al., 1995; Woodcock et al., 2001). In recent decades, changes in LU/LC composition have been occurring all over the world, due to rapid urban expansion.

The emergence of urban/rural fringe zones caused by urban expansion has led to serious land use problems, such as loss of agricultural land, unauthorized urban sprawl, and high land values (Qi et al., 2012). The fringe zones, which have been somewhat in either rural or urban studies, have become a topic of great importance (Zhu et al., 2011). In order to deal with land use problems, complete and timely land surface information about fringe areas is required.

Remote sensing has the characteristics of broad coverage and repetitive visit, and thus provides a practical and economical method for obtaining LU/LC information (Rogan et al., 2004). The use of aerial photographs to map land use and land cover mapping can be dated back to 1940s (Lillesand et al., 2004). The earliest space borne optical Remote Sensing sensor for LU/LC mapping was a series of Earth Resources Technology Satellites (ERTSs), also called "Landsat" program, developed by NASA, with the cooperation of the U.S. Department of the Interior. The satellites have the capability to cover the globe (except the $82\,^{\circ}$ to $90\,^{\circ}$ polar latitudes once every 18 days at the spatial resolution of 80m (Lillesand et al., 2004). In the past few decades, increasing high spatial resolution Remote Sensing data are available now, providing by satellites such as the Quickbird, Worldview and so on. Those day have been commonly used in urban areas,

such as boundaries detection and impervious surface extraction. In rural areas, remote sensing satellites capable of high temporal resolution imaging are useful for delivering crop type inventory, and crop condition monitoring (McNairn et al., 2009). However, little research has focused on the application of Remote Sensing in the rural/urban fringe areas. The mixture of dynamic land use and complex LU/LC classes in fringe zones has created challenging for either urban sprawl detection or crop inventory (Zhu et al., 2011).

2.1.2   Previous Studies

Remotely sensed data have been widely used in LU/LC classification. Most LU/LC types in the urban areas remain unchanged in a short period, and thus multi-temporal datasets are not necessary for distinguishing urban LU/LC classes. For example, using two images acquired at two very close dates, Qi successfully distinguished several LU/LC classes in urban/sub-urban areas with a high overall accuracy of 86.64 %(Qi, et al., 2012). However, in Qi's study, all the croplands were considered as one LU/LC type, the cropland/natural vegetation.

Multi-temporal images are essential to identify different crop types. During the growing seasons, crops evolve through a series of phenological stages. Meanwhile, the structure and water content of crops varies from type to type or even from field to field. Capturing the differences in temporal changes of crops is key to their identification. For example, in Southwestern Ontario, the growing season of most winter wheat is from April to July. However, most of the soybeans and corn are not planted until late May. Therefore, without multi-temporal datasets, satisfactory classification results are unlikely to be obtained. In the classification of crops, the selection of multi-temporal sequences of SAR images is critical to the classification results. McNairn and Skriver reported that higher accuracy in crop identification could be achieved by adding more multi-temporal SAR images (McNairn et al., 2009).

Multi-temporal optical images are ideal data sources for LU/LC classification in the urban/rural fringe areas. Remotely sensed images obtained from various optical sensors have been widely used in LU/LC mapping (Saatchi et al., 1997; Roberts et al., 2003; Thenkabail et al., 2005). However, high-quality optical images are not always available

due to the frequent cloudy and rainy weather during the growing season. Take London, Ontario as an example, during the whole growing season in 2012 (May to September), only three scenes of cloud free RapidEye optical images were obtained. The applications of optical remote sensing data in LU/LC classification of wide areas are limited by weather conditions.

Synthetic Aperture Radar (SAR) sensors play an increasingly important role in LU/LC classification due to their ability to obtain images day and night through cloud cover and haze (Shang et al., 2006; Shang et al., 2009). In 1978, the Seasat-1 was the first radar satellite developed for oceanographic research (Lillesand et al., 2004). SAR data are able to capture the dielectric properties and structure of the earth's surface materials, and thus provide complementary information for the optical data.

Early studies have used multitemporal SAR data to investigate LU/LC information, but mainly focused on the single polarization (Desons et al., 1999; Weber et al., 2003; Li et al., 2007). In the past few decades, most of the orbital radar systems, such as the ERS-1, ERS-2, JERS-1, and RADARSAT-1, only provided single or dual polarization data. The information contained in the single or dual polarization data is limited and may create confusion in distinguishing some LU/LC types (Ulaby et al., 1986; Li & Yeh, 2004, Dan et al., 2010).

In order to improve the effectiveness of single polarization SAR data, many researchers have utilized quad polarization (polarimetric) SAR data in LU/LC classification (McNairn et al., 2009; Niu and Ban, 2013; Qi et al., 2012). Recently, high spatial and temporal resolution polarimetric SAR data have been available through the radar systems, such as C-band RADARSAT-2, X-band TerraSAR-X, and Phased Array type L-band SAR (PALSAR) sensors. With access to those multitemporal sequences of high-resolution and polarimetric SAR data, a SAR-only solution for surveying rapid urban sprawl in the urban/rural fringe areas becomes increasingly viable (Palubinskas, et al. 2011).

Polarimetric SAR data provide the description of land features from the observations of full polarizations. Therefore, more information can be explored from the polarimetric

SAR data than from the single or dual polarization images (Lee et al., 2009; McNairn et al., 2009; Niu and Ban, 2013; Qi et al., 2012). Some research has shown that by integrating polarimetric data in the classification, not only are the classification accuracies of vegetation types enhanced, but also the separability between vegetation and built-up is increased (McNairn et al., 2009; Skriver H., 2012; Qi et al., 2012). Using polarimetric decomposition methods, a complex radar signal can be decomposed into several scattering responses from simpler objects with easier physical interpretation. Decomposed parameters provide information about corresponding target types in the image, and thus are able to facilitate the classification of various LU/LC classes.

2.1.3 Objectives

The major objective of this study is to assess the potential of polarimetric RADARSAT-2 data for LU/LC classification of urban/rural fringe areas. More specific objectives are: (1) to examine the effectiveness of various polarimetric decomposition parameters in LU/LC classification; (2) to find the best combination of multi-date data for accurate and efficient LU/LC classification; (3) to provide a suitable procedure for LU/LC classification of urban/rural fringe areas.

2.2   Study Area and Data Description

2.2.1   Study Area

The study area is situated in the northwest portion of the urban/rural fringe areas surrounding London, a city in southwestern Ontario, Canada. The region is characterized by a flat, regular topography which is notable for its productive agricultural lands. In recent decades, London has been experiencing rapid urban expansion. Therefore, the timely information about LC/LU in this area is critical for urban sprawl detection as well as for monitoring the areas lost to urban development. There are a wide range of LU/LC classes, such as commercial areas, industrial areas, residential areas, construction sites, forests, grass and agricultural areas. The main crop types in this area includes corn, soybeans, wheat, and field peas. The complex nature of LU/LC types in the urban/rural fringe area is both a challenge and an opportunity to test the potential of multi-temporal RADARSAT-2 data in mapping.
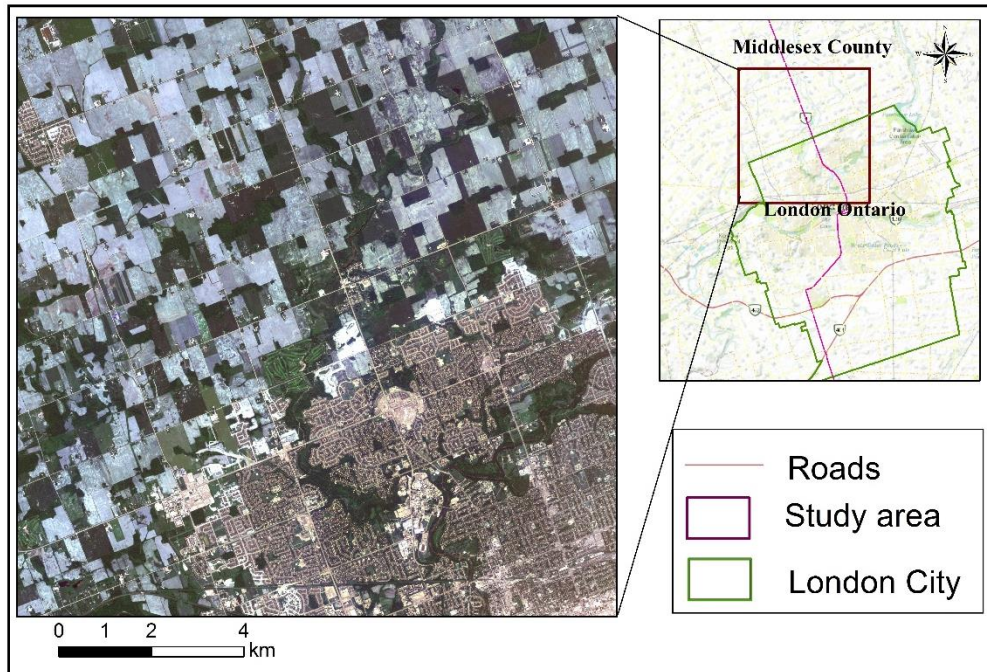
Figure 2.1 The location of London, Ontario, and the RapidEye image of the study area

2.2.2   Remote Sensing Data

Five dates of RADARSAT-2 wide fine beam Quadpol (polarimetric) images were acquired in ascending orbits over the study area from May 4th to September1st, 2012. Polarimetric information is recorded in HH, VV, HV, VH bands, with a nominal pixel spacing of 4.7m and 4.7m in the range and azimuth directions. The incidence angles for the five images are varying from 24.9 ° to 28.3 °. The frequency of the RADARSAT-2 data is 5.4 GHz at a wavelength of 5.6 cm.

Optical data used in the research is geometrically corrected RapidEye satellite imagery and air photos. The RapidEye images are multi-spectral optical data, which have five multispectral bands (from 440 nm to 850 nm) at 6.5m spatial resolution. The air photos used in the study were taken in April, 2011 with a 15cm spatial resolution (Provided by city of London). The optical data were used as reference for SAR data classification.

Table 2.1 RADARSAT-2 and RapidEye imagery from head files

Satellite	Mode	Wave length	Dates	Resolution	Bands
RADARSAT-2	Wide FQ7	5.6cm	May 4, May 28, June 21,July 15, Sept.1, 2012	8-12m	HH, VV , HV, VH
RapidEye	Standard	440 - 850nm	June 7, July 16,July 24, Aug 25, 2012	6.5m	Blue, Green, Red, Red Edge, Near Infrared

2.2.3   Field Data Collection

The purpose of the field work was to investigate the LU/LC types and crop growing state. Two general investigations of crop and non-crop LU/LC types were completed in July and September. More frequent field work was conducted through the whole crop growing season, so as to ensure that there were in-situ data available whenever RADARSAT-2 image was taken.

In the field, the accurate locations of various crop lands were recorded using GPS units. To observe crop conditions at different growing stages, the average crop height were measured and crop samples were photographed. Weather condition was recorded, as inclement weather influences the moisture of scatterers, such as soil and crops. The change of moisture leads to the change of dielectric constant, which might result in abnormal SAR backscattering values. In order to facilitate the interpretation of the SAR data, hourly meteorological information was recorded to coincide with RADARSAT-2 imaging dates.

2.3   Methodology

The methodology for this research consists of RADARSAT-2 image preprocessing; selection of samples; multi-temporal RADARSAT-2 dataset classification; post classification processing, and accuracy assessment (Figure 2.2).
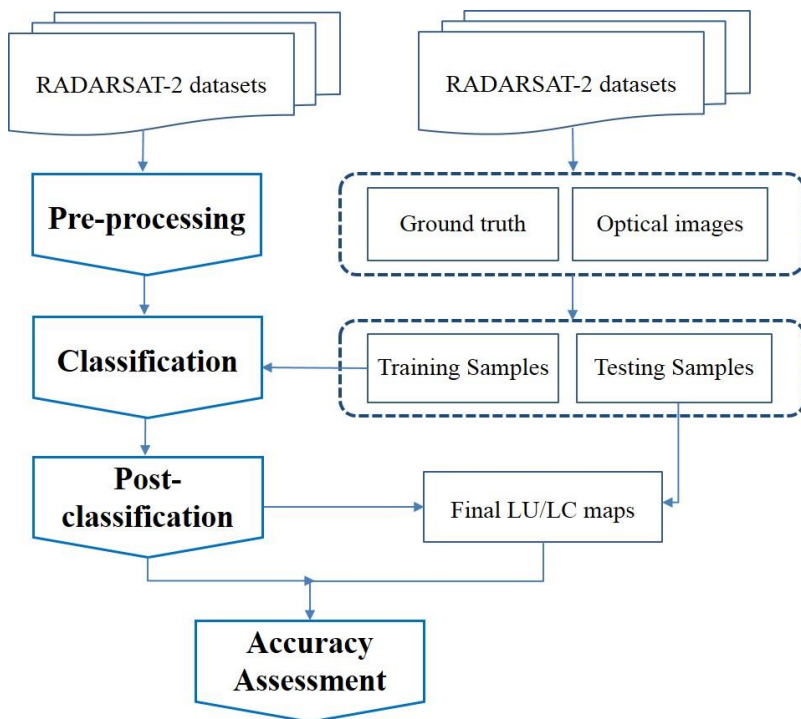
Figure 2.2 The flowchart showing the methodology for LU/LC classification

2.3.1   RADARSAT-2 Data Pre-processing

The preprocessing of polarimetric SAR data is of critical importance to achieving good classification results (Lee et al., 2009); as such, three main pre-processing steps have been sequentially conducted, including polarimetric decomposition data extraction, speckle filtering, and geometric correction (Figure 2.3).
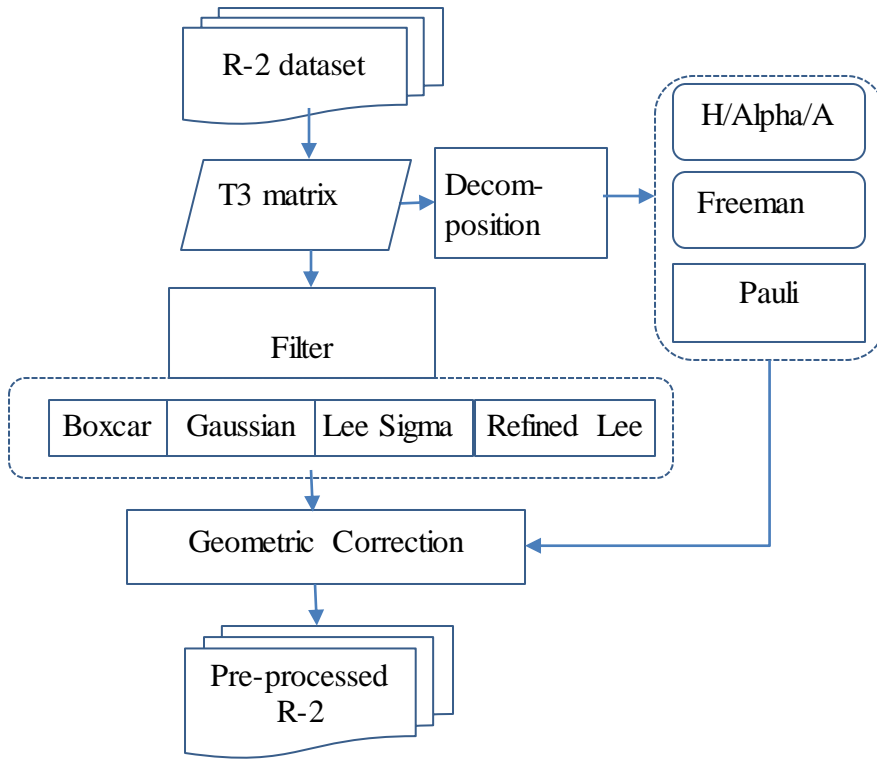
Figure 2.3 An overview of the preprocessing of RADARSAT-2 images

2.3.1.1 Coherency Matrix and Pauli Decomposition and

The raw polarimetric RADARSAT-2 data are recorded in the four elements of the S matrix, S_{hh}, S_{hv}, S_{vh}, S_{vv} (see the function 2.1). Initially, the coherency matrix T3 was extracted from the S matrix using PolSARpro software. The coherency matrix T3 contained all the polarimetric information. Most of the decomposition parameters were derived from coherency matrix T3, or covariance C3, which contains similar information, but in different form. The coherency matrix T3 and covariance matrix C3 can be expressed as:

$$S = \begin{bmatrix} S_{hh} & S_{hv} \\ S_{vh} & S_{vv} \end{bmatrix} \tag{2.1}$$

$$K = \frac{1}{\sqrt{2}} [S_{hh} + S_{vv} \quad S_{hh} - S_{vv} \quad S_{hv} + S_{vh}]^T \tag{2.2}$$

$$T_3 = \langle K \cdot K^{*T} \rangle \tag{2.3}$$

$$T_3 = \begin{bmatrix} T_{11} & T_{12} & T_{13} \\ T_{12}{}^* & T_{22} & T_{23} \\ T_{13}{}^* & T_{23}{}^* & T_{33} \end{bmatrix} \tag{2.4}$$

$$= \frac{1}{2}\begin{bmatrix} |S_{hh}+S_{vv}|^2 & (S_{hh}+S_{vv})(S_{hh}-S_{vv})^* & 2(S_{hh}+S_{vv})S_{hv}{}^* \\ (S_{hh}-S_{vv})(S_{hh}+S_{vv})^* & |S_{hh}-S_{vv}|^2 & 2(S_{hh}-S_{vv})S_{hv}{}^* \\ 2S_{hv}(S_{hh}+S_{vv})^* & 2S_{hv}(S_{hh}-S_{vv})^* & 4|S_{hv}|^2 \end{bmatrix}$$

$$C_3 = \begin{bmatrix} C_{11} & C_{12} & C_{13} \\ C_{12}{}^* & C_{22} & C_{23} \\ C_{13}{}^* & C_{23}{}^* & C_{33} \end{bmatrix} \tag{2.5}$$

$$= \begin{bmatrix} |S_{hh}|^2 & \sqrt{2}S_{hh}S_{hv}{}^* & S_{hh}S_{vv}{}^* \\ \sqrt{2}S_{hv}S_{hh}{}^* & 2|S_{hv}|^2 & \sqrt{2}S_{hv}S_{vv}{}^* \\ S_{hv}S_{hh}{}^* & \sqrt{2}S_{vv}S_{hv}{}^* & |S_{vv}|^2 \end{bmatrix}$$

*For the monocratic case, $S_{hv} = S_{vh}$, * denotes the conjugate and | | detonates the module.*

The Pauli decomposition parameters are composed of the three diagonal elements of the coherency matrix T3. The advantage of the Pauli decomposition is that each of the three elements corresponds to a basic scattering mechanism. $S_{HH}+S_{VV}$ represents single (odd) bounce scattering, $S_{HH}-S_{VV}$ indicates double bounce scattering, and $S_{HV}+S_{VH}$ is associated with volume scattering. Typical LU/LC examples in the real field for those three scattering mechanisms are bare soil, buildings and forests, respectively (Lee and Pottier, 2009).

2.3.1.2 Other Polarimetric Decomposition

(1) Freeman-Durden decomposition

The Freeman-Durden decomposition is a method for fitting a physically based, three-component scattering mechanism model to polarimetric SAR observations. The three-component scattering mechanism include surface, double-bounce and volume scattering mechanisms (Lee and Pottier, 2009). This approach can be used to determine the dominant

scattering mechanisms and to facilitate identifying the current state of the surface cover. In addition, the three-component scattering may provide features for distinguishing between different surface cover types. Although the Freeman-Durden decomposition has been widely used in LU/LC classification, it has some limitations. Since Freeman-Durden method was intended to model the backscattering from forests, it might be invalid for other surface scatterings.

(2) H/Alpha/A Decomposition

H/Alpha/A decomposition is an approach proposed by Cloude and Pottier for extracting average parameters from experimental data using a smoothing algorithm based on second-order statistics (Cloude and Pottier, 1996; Cloude and Pottier, 1997). Decomposition parameters are generated from an eigenvector analysis of the coherency matrix T3. The eigenvectors describe different scattering processes, and the eigenvalues indicate their relative magnitudes. Among all the parameters, the averaged Alpha angle (α) relates directly to the underlying average physical scattering mechanisms. The value of Alpha ranges from 0° to 90°, which indicates the dominant scattering varies from surface scattering mechanism (0°), moving into single scattering (45°) by a cloud of anisotropic particles, and finally reaching dihedral scattering (90°). The Entropy (H) describes the randomness of the scatter. The anisotropy (A) corresponds to the relative power of the second and third eigenvectors (Lee and Pottier, 2009).

Both of the aforementioned polarimetric target decomposition methods have been commonly used in the LU/LC classification (Qi et al., 2010; McNairn et al., 2009; Niu et al., 2013). In this study, the three polarimetric decomposition methods mentioned above have been applied to each RADARSAT-2 image (Figure 2.3). A right multi-look number is critical to the final classification results. After several tests, the multi-look number of 3 for Freeman-Durden decomposition, and the multi-look number 7 for H/Alpha/A was applied, see the decomposition results in Figure 2.4.

(a) Pauli

(b) Freeman

(c) H/Alpha/A

(d) RapidEye
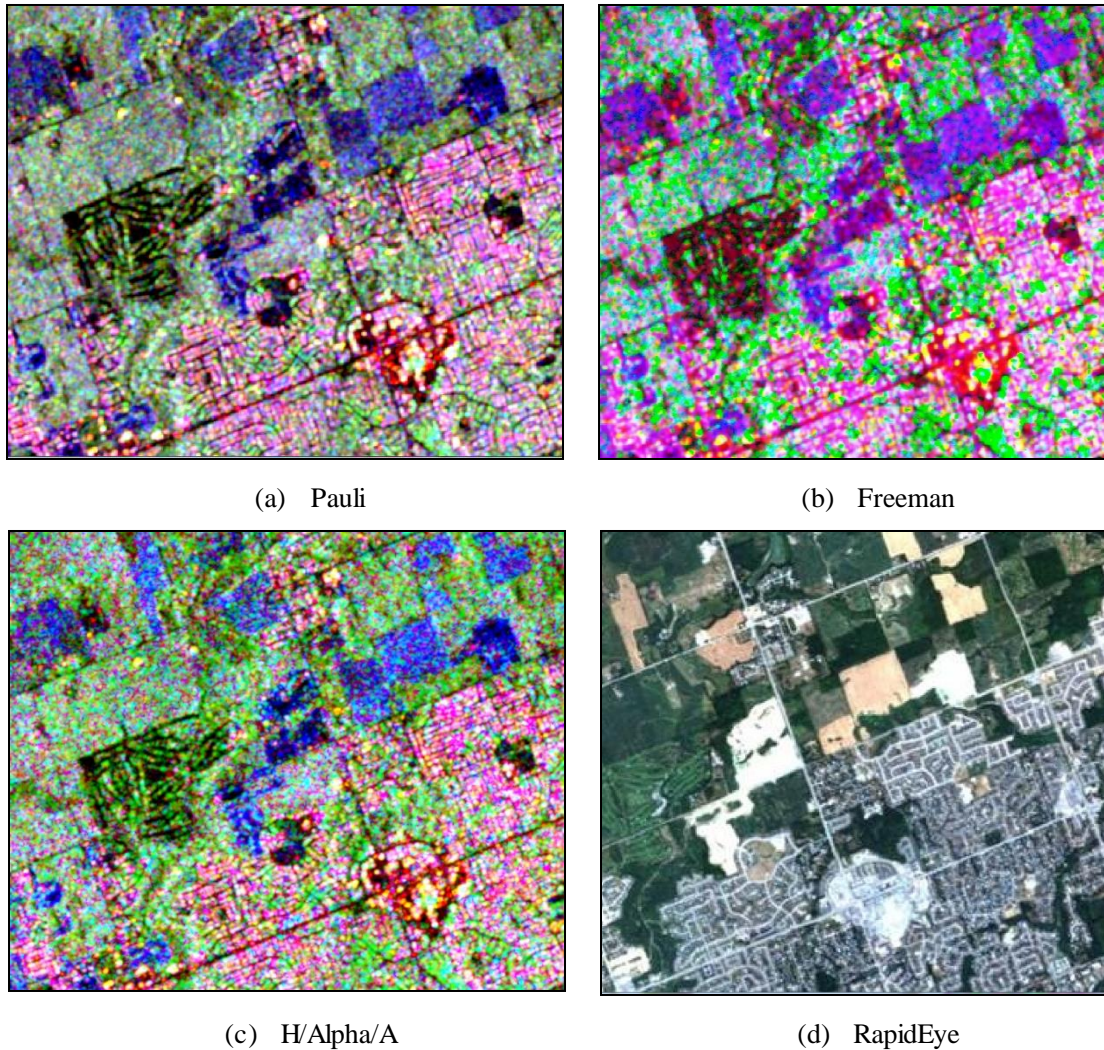
Figure 2.4 RGB composition images presenting different polarimetric decomposition methods.

2.3.1.3   Speckle Filter

Speckle effects are inherent noises resulting from the coherent interference of the waves that have been reflected from elementary scatter (J.W. et al., 1976; Lee et al., 1994; Lee and Pottier, 2009). In order to achieve optimal speckle-reducing in imagery, four different filters, boxcar, Gaussian, sigma Lee, and Refined Lee, were tested and compared (Figure 2.5). Visually, Gaussian filter achieved the best results among all the filters. After filtering with the boxcar filter, the boundaries of each LU/LC type were quite blurred. In the Sigma Lee filtered images, the separability among various classes was increased after filtering;

however, some dark and bright points remained unfiltered. In contrast, the Refined Lee filter maintained the sharp boundaries of land surface features, but introduced some false edges. Within homogenous crop fields, these false edges appear as larger speckles.

Boxcar

Gaussian

Sigma Lee

Refined Lee
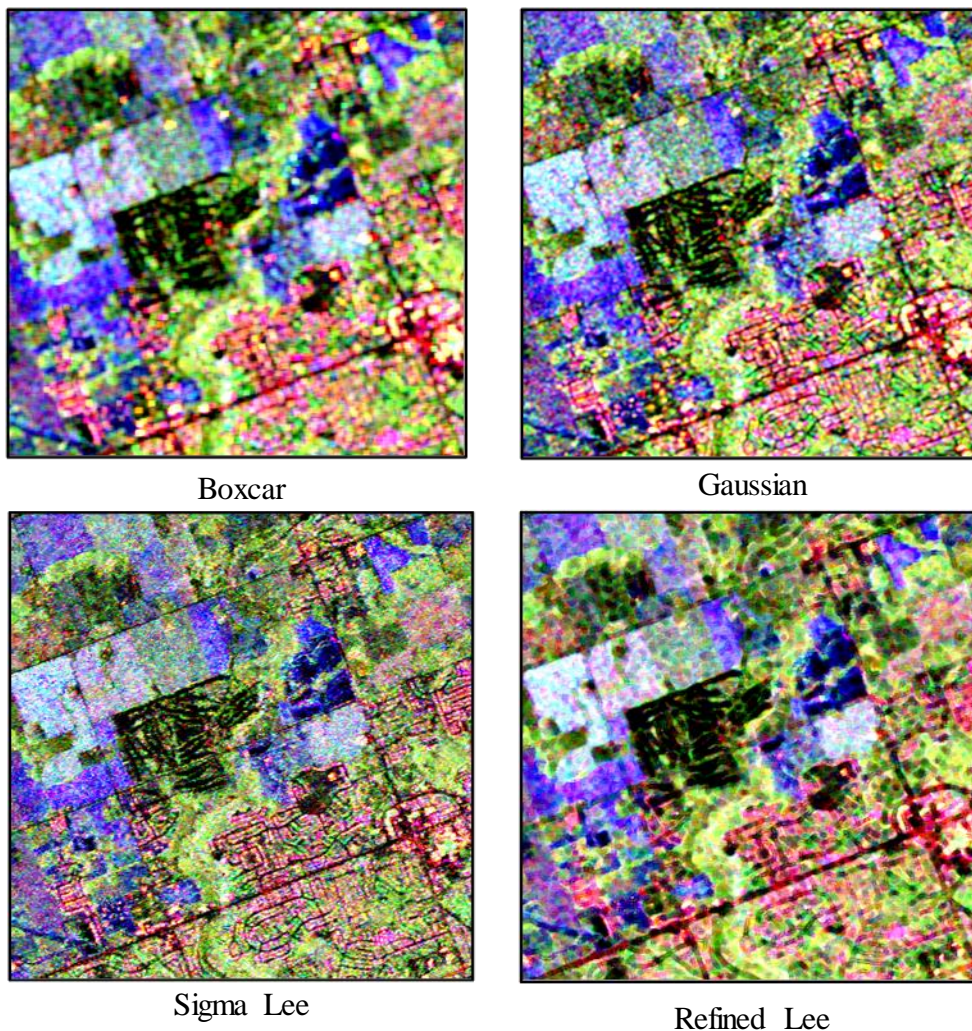
Figure 2.5 Filtered Pauli RGB images using different speckle filtering methods

The Gaussian function, which is also used to express the normal distribution, is applied to smooth an image by calculating the weighted averages in a filter box. In two dimensions image, the weight factors for a Gaussian distribution can be expressed as

$$G(x,y) = \frac{1}{2\pi\sigma^2} e^{-\frac{x^2+y^2}{2\sigma^2}}$$ (2.7)

where x is the distance from the origin in the horizontal axis, y is the distance from the origin in the vertical axis; σ is the standard deviation of the Gaussian distribution (Cover, 2006). Gaussian filter is a low-pass filter, and is thus able to reduce the image's high-frequency components. The Gaussian filter was applied to each polarimetric SAR image prior to analysis.

2.3.1.4   Geometric Correction

Geometric correction is an essential step in SAR data preprocessing. Due to the unique SAR satellite imaging process, the image is recorded in a slant range system, where distances on the Earth's surface are measured between the antenna and the target (Lee and Pottier, 2009). In areas with large elevation variation, serious geometric distortion can be easily observed in SAR images (Chen et al., 2008). Since the selected study area is generally flat, terrain effects, such as layover and shadowing are avoided. Effective geometric correction was conducted to transfer the slant range system to the ground range coordinate system. Subsequently, the multitemporal SAR images were georegistered together.

MapReady is a Remote Sensing Tool kit developed by Alaska Satellite Facility. This tool can be used to correct terrain effects, geocode polarimetric decomposition parameters and converted data to several common imagery formats. The MapReady tool kit used in this study is embedded in the PolSARpro software. Therefore, geometric correction can be applied directly on the datasets of T3, C3 matrix and other polarimetric parameters generated from the PolSARpro software. Initially, the platform ephemeris information of SAR images and the Digital Elevation Model (DEM) data of the study area were used to simulate an amplitude image. Terrain effects were then corrected through matching the real SAR image with the simulated SAR data.

After geometric correction, visual inspection of urban streets and boundaries of lakes and rivers in the geocorrected SAR images shows that they align with the same features in the geocorrected RapidEye images of the same area (Figure 2.5). These accurate geometric correction results provided a solid foundation for subsequent image analysis and classification.

(a)   (b)
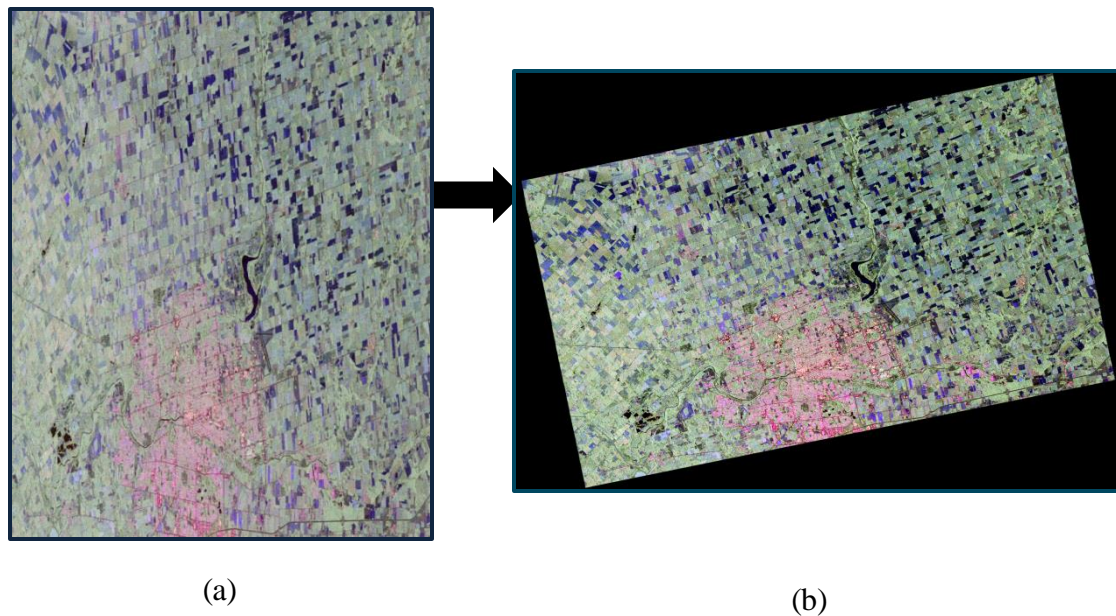
Figure 2.6 Pauli RGB image before(a) and after(b) geometric correction using MapReady

2.3.2 Classification Scheme and Training Samples

(1) Classification Scheme

A good classification scheme is required to achieve successful classification results. Theoretically, a satisfactory classification scheme should be mutually exclusive and totally exhaustive (Russel C., & Kass G., 1999). In other words, any pixel should be classified into one and only one category or class; furthermore, each LU/LC type should be considered in the classification. Ideally, a hierarchical classification scheme should be used to readily distinguish between LU/LC classes. Two or more detailed classes can be merged

into a more general category, so as to meet the required accuracy standard (Russel C., & Kass G., 1999).

In this study, LU/LC types were initially categorized into eleven classes, which include six crop types: alfalfa, grass, wheat, field peas, soybeans, corn; and four non-crop classes: forest, lawn, construction sites (CS), residential areas (RA), and commercial/industrial/institutional areas (CIIA). However, the primary objective of this research is to distinguish urban built-up from vegetation, and identify several main crop types. Therefore, post-classification methods required the aggregation of the RA, and CIIA classes into a new "built-up" category. Similarly, alfalfa and grass crop types were combined into a new forage class.

(2) Training Sample Selection

In a supervised classification, the classification algorithm should be trained to separate different classes. To achieve this purpose, representative samples, also known as prototypes, exemplars, or simply training samples, for each class of interest with ground truth are required. The training samples of each category should be representative, homogeneous, and should include the range of variability within a given category (Robert, 2007). In this study, ground truth data was acquired from the in-situ survey as well as through reference to the RapidEye optical image and the aerial photo. All the training samples for each of the eleven LU/LC types were evenly distributed and carefully selected in order to accurately represent each LU/LC type in the study area.

2.3.3   RADARSAT-2 Data Classification

Maximum Likelihood Classification (MLC) classifier is the most commonly used method adopted in supervised classification. MLC is based on the mean, variance or covariance statistics of class signal responses, and utilizes a Bayesian Probability Function which is calculated from the training samples for each class. Each pixel is then classified to the class to which it most likely belongs, based on statistical values (Jensen, 2005). In this study, MLC classifiers based on two different probability functions, (i.e. Gaussian and Wishart distributions) were applied to find the better classification method.

(1) MLC Based on Gaussian distribution

MLC classification based on Gaussian (Normal) distribution (see Function 2.8) is widely used in the optical image classification, because the distributions of each class spectral responses recorded in optical images are normally distributed (Jensen, 2005). Due to the speckle effects, the radar responses in SAR image for each class are not normally distributed. Recently, some researchers have proved that when the number of look is large enough, the Gaussian probability density distribution is a valid approximation of multi-look SAR data (Skriver, 2012).

$$G(f; \mu, \sigma) = \frac{1}{\sigma\sqrt{2\pi}} e^{-\frac{(f-\mu)^2}{2\sigma^2}} \qquad 2.8$$

In this study we found that the distributions of logarithm Pauli decomposition parameters, T11, T22 and T33 are approximate to the Gaussian distribution. As displayed in histogram of T11 (0.5|HH+VV|²), T22 (0.5|HH-VV|²) and T33 (2|HV|²) shown in Figure 2.8, the majority of the original pixels value are concentrated in the low value zone. After the logarithmic transformation, the histograms of T11, T22 and T33 became bell shaped. Moreover, the curves of histograms of T11, T22, and T33 were well-matched with the corresponding normal distribution ones. The same shapes can be observed from the histograms of other classes, as well. The marked similarity between the aforementioned curves guaranteed that the Gaussian distribution can be a valid, if not optimal, approximation of logarithm T11, T22, T33 data.

Consequently, MLC based on the Gaussian statistics was adopted for use in classifying multi-temporal polarimetric data that were derived from different decomposition parameters.
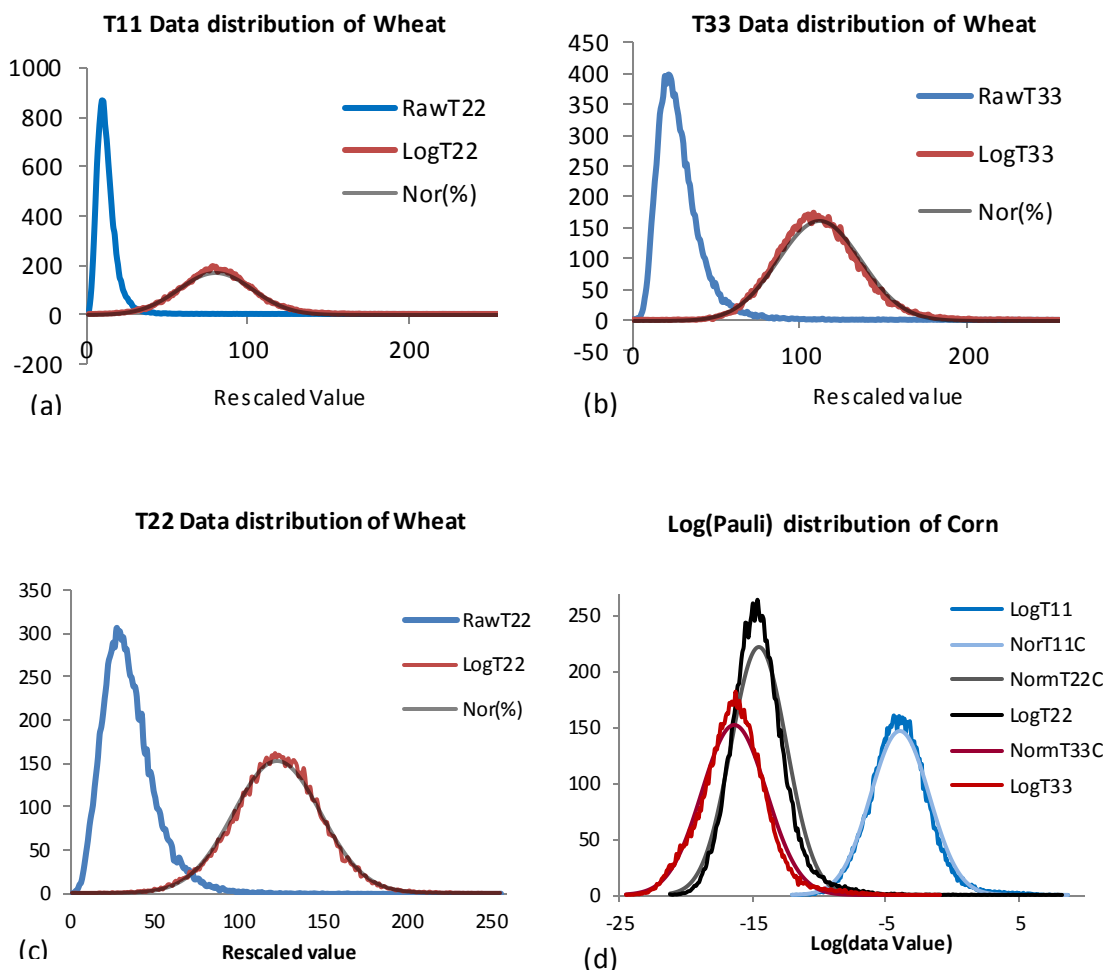
Figure 2.7 Data distributions of wheat from the raw Pauli parameters (blue), logarithm Pauli parameters (red), and simulated normal curve (black) at T11 (a), T22 (b) and T33 (c). (d) Comparison of fitted normal curves and logarithm Pauli parameters histogram curves of corn. (Nor means Normal)

(2) MLC Based on Complex Wishart distribution

Complex Wishart distribution MLC is an algorithm proposed by Lee to deal with LU/LC classification using polarimetric SAR data (Lee, et al., 1994). Similar to the MLC based on Gaussian distribution, Bayesian probability function is also adopted to determine the classification boundaries. In contrast, the probability is derived from the probability density functions of the coherency T3 (or covariance C3) matrix of polarimetric SAR data, named

complex Wishart density function. The Wishart distance measure from a pixel to a class m can be simplified as:

$$d(Z, w_m) = nTr(C_m^{-1}Z) + nln|C_m| - ln[\ P(w_m)] \qquad (9)$$

Where Z is the covariance matrix of the pixel to be classified, C_m is the average covariance matrix of the m class, n is the number of look. $P(w_m)$ is the priori probability of the class m.

MLC based on the complex Wishart distribution has been used in the classification of single polarimetric SAR imagery. Additionally, some researchers have investigated its usefulness in multi-frequency polarimetric SAR data classification (Lee et al. 1994). However, few studies have applied the Wishart supervised classifier in multi-temporal polarimetric SAR data classification (Skriver, 2012). Based on the assumption that multi-temporal data are uncorrelated, it is hypothesized that the joint probability density function will be the product of the probabilities for each image. Therefore, the Wishart distance measure for multi-temporal polarimetric SAR classification becomes:

$$D(Z, w_m) = \sum_{j=1}^{J} n[Tr(C_m^{-1}(j)Z(j)) + ln|C_m(j)|] - ln[\ P(w_m)] \qquad (10)$$

where J is the total number of images, n is the number of looks, $C_m(j)$ is the average covariance matrix of the m class in the j*th* image. $Z(j)$ is the pixel's covariance matrix from the j*th* image.

The comparison between the results generated from MLC based on Complex Wishart distribution and Gaussian distribution are explained in the Results Analysis and Discussions section.

2.3.4   Post- classification Processing

Due to the serious speckle effect impacting SAR images, the preliminary classification results are not always satisfactory, regardless of which filter are used to pre-process the imagery. Visually, a small number of isolated, generally poorly classified pixels are often located at the boundaries between two clearly assigned areas or within a large classified

area. In order to produce more accurate LU/LC maps, post-classification process is required to reduce those isolated misclassified pixels. Two commonly used post-classification methods were adopted in this study.

(1) Sieve Filter

The sieve filter functions by merging image value polygons smaller than a user-specified threshold with the largest neighboring polygon (Liu et al., 2013). In the SAR classification results, there were always some single pixels and small polygons which are misclassified. The sieve filter was particularly useful in enhancing SAR image classification accuracies.

(2) Segmentation

The segmentation post-classification method functions by grouping the pixels in the preliminary classification results into homogenous objects using segmentation algorithm in the eCognition software. Initially, the original SAR images are segmented into spectrally similar and spatial contiguous objects. Then the majority class within each object was assigned to that object in the classification results.

2.3.5   Classification Accuracy Assessment

(1) Testing Sample Selection

Testing samples are the portions of the generated land use classification map that will be selected for accuracy assessment (Russel C., & Kass G., 1999). To give a statistically valid and appropriate assessment of classification results, two vital factors of testing samples selection should be considered. One is the sample size and the other is the method of testing sample selection. Adequate number of samples per class should be gathered so that the assessment is statistically valid. Secondly, the distribution and proportion of each class should also be fully considered in order to select appropriate sampling methods..

In urban areas where the classification maps are less homogeneous than rural areas, the single pixel or clusters of pixel units are usually chosen as testing samples. In order to obtain sufficient randomly distributed testing samples, which is a basic requirement for

accuracy assessments (Jenson, 2005), a compromising option is to select a homogeneous cluster of pixels around each of the randomly distributed points.

In the rural areas that are dominated by homogenous crop fields, polygons are the most common sample units. The testing samples and training samples should be exclusive, even if they are derived from the same ground truth data.

(2) Error Matrix

The error matrix is the most widely accepted measure for LU/LC mapping accuracy (Russel C., & Kass G., 1999). As defined by Russel, "An error matrix is a square array of numbers set out in rows and columns that expresses the number of sample units assigned to a particular category in one classification relative to the number of sample units assigned to a particular category in reference data". It is a very effective way to present errors of omission and commission for individual classes. The error matrix can also be used to calculate other accuracy measures, such as overall accuracy, Kappa accuracy, producer's accuracy, and user's accuracy.

Overall accuracy (OA) is simply the sum of the number of correctly classified sample units divided by the total number of sample units in the entire error matrix. Producer's accuracy (PA) describe the accuracy of individual class from map producers' perspective. PA for each category is performed by dividing the number of correct sample units by the total number the reference data in that class. "User's accuracy" (UA) is defined from the map users' perspective. It is computed by dividing the number of correct sample of one class by the total number of samples classified to that class in the map. Kappa can be used to determine if the values contained in an error matrix represent a result significantly better than random results (Jensen 2005).While the OA is the same for two classification result, the one with higher Kappa usually has better classification accuracy.

2.4   Results Analysis and Discussion

This study was conducted following the processing procedure introduced in the Methodology section.

(1) Preprocessing

The preprocessing of multi-temporal RADARSAT-2 datasets were conducted in the PolSARpro software. Pauli, Freeman-Durden, and H/Alpha/A polarimetric decomposition parameters were generated from the coherency T3 matrix and the covariance C3 matrix. Gaussian filter at the window size of 5×5 was then applied to each of the decomposition parameters. The filtered decomposition parameters from each image were geometrically corrected and resampled into 10 meter resolution datasets, using a DEM data through the MapReady tool kit.

(2) Training Samples Selection

In order to provide enough sample units for training the classifier, over 200 polygons with over 7000 pixels were manually selected from the reference and ground truth data (see table 2.2).

Table 2.2 Number of the plots and pixels selected for each LU/LC class in the training sample units.

class	alfalfa	wheat	hay	peas	soybeans	corn	forest	lawn	CS	RA	CIIA
Plots	3	53	3	6	40	49	10	6	4	26	14
Pixels	45	762	40	71	1849	2397	695	155	158	553	524

CS: construction sites, RA: residential areas, CIIA: commercial/industrial/institutional areas.

(3) Multi-temporal dataset classification

To assess the potential of multi-temporal polarimetric RADARSAT-2 data in the urban/rural fringe area mapping, a number of classifications strategies were conducted using different RADARSAT-2 datasets (Figure 2.8). As Figure 2.8 shows, the various classifications were conducted and compared from four aspects, (1) different classifiers, (2) polarimetric parameters, (3) time selections and combinations of images, as well as (4) different post-classification processing methods.
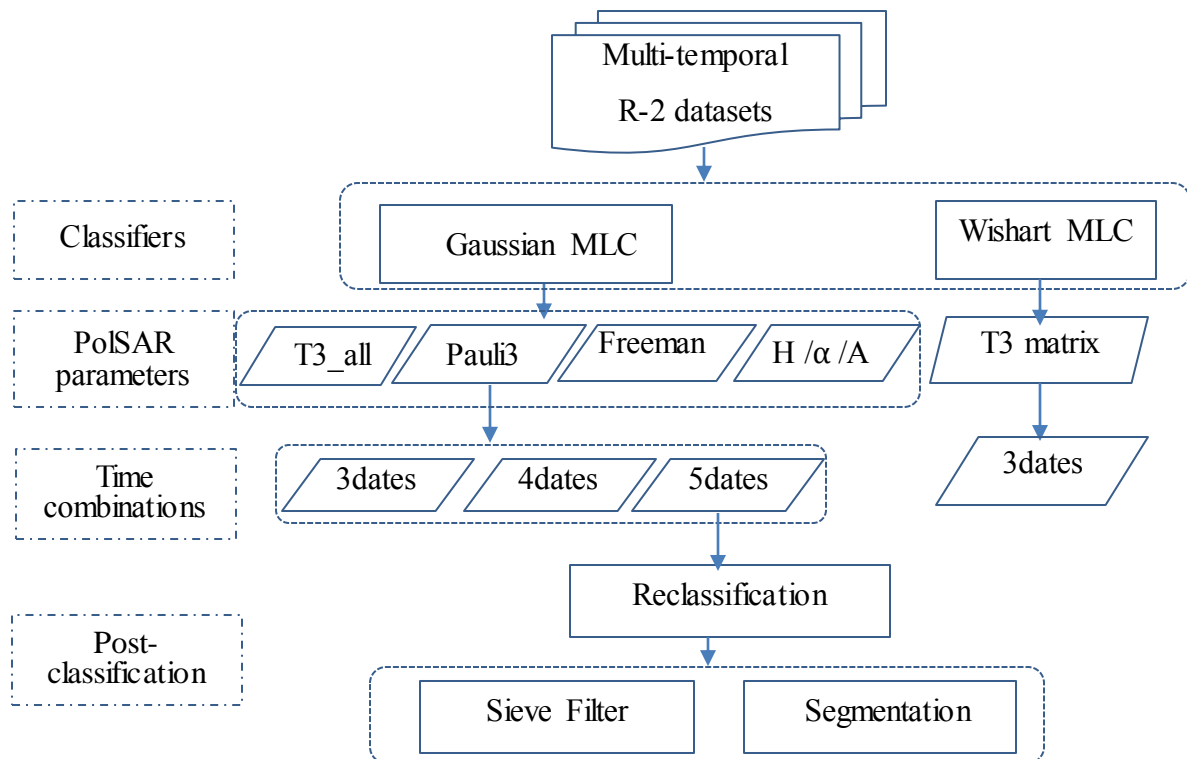
Figure 2.8 An overview of the comparisons among various classification strategies

(4) Testing Samples selection

Nine LU/LC classes, which include five crop types (i.e. forage, wheat, field peas, soybeans, corn) and four non-crop classes (i.e. forest, lawn, construction sites (CS), and built-up areas), were aggregated from the original eleven detailed classes. The hay and the alfalfa are aggregated into the forage, and the RA and the CIIA are aggregated into the built-up areas. To fully assess the classification effectiveness for each LU/LC class in

the fringe areas, two sets of testing samples were selected. For all the classes, 700 random points were generated using the PCI software, and over 500 clusters of more than 7000 pixels were selected around those points as the testing samples (Table 2.3). To test the accuracy of the classification results of the five crop types, all of the field inventory data were used for testing, with the exception those selected as training samples (table 2.4).

Table 2.3 Number of the plots and pixels selected for five crop types in the testing samples.

class	forage	wheat	peas	soybeans	corn
fields surveyed	23	44	3	63	57
pixels per class	6175	42200	6037	69311	76583
% of total	3%	21%	3%	35%	38%

Table 2.4 Number and percentage of pixels selected for the testing samples of all LU/LC classes

class	forage	wheat	peas	soybean	corn	Bups	CS	forest	lawn
Pixels #	79	765	72	1859	2395	1079	159	698	161
Class%	1%	11%	1%	26%	33%	15%	2%	10%	2%

CS: construction sites, Bups: Built-ups

(4) Accuracy Assessment

To assess classification accuracy, an error matrix for each of the classification results was generated. The advantages and disadvantages of each classification method are analyzed and discussed based on the error matrix and LU/LC maps in the following sections.

2.4.1 Training Data Analysis

To identify the separability of LU/LC different classes, the responses of polarimetric parameters to different land surfaces in different images are analyzed. Based on the training

sample units, the mean values and standard deviations of the polarimetric parameters in each image for every LU/LC class have been calculated.

(1)Pauli Decomposition Parameters

The temporal profiles of Pauli decomposition parameters (T11, T22, and T33) of RADARSAT-2 data for the six crop types were shown in Figure 2.6. Generally, the T11 represents the surface scattering and the T33 indicates the volume scattering. In T11 parameter, the separability of various crops is higher in the May 4th and June 21st images than for the other dates. However, in terms of both T22 and T33 parameters, the May 28th, July 15th, and Sept. 1st data provides higher separability between various crops.
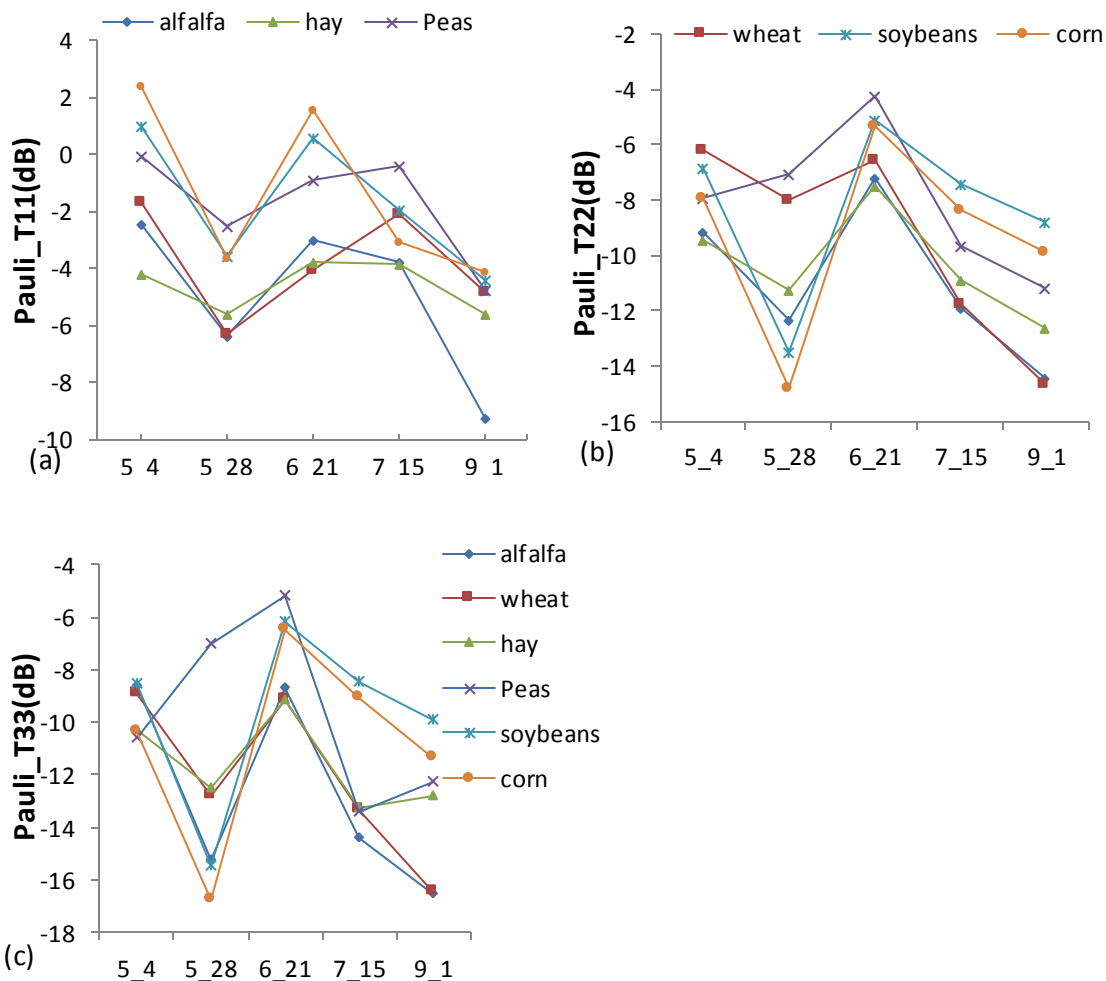
Figure 2.9 Temporal profiles of Pauli decomposition parameters value for various crop types in (a) PauliT11 single bounce, (b) PauliT22 double bounce, and (c) PauliT33 volume scattering.

For each crop type, the separability varies from parameter to parameter and image to image. For example, peas can be easily separated from other crops using T33 in the May 28th image alone. The mean T33 value of peas is at least 6 dB higher than those of the other crops. The curves of wheat, hay, and alfalfa at T11 are very close to each other, but greater difference is observed between the wheat and the hay at T22 on May 28th and also between the hay and the alfalfa at T33 on Sept. 1st. The curves of corn and soybeans are particularly different from the curves of other crops. The sharp increase of double bounce (T22) and

volume (T33) scattering from May 28th to June 21st corresponds to the rapid growth of soybeans and crop. Before May 28th, the SAR backscattering from the fields of soybeans (height<15cm) and crop (height<20cm) was dominated by the soil, according to the ground truth data. In contrast, the fields were fully covered by soybean plants (height >25cm) and corn plants (height>70cm) since June 21st. The marginal difference is observed between the soybeans and corn at T22 and T33, which might lead to the misclassification of these crops.

(2)Freeman-Durden and H/Alpha/A Decomposition Parameters

The values of Freeman-Durden decomposition parameters indicate the contributions of different scattering mechanisms, such as double-bounce, volume, and odd-bounce scattering mechanisms. In Figure 2.10(b), the mean values of Freeman volume scattering are close to each other for most classes; however, at double and odd bounced scatterings, the differences between the mean values of various classes are more significant. Figure 2.10 (a) shows that the separability of H/Alpha/A parameters between crop and non-crop types is much larger than that between agricultural crops.
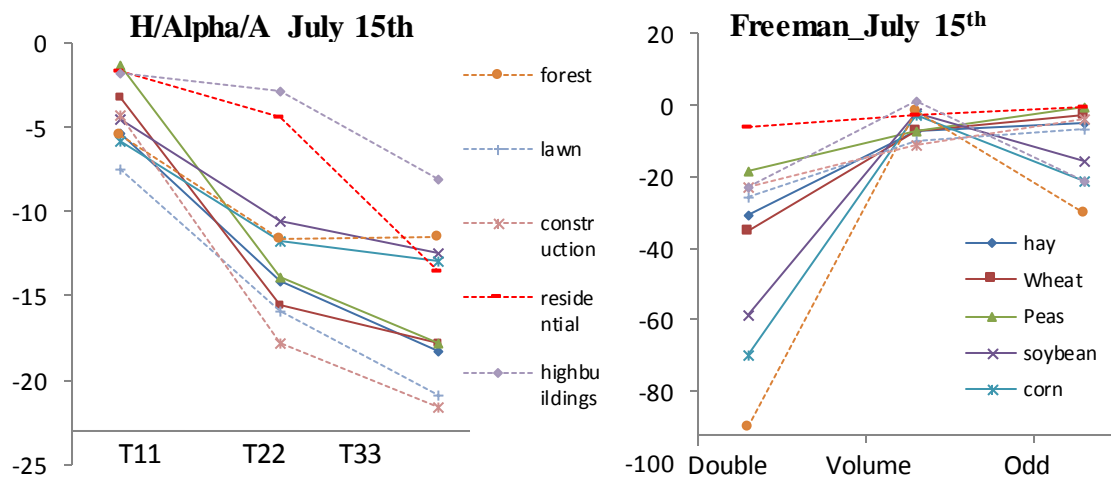
Figure 2.10 (a) H/Alpha/A (T11, T22, T33 scattering value in dB), and (b) Freeman[42] decomposition parameters (Double Volume and Odd scattering value in dB), for all the LU/LC classes on the July 15th image.

2.4.2 Classification Results Using the Gaussian and Wishart Classifier

Both Gaussian and Wishart-based methods are effective in LU/LC classification using multi-temporal RADARSAT-2. Gaussian based MLC generates a better classification results mainly in non-crop classes. Within the nine LU/LC classes used in this study, the results given by Gaussian are 86.3% (OA) and 0.83(Kappa), contrast to those given by Wishart at 78.4% (OA) and 0.73 (Kappa).

However, in terms of crop classification accuracy, the Gaussian MLC is slightly superior to the Wishart MLC. Using the five main crop type testing samples, the assessment results show that the Gaussian MLC is merely 1%(OA) and 0.01(Kappa) better than the Wishart MLC. The results revealed that the Gaussian MLC is more suitable than the complex Wishart MLC for LU/LC classification in these urban/rural fringe areas with various crop and non-crop LU/LC classes.

2.4.3 Classification Results Using Different Polarimetric SAR Parameters

To fairly compare the classification accuracy using different polarimetric parameters, the same Gaussian MLC classifier was adopted for all the classification. Classification results using four sets of decomposition parameters (i.e. coherency matrix, Pauli, H/Alpha/A, and Freeman) were compared respectively.

(1) Coherency Matrix and Pauli Decomposition Parameters

Pauli decomposition parameters (Pauli3) consist of the diagonal elements of coherency matrix (T3all). Classification results indicate that using Pauli3 outperforms those using T3all, although T3all contains more polarimetric information than Pauli3.

The classification results using the same four-date dataset shows that the results given by Pauli3 is 89 % (OA) at 0.87 (Kappa), while those by T3all is only 84.8 % (OA) at 0.81

(Kappa). For most crops (hay, wheat, and peas) and other vegetation types, such as forest, the Pauli3 gives higher accuracy than T3all in terms of both producer's and user's accuracy.

The comparison results reveal that the Pauli decomposition parameters contain the most useful polarimetric information in T3 matrix. The other off-diagonal elements in the T3 matrix introduce more noises to the classification process, rather than providing useful information.

(2) Freeman-Durden and H/Alpha/A Decomposition Parameters

The classification results using H/Alpha/A decomposition parameters are better than those yielded by Freeman-Durden decomposition parameters, but not effective in comparison to classification results obtained by using the Pauli decomposition parameters. The OA given by H/Alpha/A was 84.1% at 0.79 (Kappa), while those accuracies achieved by Freeman were merely 76.9 %(OA) at 0.71(Kappa).

(3) Separability Analysis of Different Parameters

Among the three polarimetric parameter datasets, the Pauli3 gives the best results, while the Freeman gives the lowest accuracy. The inferior performance of Freeman can be explained by the poor separability among different classes in the decomposed images. According to the concept of feature separation (Cumming and Van Zyl 1989, Shi et al. 1994), features can be readily separated, provided that the distance between the class mean values is larger than the standard deviations. Richards (Richards 1987) proposed a criteria, named the Bhattacharya distance, to quantitatively measure the separability between two classes, such as the class i and j:

$$S_{i,j} = \frac{|u_i - u_j|}{S_i + S_j}$$

(11)

Where u and s are mean value and standard deviation of the classes. The higher the $S_{i,j}$ is, the more useful the feature is in distinguishing class i from class j.

This relationship is exemplified in terms of assessing the separability between corn and soybeans classes in this study. In the same image taken on July 15th, the $S_{i,j}$ of Freeman-Durden double scattering, H/Alpha/A T22, and Pauli T22 parameter is 0.09, 0.22, and 0.36 respectively. The classification results also indicates that polarimetric parameters with higher $S_{i,j}$ value, such as Pauli decomposition parameters, generated better results.

2.4.4   Classification Results Using Different Time Combinations

Dataset with high temporal resolution are preferable for LU/LC classification, particularly for crop type identification. However, due to the limitation of the budget for data purchasing, and the limitation of image processing abilities, it is especially valuable to accurately classify crops with the least number of images. To achieve this goal, a variety of data combinations using one to five images from different dates were tested in this study. These multi-temporal classification results were assessed and compared using the same classification procedure.

(1) Overall Trends

Generally, classification accuracy increases as more dates of images are included in the classification (Table 2.5). The highest classification accuracy was achieved by using all members of the five-date dataset at 91% (OA) and 0.888 (Kappa). The best classification results generated by the four-date dataset, 90.1% (OA) and 0.877 (Kappa), which was very close to that given by five-date one. The classification results given by the three-date and two-date datasets are less satisfactory, with the highest OA being 87.8% and 83.3% respectively. In contrast, the best result generated by one-date data is as low as 62.4% (OA).

The greatest increase in classification accuracy (over 20%) is observed from one-date datasets to two-date datasets. Less than 1% increase in OA is observed between the highest four-date datasets to five-date dataset, which indicates that well-selected four-date datasets are able to generate the classification results almost as accurate as the five-date one.

The chart shows the following data table:

	1	2	3	4	5
■ 5 dates	91.0%				
■ 4 dates	90.1%	89.5%	88.8%	88.6%	88.3%
■ 3 dates	87.8%	86.3%	86.3%	86.2%	84.0%
■ 2 dates	83.3%	82.8%	78.6%	77.0%	75.5%
■ 1 dates	62.4%	59.9%	59.1%	54.5%	

Time combination sets
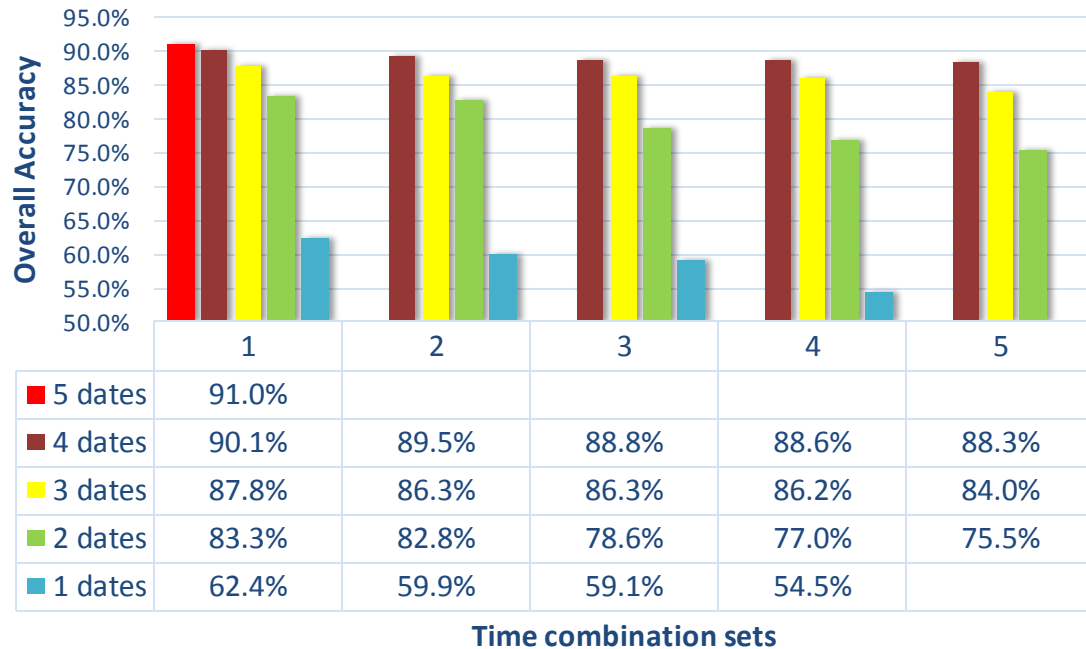
Figure 2.11 the classification result using different time combination ranking by classification OA from highest to lowest overall accuracy (%) (1 to 5).

 (2) Four-date Dataset

The overall accuracies of four-date datasets vary from 88.3% to 90.1% (see table 2.5). Among these four-date combinations, datasets without May 28th (528) or July 15th (715) image dates give the lowest overall accuracy. In other words, the May 28th and July 15th images contained the most useful information in terms of multi-temporal classification. With reference to the ground truth data, the greatest separability among various crops was also observed on image dates collected on those two periods, particularly in Mid-July, 2012.

Table 2.5 The classification results from four-date dataset by different combinations

	May 4	May 28	June 21	July 15	Sep.1	overall	kappa
Four dates	▓	▓	▓	▓		90.1%	0.877
	▓	▓		▓	▓	89.5%	0.869
		▓	▓	▓	▓	88.8%	0.86
	▓		▓	▓	▓	88.6%	0.858
	▓	▓	▓		▓	88.3%	0.855

As Figure 2.12 shows, crops in Southwestern Ontario were in different growing stages as of mid-July, 2012. Most wheat was harvested by that point in time, while forage grew very well. Field peas were withered and dry. The soybean plants could just cover the soil, and had started flowering. Corn had begun tasseling, and some of corn plants were already as tall as 2 meters.
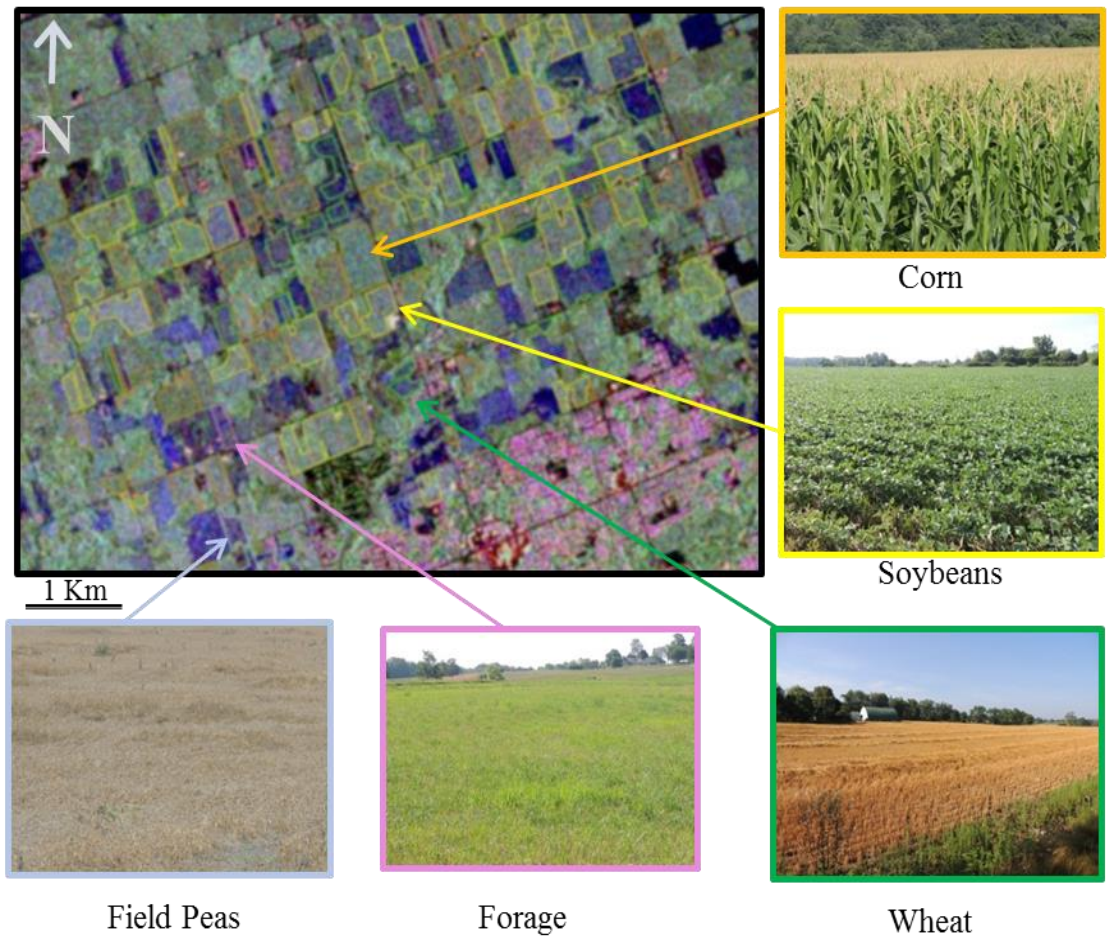
Figure 2.12 The PauliRGB composite image acquired on July 15th, 2012. Five major crop types can be identified within this image

(3) Three-date Datasets

The overall accuracies of the three-date dataset varies from 87.8% to 84.0%. As Table (2.6) indicates, the classification results given by images obtained in the early and middle growing seasons (May to July) are relatively better than those of images obtained later in the season. For example, the OA given by the three-date dataset from May 4, May 28, and July 15, is 3.8% higher than that given by the June 21, July 15, and September 1 dataset. In the early growing season, non-crop vegetation and other built-ups classes can be separated more easily from crop fields as most of the fields have not been covered by plants yet. In the late crop growing season, most crop types are either harvested or senescent, so

the crop plants are similar to each other. In addition, some dry plants might be easily confused with plant residues, which also increase the difficulty in crop separation.

Table 2.6 The classification results from three-date datasets by different combinations

	May 4	May 28	June 21	July 15	Sep.1	overall	kappa
Three dates	✓	✓		✓		87.8%	0.849
	✓	✓	✓			86.3%	0.83
		✓		✓	✓	86.3%	0.83
		✓	✓	✓		86.2%	0.83
			✓	✓	✓	84.0%	0.801

In sum, carefully selected multi-temporal dataset can improve the classification accuracy more economically and effectively than using more images. As these results indicate, satisfactory classification OA (over 87%) can be achieved using images from four-date and three-date datasets, provided that the images at key points in the growing season were included.

2.4.5 Classification Results Using Different Post-classification Processing Methods

In general, both sieve filter and segmentation methods are effective in enhancing classification accuracy. For example, the overall accuracy of five-date MLC results was 87% before any post-classification processing. The OA increased to 91% and 92% after using sieve filter (Figure 2.15) and segmentation methods respectively.

A detailed analysis of each class type revealed that while both methods are effective for most classes, some omission errors were induced in the classification of LU/LC classes and resulted in small and fragmentized patches. The forage class is a good example of this phenomenon, as some field areas of forage were so small that they were inadvertently reassigned to their neighboring classes in the segmentation. As a result, the producer's accuracy for the forage class decrease by 40%.
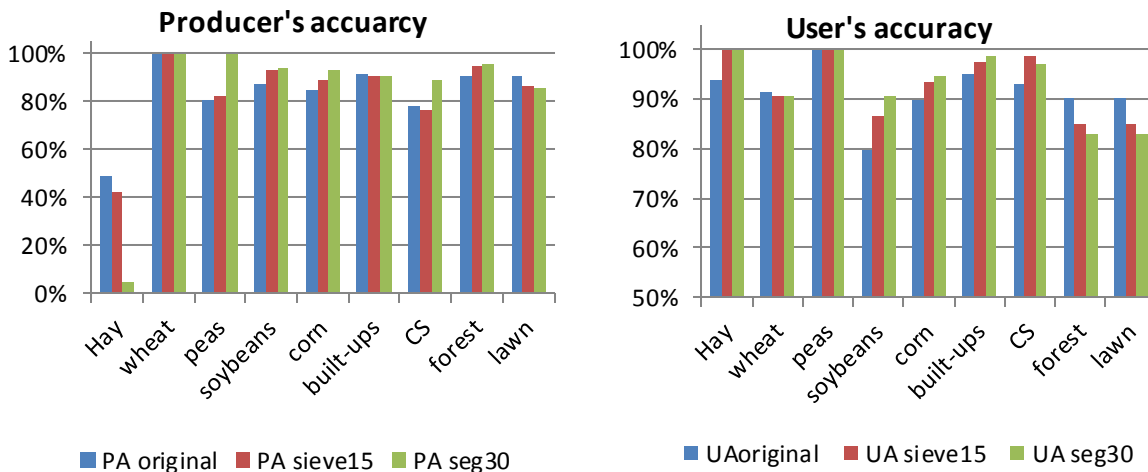
Figure 2.13 Producer's Accuracy (PA) and User's Accuracy (UA) of each LU/LC type using different post-classification processing methods

2.5   Conclusions

In summation, the capabilities of multi-temporal polarimetric RADARSAT-2 data for LU/LC classification in urban/rural fringe areas have been well proved and assessed by using the basic MLC supervised classification method in this study.

LU/LC classes in urban/rural fringe areas can be successfully identified using multi-temporal polarimetric RADARSAT-2 datasets. An accurate LU/LC map of the study area has been generated (Figure 2.13). Most non-crop classes and crop types in the rural areas have been readily separated. Within individual fields of crops, some confusions can still be observed, such as misclassifications between corn and soybeans, wheat and forage, because their phonologies are similar over the growing season. Some construction sites have been successfully detected in the north boundaries of London city, indicating the occurrence of urban expansion.
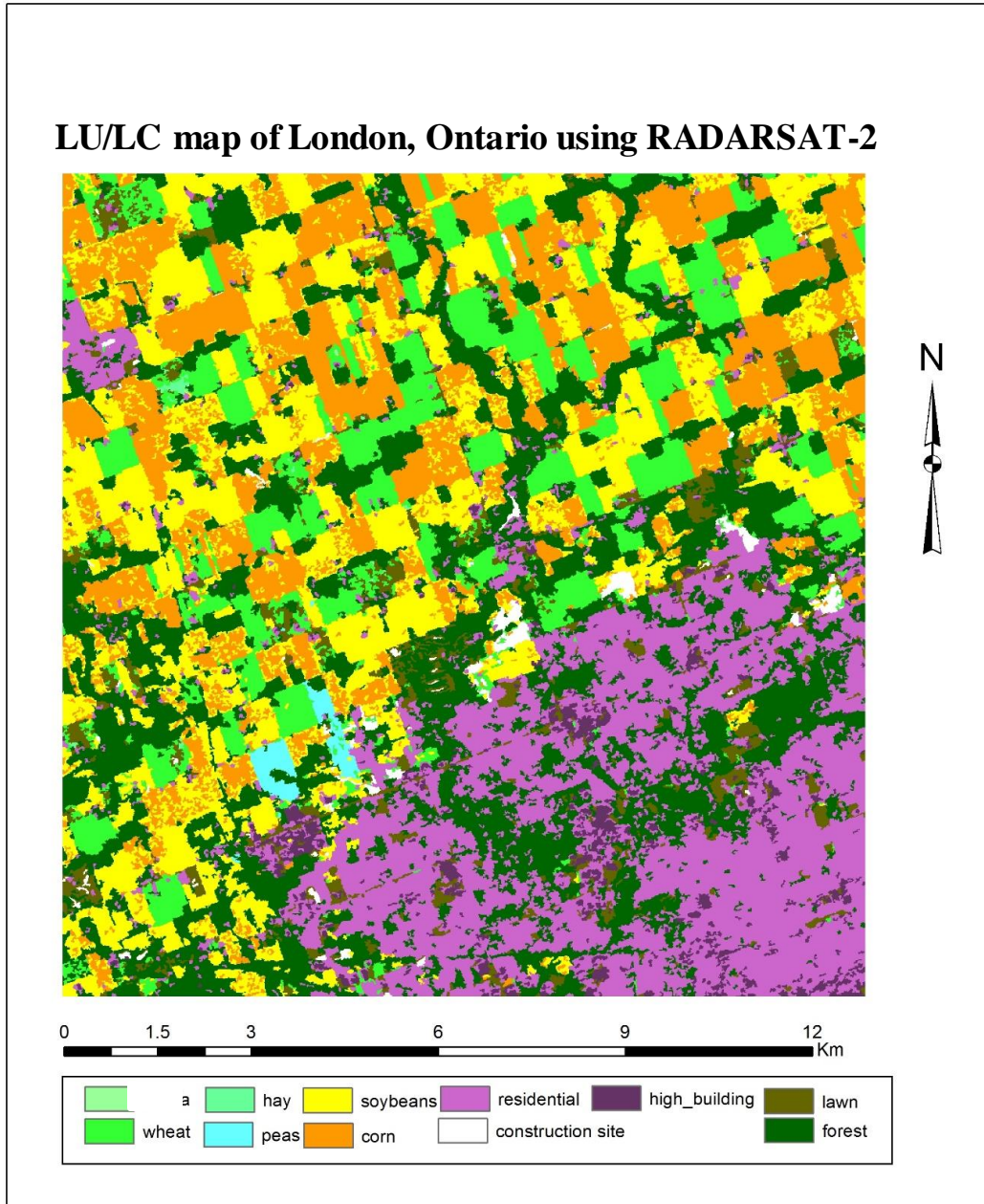
Figure 2.14 LU/LC map of the study area generated by five-date images after sieve filtering

To assess the potential of multi-temporal polarimetric RADARSAT-2 data, four aspects of classification have been evaluated: classifiers, decomposition parameters used for classification, time combinations of images, and post-classification processing methods. The major findings of this study are as follows.

(1)Gaussian based MLC is an effective classifier for Land Use and Land Cover classification in urban/rural fringe areas. Using Gaussian based MLC, the overall accuracy of 89% has been achieved with four-date RADARSAT-2 data.

(2) An appropriate decomposition method is essential for polarimetric RADARSAT-2 classification. Using Pauli decomposition parameters, the overall accuracy of classification increased by 12% comparison to Freeman-Durden decomposition parameters.

(3) The classification accuracy can still be significantly improved through carefully selecting and combining multi-date images. Although the inclusion of more dates can result in a slightly higher accuracy, satisfactory classification accuracy (over 87%) can also be achieved using images from three dates, provided that the imagery obtained at key points in the growing seasons was included.

(4) An effective post-classification processing method is also useful in improving the classification results. In this study, the overall accuracies of classification results have been improved by 5% and 4% using the segmentation and filter post-classification processing method, respectively.

The classification procedure provided in this study may have significant applications in both annual crop inventory performed with remote sensing technology, or for land use and land cover change detection in urban/rural fringe areas.

2.6 References

Chen, Z., Wang, J., 2008. A new method for minimizing topographic effects on RADARSAT-1 images: an application in mapping human settlements in the mountainous Three Gorges Area, China. Canadian Journal of Remote Sensing, Vol. 34, No. 1, pp. 13-25.

Cloude, S. R. and E. Pottier, 1996. A review of target decomposition theorems in radar polarimetry. Geoscience and Remote Sensing, IEEE Transactions on 34(2), pp. 498-518.

Cloude, S. R. and Pottier, E., 1997. An entropy based classification scheme for land applications of polarimetric SAR. IEEE Transactions on Geoscience and Remote Sensing, 35 (1).

Cover, Thomas M. and Thomas, Joy A., 2006. Elements of Information Theory. John Wiley and Sons.

Cumming, I.G. and Van Zyl, J.J., 1989. Feature utility in polarimetric radar image classification. In Proceedings of IGARSS'89, Vancouver, Canada pp. 1841–1846.

Dan Wang, Hui Lin, Jinsong Chen, Yuanzhi Zhang & Qiwei Zeng 2010. Application of multi-temporal ENVISAT ASAR data to agricultural area mapping in the Pearl River Delta, International Journal of Remote Sensing, IEEE Journal of Selected Topics in Applied Earth Observations and Remote. 31:6, pp.1555-1572data,

Desnos Y.-L., Laur H., Lim P., Meisl P., and Gach T., 1999. The ENVISAT-1 advanced synthetic aperture radar processor and data product, in Proc. IGARSS'99, Hamburg, Germany, July 1999.

Freeman, A. and Durden, S. L., 1998. A hree-component scattering model for polarimetric SAR data. IEEE Transactions on Geoscience and Remote Sensing, 36(3), pp. 963-973.

J. W. Goodman, 1976. Some fundamental properties of speckle. J. Opt. Soc. Amer., vol. 66, no. 11, pp. 1145–1150.

Jensen, J. R. 2005 . Introductory digital image processing: a remote sensing perspective. (3rd ed.). Upper Saddle River, NJ: Pearson Education Inc.

Jung, M., Henkel, K., Herold, M., & Churkina, G. 2006 . Exploiting synergies of global land cover products for carbon cycle modeling. Remote Sensing of Environment, 101(4), 534–553.

Lark, R. M., & Stafford, J. V. 1997 . Classification as a first step in the interpretation of temporal and spatial variation of crop yield. The Annals of Applied Biology, 130(1), 111–121.

Lee, J. S. 1981 . Speckle analysis and smoothing of synthetic aperture radar images. Computer graphics and image processing 17(1): 24-32.

Lee, J. S., M. R. Grunes, et al. 1994 . Classification of multi-look polarimetric SAR imagery based on complex Wishart distribution. International Journal of Remote Sensing 15(11): 2299-2311.

Lee, J.S., and Pottier, E. 2009. Polarimetric radar imaging: from basics to applications. Taylor & Francis Group, New York.

Li, J., Chen, W., Touzi, R.Optimum 2007. RADARSAT-1 configurations for wetlands discrimination: A case study of the Mer Bleue peat bog. Canadian Journal of Remote Sensing, 33 (SUPPL. 1), pp. S46-S55.

Lillesand, T. M., Kiefer, R. W., & Chipman, J. W. 2004. Remote sensing and image interpretation (No. Ed. 5). John Wiley & Sons Ltd.

Liu, C., Shang, J., Vachon, P. W., & McNairn, H. 2013. Multiyear Crop Monitoring Using Polarimetric RADARSAT-2 Data. Pp. 1-14.

McNairn, H., C. Champagne, et al. 2009. Integration of optical and Synthetic Aperture Radar (SAR) imagery for delivering operational annual crop inventories. Isprs Journal of Photogrammetry and Remote Sensing 64(5): 434-449.

Niu, X., & Ban, Y. 2013 . Multi-temporal RADARSAT-2 polarimetric SAR data for urban land-cover classification using an object-based support vector machine and a rule-based approach. International Journal of Remote Sensing, 34(1), 1-26.

Palubinskas, G., A. Makarau, 2011. Multi-sensor remote sensing information fusion for urban area classification and change detection. Multisensor, Multisource Information Fusion: Architectures, Algorithms, and Applications 2011. Bellingham, Spie-Int Soc Optical Engineering. 8064. pp. 68-78.

Qi, Z., Yeh, A. G. O., Li, X., & Lin, Z. 2012. A novel algorithm for land use and land cover classification using RADARSAT-2 polarimetric SAR data. Remote Sensing of Environment, 118, 21-39.

Richards , J.A., Woodgate, P.W. and Skidmore, A.K., 1987, An explanation of enhanced radar backscattering from flooded forests. International Journal of Remote Sensing, 8,pp. 1093–1100.

Robert A. Schowengerdt, 2007.Chapter 9 - Thematic classification, Remote Sensing (Third edition), Academic Press, Burlington, Pages 387-456,XXVII-XXXIII, ISBN 9780123694072, 10.1016/B978-012369407-2/50012-7.

Roberts, D. A., Keller, M., & Soares, J. V. 2003. Studies of land-cover, land-use, and biophysical properties of vegetation in the large scale biosphere atmosphere experiment in Amazonia. Remote Sensing of Environment, 87, 377–388.

Rogan, J., and D. Chen 2004. Remote sensing technology for land cover and land use mapping and monitoring." Progress in Planning, 61(4):301-325.Sensing (J-STARS), 4 (2), 423- 431.

Russel C., and Kass G. 1999. Assessing the accuracy of remotely sensed data: principles and practices. CRC Press,

Saatchi, S. S., Soares, J. V., & Alves, D. S. 1997. Mapping deforestation and land use in Amazon rainforest by using SIR-C imagery. Remote Sensing of Environment, 59(2), 191-202.

Shang, J., Champagne, C., and McNairn,H. 2006.Agriculture land use using multi-sensor and multi-temporal Earth Observation data. Proceedings of the MAPPS/ASPRS 2006 Fall Specialty conference, San Antonio, Texas, USA.

Shang, J., McNairn,H., Champagne, C., and Jiao X.F. 2009. Contribution of multi-frequency, multi-sensor, and multi-temporal radar data to operational annual crop

mapping. International Geoscience and Remote Sensing Symposium, Boston,7-11 July 2008,4 pp. Invited paper.

Skriver, H. 2012.Crop Classification by Multitemporal C-and L-Band Single-and Dual-Polarization and Fully Polarimetric SAR." Geoscience and Remote Sensing, IEEE Transactions on 50(6): 2138-2149.

Thenkabail, P. S., Schull, M., & Turral, H. 2005. Ganges and Indus river basin land use/land cover (LULC) and irrigated area mapping using continuous streams of MODIS data. Remote Sensing of Environment, 95(3), 317-341.

Ulaby, F. T., Kouyate, F., Brisco, B., & Williams, T. H. L. 1986. Textural information in SAR images. IEEE Transactions on Geoscience and Remote Sensing, 24, 235–245.

Weber, F., Nixon, D., Hurley, J. 2003.Semi-automated classification of river ice types on the Peace River using RADARSAT-1 synthetic aperture radar (SAR) imagery Canadian Journal of Civil Engineering, 30 (1), pp. 11-27.

Wolter, P. I., Mladenoft, D. S., & Crow, T. R. 1995. Improved forest classification in the northern lake states using multi-temporal Landsat imagery. Photogrammetry Engineering & Remote Sensing, 61(9), 1129–1143.

Woodcock, C. E., Macomber, S. A., Pax-Lenney, M., & Cohen, W. B. 2001. Large area monitoring of temperate forest change using Landsat data: Generalization across sensors, time and space. Remote Sensing of Environment, 78(1–2), 194–203.

Zhu, Z., C. E. Woodcock, 2012. "Assessment of spectral, polarimetric, temporal, and spatial dimensions for urban and peri-urban land cover classification using Landsat and SAR data." Remote Sensing of Environment 117: 72-82.

Chapter 3

3 Sensitivity of RADARSAT-2 Polarimetric SAR Data to Normalized Difference Vegetation Index and Crops Height

3.1 Introduction

3.1.1 Background

Agriculture plays a critical role in the Canadian economy, and accounts for more than 8% of Canadian Gross Domestic Product (Longtin, 2006). Acquisition of timely information about agricultural land use and land management is useful for crop yields estimation, and thus is essential for the agriculture and economic suitability.

Remote sensing technology has the capability of providing timely and wide-spread coverage of land surface information at a wide range of spatial and temporal scales. Thus, space borne and airborne remote sensing images have been widely used in agricultural applications, such as crop type inventory, soil analysis, crop condition monitoring and even yield prediction.

Traditionally, agricultural survey and crop condition monitoring was mainly dependent on in situ measurement, and thus used to be time and labor consuming. Currently, with the development of remote sensing techniques, the plant biological parameters which are observed in the field, can also be derived from remotely sensed data, and be extended to a wide area.

Optical remote sensing data have been primarily used to extract vegetation indices, such as Normalized Difference Vegetation Index (NDVI), Perpendicular Vegetation Index (PVI), Soil Adjusted Vegetation Index (SAVI), and Transformed Soil Adjusted Vegetation Index (TSAVI) (Haboudane et al. 2002; Eitel et al. 2007, 2008). These indices are proved to be sensitive to canopy characteristics, such as Leaf Area Index (LAI) and plant biochemical constituents (Viña et al., 2011). Tracking VI changes through the growing season is critical for crop growth modeling and yield forecast. Conventionally, optical data have been widely used to calculate VI (Liu et all,

2012). However, under unfavorable weather conditions, optical sensors cannot reliably meet the time requirement when information on key growing stages is needed.

3.1.2   Previous Studies

Synthetic Aperture Radar (SAR) sensors are able to transmit microwaves through the haze and clouds, and therefore offer an alternative data source for optical data. Different from traditional optical data, SAR signals respond to the crop structure (size, shape, and orientation of leaves, stalks, and fruits), the dielectric properties of the canopy, as well as the roughness and moisture of the underlying soil (McNairn et al. 2009a, Steffen et al., 2012). The existence of the connection between the SAR signals and crops parameters has been proved by previous research (McNairn et al. 2004). However, how robust the connections are have not been fully explored yet.

SAR data acquired at different frequencies have different transmission abilities, and thus are sensitive to the properties of plants at different components' scales (Lopez-Sanchez et al.2009). The selection of SAR sensors for agricultural applications is highly dependent on the crop types and task objectivities. Indeed, many successes have resulted from using multi-frequency SAR data in a wide range of agricultural applications, such as crop-type mapping (McNairn et al., 2009b, Shang et al., 2009), crop condition monitoring (Ferrazzoli et al. 1997, Paloscia, 1998), and soil moisture retrieval (Lievens et al. 2011). Baghdadi and colleagues investigated the potential of TerraSAR-X, ASAR/ENVISAT and PALSAR/ALOS for monitoring sugarcane crops. Their results show that cross polarizations at long radar wavelengths are mostly sensitive to the changes in sugarcane crops' height and NDVI early in the growing stages (Baghdadi et al. 2009). The C band SAR data was established as appropriate for biomass estimation of crops such as colza, wheat, alfalfa, and soybeans (Ferrazzoli et al. 1997). Compared to L and P band SAR data, C band has a relatively short wave length, and thus is less able to penetrate into crop plants with large biomass. Therefore, the sensitivity of C band SAR data to crop biomass is also restricted by the presence of signal saturation effects of crops with large biomass, such as the corn and sugarcane (McNairn et al. 2000).

Multipolarization SAR data provide more information about crop growing conditions than the single polarization SAR data. The potential of single polarization SAR data for crop monitoring has been well explored in the previous studies. For example, strong correlations have been reported between the HH polarization backscattering values from multitemporal RADARSAT data and biological parameters of rice, such as the plant height, age, and biomass (Shao et al. 2001, Li et al. 2003, Chakraborty et al. 2005). However, the sensitivity of the wave polarization to the orientation, shape and dielectric properties of the plants is less studied. Recently, as more polarimetric SAR data are provided by satellites such as C band RADARSAT-2, PAlSAR L band ALOS, and X band TerraSAR sensors, increasing number of studies have focused on the application of polarimetric SAR data in crop condition monitoring. Studies indicate that for both corn and soybeans, significant correlation has been reported between volume scattering indicative RADARSAT-2 Quadpol parameters and the LAI (Jiao et al. 2011). In addition, Steffen and colleagues compared TerraSAR-X Quadpol backscattering with RapidEye multispectral vegetation indices over rice fields, and the results showed that significant correlations are found between the VV images, the VH images, and the modified chlorophyll absorption ratio index/second modified triangular vegetation index(MCARI/MTVI2) on an object basis (Steffen et al.,2012).

The temporal and spatial dimensions of remotely sensed data are also critical to certain agricultural applications, such as crop phenological stages monitoring, and plant pathology detection (Lopez-Sanchez et al.2009). Most of the crops in North America change rapidly in the summer season, when weather conditions are optimal. Also, the variation of crops in the same field might also be significant. As the results of a 2007 field campaign showed, variations of 20% in LAI, 20% in vegetation height and 40% in biomass were measured within the same corn fields (Gerighausen et al., 2007). Therefore, high temporal and spatial resolution of remotely sensed data are necessary for accurate farming and other time critical agricultural applications. Several newly launched SAR sensors, such as RADARSAT-2 and TerraSAR, have short revisit intervals and fine spatial resolution, and thus are able to provide an opportunity for these applications.

3.1.3   Objectives

The objectives of this study are to investigate the potential of RADARSAT-2 polarimetric SAR data in monitoring crops growth conditions of wheat, peas, soybeans and corn agricultural crops in southwestern Ontario.

3.2   Study Areas and Data Description

3.2.1 Study Area

The study site is in Middlesex County, Ontario, Canada (43 ° 02 N, 81 ° 19 W), one of the most agriculturally productive areas in Ontario, Canada.   The terrain is generally flat. The soils are mainly Huron Lobe Glacial till with loamy and clay texture, with some stratified sand and gravel along the rivers. The climate is ideal for farming, with plenty of sunshine and precipitation. Meteorological data show that, the average monthly temperature ranged from 13 °C to 20 °C, and the monthly precipitation was 82 cm to 87 cm, during most of the crop growing season from May to September in 2012. In that same time, the mean relative humidity at 3:00 PM ranged from 55% to 60%, and monthly total hours of bright sunshine totaled between 221 and 262 hours. The main crops in this area include corn, soybeans, wheat, forage, and field peas.
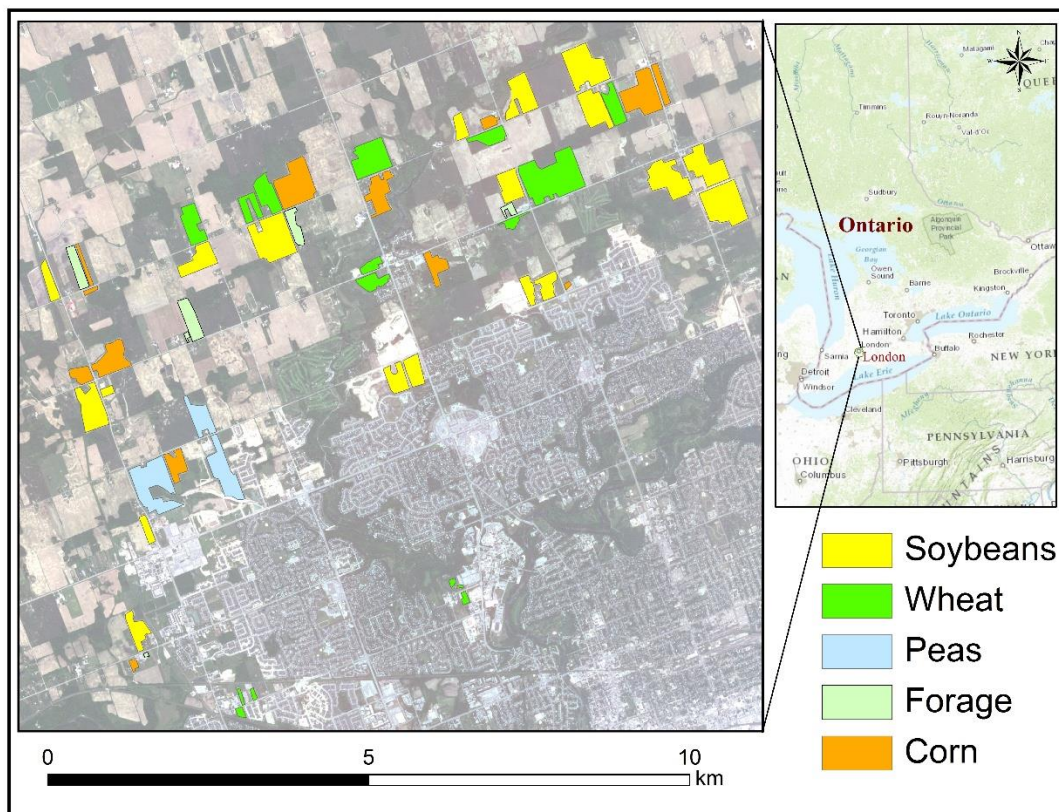
Figure 3.1 Study fields shown in the RapidEye image

3.2.2 Satellite Data

Two sets of multi-temporal RADARSAT-2 Wide Swath Quadpol data, FQ7 and FQ21, were acquired over the growing season in 2012. The FQ7 has a steeper incidence angles (25.7° - 27.6°), while the incidence angles in for FQ 21 images are much shallower (40.2°-41.6°). The nominal pixel spacing for the polarimetric SAR image is 4.7m in range and 5.1m in azimuth (Table 3.1).

During the same crop growing season, four scenes of RapidEye images were obtained (June 7th, July 20th, August.5th and August 25th). The multispectral RapidEye sensors are particularly useful in vegetation applications because they observe the Earth in a wide spatial range, with five spectral bands ranging from 400 to 850nm at 6.5m resolution at nadir.

Table 3.1 Summary of Satellite images and acquisition dates

Satellites	RapidEye	R-2 FQ7	R-2 FQ21
Dates (d-mm-yyyy)		5-04-2012	5-07-2012
	6-07-2012	5-28-2012	5-31-2012
	7-16&24-2012	7-15-2012	7-18-2012
	8-05-2012		8-11-2012
	8-25-2012	9-01-2012	9-04-2012
			9-28-2012

3.2.3 Field Work

The in situ measurements were taken coincident with the satellites overpasses. Measurement were conducted on per-fieldbasis. The crop fields selected in this study area are representative of the main crops in Southwestern Ontario. Within the study area, 13 corn, 19 soybeans, and 16 wheat croplands, 6 forage and 3 peas' fields were selected in the study area. The polygons for each field were manually drawn from the RapidEye images.

In each field, the general crop condition information has been investigated, which includes the field management information, crop phenological stages, height, and general soil conditions. Height information is one of the most important characteristics in describing the plant growing conditions. The plants' heights are usually homogenous for the most of the fields, and thus were measured by averaging three samples in each individual field. As SAR signals might be responsive to the soil moisture, the soil wetness are also recorded in each field on every imagery acquisition date. Soil conditions are briefly measured by hand and recorded in five categories: dry, slightly moist, moist, wet, and extremely wet soil conditions.

The meteorological information is very useful in analyzing the SAR signal, which is sensitive to the moistures in the land surface. Detailed meteorological information was downloaded from the environmental Canada. Hourly weather information on the image acquisition date were recoded, such as participation, temperature, wind, and pressure.

3.3   Methodology

The methodology of this study can be separated into three main steps (Figure 3.2): (1) RADARSAT-2 polarimetric data decomposition; (2) NDVI mapping and segmentation; (3) Correlation analysis between crop parameters (height and NDVI) and polarimetric parameters. The detailed concepts and methods are explained as below.
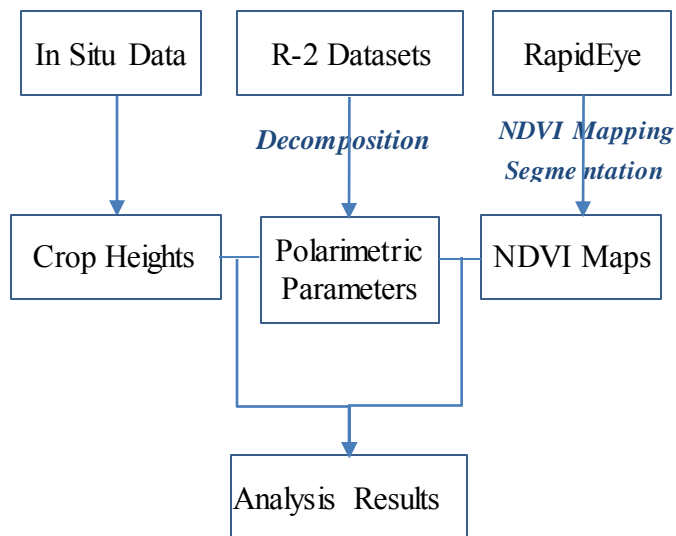
Figure 3.2 The methodology of the data processing and analysis

3.3.1 Polarimetric Data Processing

The polarimetric information contained in the RADARSAT-2 data is related to the crop parameters, such as crop height, density, moisture, as well as the canopy structures. Using polarimetric decomposition methods, a variety of parameters can be extracted from the original RADARSAT-2 datasets. Different parameters contain different physical meaning, and thus each of them might have different sensitivities different crops. Among all the polarimetric parameters, the most commonly used one can be separated into two main categories: (1) the basic polarimetric parameters (2) and decomposition parameters.

(1) Basic Polarimetric Parameters

T3 coherency and C3 covariance matrix are fundamental matrices, from which other decomposition parameters can be derived (Lee and Pottier, 2009). Among all the

parameters in T3, the diagonal parameters T11 (|HH+VV|), T22 (|HH-VV|), and T33 (|HV|) contain the most useful polarimetric information. The widely used Pauli decomposition is based on the T3 matrix. Each of the parameters has clear physical meaning: T11 represents single (odd) bounce scattering, T22 indicates double bounce scattering, and T33 is associated with volume scattering (Lee and Pottier, 2009).

From the C3 matrix, the intensities of different polarization bands can be extracted from the diagonal parameters. C11 (|HH|) and C33 (|VV|) represent the horizontal and the vertical polarization band intensity, respectively. C22 (|HV|) is similar to T22, which indicates the intensity in volume scattering.

The intensity ratios are also sensitive to the canopy characteristics of different crops at various growing stages. Three main intensity ratios have been studied in this study, which includes HH/VV, HV/HH, and HV/VV polarizations.

(1) Polarimetric Decomposition Parameters

The Freeman-Durden decomposition is a method for fitting a physically based, three-component scattering mechanism model to the polarimetric SAR observations. The three-components scattering mechanism model includes surface, double-bounce and volume scattering mechanisms (Freeman et al., 1998; Lee and Pottier, 2009). This approach can be used to determine the dominant scattering mechanisms in the land surface. In the crop growing season, the dominant scattering mechanisms in the crop land would change according to the plant development. Therefore, the decomposition results from Freeman-Durden might related to the crop growing stage and crop conditions.

(2) H/Alpha/A Decomposition

H/Alpha/A decomposition is an approach proposed by Cloude and Pottier for extracting average parameters from experimental data using a smoothing algorithm based on second-order statistics (Cloude and Pottier, 1996; Cloude and Pottier, 1997). Decomposition parameters are generated from an eigenvector analysis of the coherency matrix T3. The eigenvectors describe different scattering processes, and the eigenvalues indicate their relative magnitudes. Among all the parameters, the averaged Alpha angle (α) relates

directly to underlying average physical scattering mechanisms. The value of Alpha ranges from 0 ° to 90 °, which indicates the variance of dominant scattering from surface scattering mechanism moving into single scattering by a cloud of anisotropic particles, and finally reaching dihedral scatters. Entropy (H) describes the randomness of the scatter. The anisotropy (A) corresponds to the relative power of the second and third eigenvectors (Lee and Pottier, 2009).

Among the three H/Alpha/A decomposition parameters, H has been reported to be most sensitive to the density and randomness of some plants canopy (Lee and Pottier, 2009, McNairn et. al, 2009). The sensitivity of H to crop parameters, such as height and NDVI, has not been fully investigated yet, and thus requires further study.

(3) Pedestal Height and Span

Pedestal height is another way of measuring randomness in the scattering. Pedestal height is equivalent to measuring the ratio of the minimum eigenvalue to the maximum eigenvalue. It is an indicator of the presence of an unpolarized scattering component in the received signal, and thus is related to the degree of polarization of a scattered wave (Lee and Pottier, 2009). Span is a measurement of total power by adding all the intensities from different polarization bands.

As the Figure 3.3 show, in this study, all the parameters were extracted from the filtered multi-temporal RADARSAT-2 polarimetric data. After the decomposition, all the data are orthorectified and registered together. Each step of the polarimetric data pre-processing is conducted using the PCI Geomantica 10.3 software and the additional Polarimetric SAR Work Station.
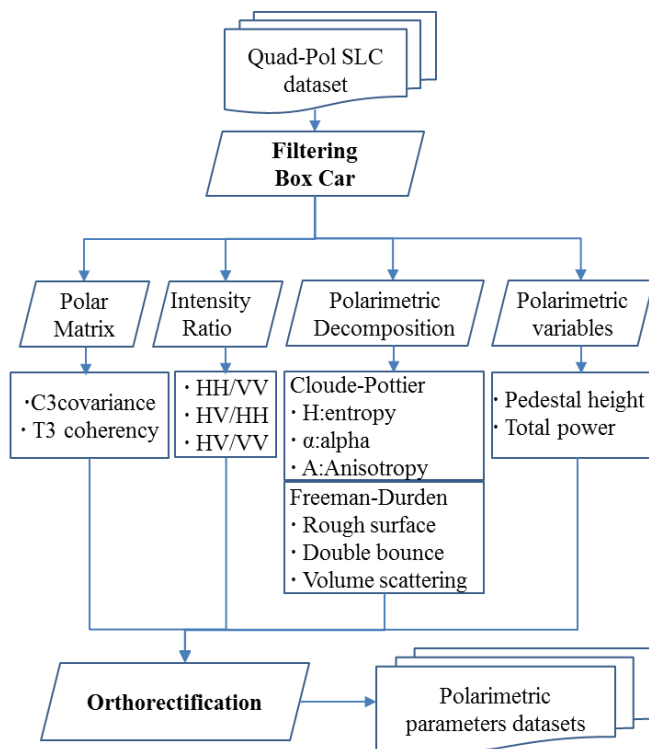
Figure 3.3 Flowchart shows the workflow used to process the polarimetric RADARSAT-2 datasets.

3.3.2 NDVI Calculation

Normalized Difference Vegetation Index (NDVI) is one of the most commonly used vegetation indices derived from optical Remote Sensing data. It is calculated from the visible and near-infrared (NIR) light reflected by vegetation (Rouse et al., 1974). NDVI is able to reflect the health conditions of vegetation because healthy vegetation absorbs most of the visible light that hits it, and reflects a large portion of the near-infrared light. However, unhealthy or sparse vegetation reflects more visible light and less near-infrared light. The normalized difference between NIR and Red reflectance (Function 3.1) is able to characterize the healthiness of vegetation.

The RapidEye images have a wide coverage of NIR and visible spectral wavelength, and thus have great potential in vegetation indices derivation. However, due to the different atmospheric condition of each image taken at different time, using the original digital number is not accurate enough to derive high quality NDVI maps. Atmospheric Correction

of optical data is necessary prior to NDVI calculation, as the calculated reflectance in each band from multi-temporal images only become comparable the atmospheric correction. In this study, the atmospheric correction module ATCOR, which is embedded in PCI software, has been used to perform the correction.

Pixel based analysis of the sensitivities between polarimetric parameters and vegetation indices is usually unstable due to the serious speckle effects in the SAR images. Therefore, the object unites are adopted in this study to investigate the relationship between polarimetric SAR parameters and NDVI.

In the course of this study, NDVI maps were segmented into homogenous zones using the multi-resolution algorithm in eCognition software. As the crop growing conditions vary a lot from day to day even within the same individual crop land, each NDVI map generated from different images should be segmented independently. The mean values of the NDVI and polarimetric parameters within each of the homogenous zones were extracted for the correlation analysis.

$$NDVI = \frac{\rho_{NIR} - \rho_{Red}}{\rho_{NIR} + \rho_{Red}} \qquad (3.1)$$

Where ρ_{NIR} and ρ_{Red} are the reflectance in NIR and Red bands.

3.3.3 Correlation Analysis

The widely used Pearson product-moment correlation coefficient (Pearson's r) is utilized in this study for correlation analysis (Wilcox, 2005). Pearson's r is a measure of the linear correlation (dependence) between two variables X and Y, giving a value between +1 and −1 inclusive (see Function 3.2).

$$\rho_{X,Y} = \frac{cov(X,Y)}{\sigma_X \sigma_Y} = \frac{E[(X - \mu_X)(Y - \mu_Y)]}{\sigma_X \sigma_Y} \qquad (3.2)$$

In this study, the Pearson's r between NDVI and SAR parameter is defined as the covariance of the two variables divided by the product of their standard deviations.

The absolute values of Pearson's r are less than or equal to 1. The higher the absolute value of Pearson's r, the stronger the correlation between two variables.

3.4   Results and Discussion

This study was conducted from three aspects as mentioned in the methodology section.

(1) The crop height information was measured from each of the cropland at every image acquiring date. The crop phenological information was observed in the field. The vegetation characteristics changes were also tracked and analyzed based on the field measurements results.

(2) The NDVI maps were first generated from RapidEye maps, and then segmented into homogenous objects. Over 1000 objects, with similar NDVI values in the same object have been extracted for the sensitivity analysis.

(3) A high dimension of polarimetric dataset was derived from the multi-temporal RADARSAT-2 data. The responses of those polarimetric data to the vegetation parameters (both height and NDVI) at two different image incidence angles (FQ7 and FQ21) were analyzed respectively.

Detailed analysis of study results are discussed below.

3.4.1 Field Data Collection

Over 20 times of field work were conducted from early May to the end of September. Plant height, one of the most important pieces of crop information, has been carefully recorded (See Appendix 2.4).

(1) Corn and Soybeans

Six stages of corn growth have been captured, from the end of May to the end of September: stalk initiation, stalk development, tasseling and flowing, ear development, kernel development, and maturation (Figure 3.4). The height of corn starts to increase dramatically in the end of May when the corn began to initiate (20cm) and the growth rate slowed down with when the corn started to tassel in the middle of July (200cm).

For the soybeans, five images taken at different soybean growing stages are presented in Figure 3.4. The average soybean height varied from 20cm in late June to 70cm in early September. Most soybeans were planted in late May. On June 24th, the two-trifoliate was fully developed for the majority of the soybeans. The height of soybeans increased continually through the stages of flowering and bean filling. Average soybean height peaked when leaves began shedding in early September, and decreased by 5cm when the soybeans matured.

| Corn May31 | Corn June24 | Corn July 18 | Corn Aug.11 | Corn Sept.28 |

| soybeanJune24 | Sb Jul 18 | Sb Aug 11 | Sb Sept.4 | Sb Sept.28 |
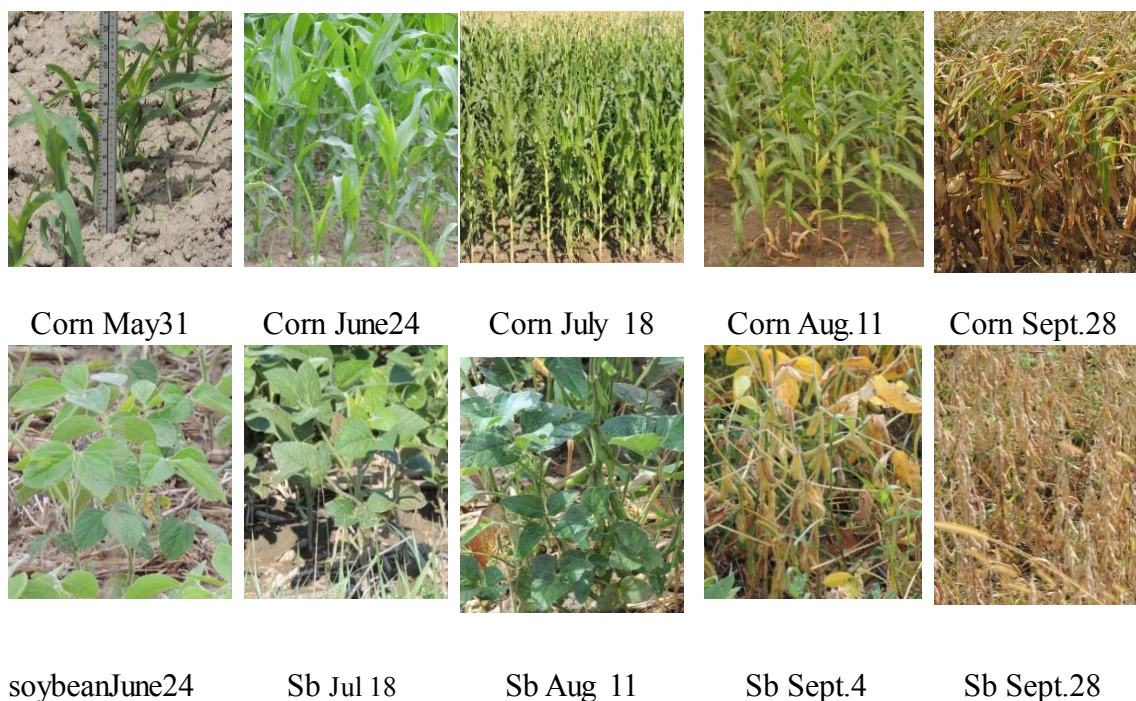
Figure 3.4 Key crop growing stages for corn and soybeans during the growing season

(2) Wheat and Field peas

Four main growing stages of wheat were captured by the RADARSAT-2 images taken from early May to mid-July, 2012 (Figure 3.5). The height of wheat increased rapidly from the tiller formation stage in early May at 30cm, and reached a peak of 75cm at heading and flowering stages by the end of May. Most wheat began to ripen at the end of June, and were harvested in the middle of July.

The development stages of field peas in 2012 were similar to those of wheat. The majority of pea plants emerged in early May, and bloomed in early June. The pea pods were fully developed at the end of June, and were finally harvested in the middle of July (Figure 3.5). Over the whole growing season, the height of field pea plants varied from 10cm to 55cm (Figure 3.5).

| Wheat May 7 | Wheat May 31 | Wheat June 24 | Wheat July 18 |

| Field Peas May 7 | Field Peas May 31 | Field Peas June 24 | Field Peas July 18 |
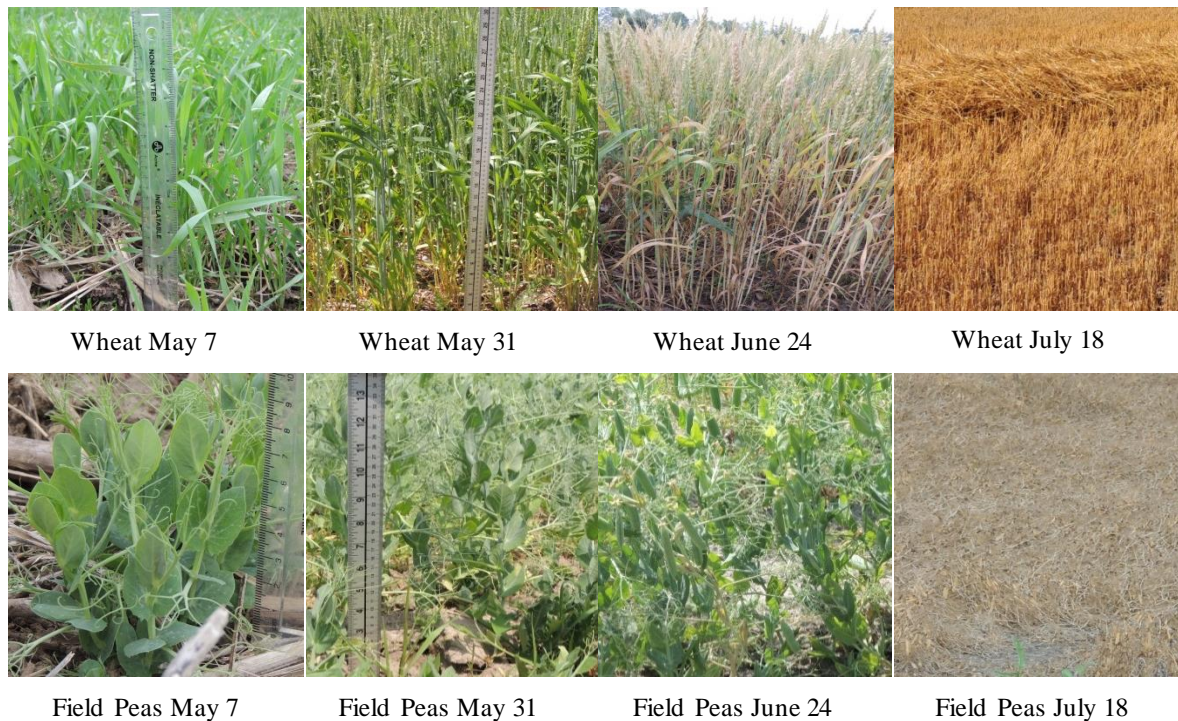
Figure 3.5 Key crop growing stages for wheat and field peas during the 2012 growing season

3.4.2 Correlation Analysis between RADARSAT-2 Polarimetric SAR Data and Crop Height

The correlation between crop height and RADARSAT-2 polarimetric parameters are summarized in Table 3.2. The average heights of each crop field were observed in the field at each satellite passing day. The mean values for each SAR parameter at corresponding places in the field were extracted from the polarimetric parameters datasets.

(1) Overall Trend

Relative high correlations(r) were observed in corn and peas. The high value of r ranged from 0.7 to 0.8. For soybeans and wheat, the correlations were relatively low, with the r less than 0.6. To further investigate the relationship between crop height and SAR parameters, one typical field for each crop was selected for detailed analysis.

Table 3.2 The correlation between crop height and SAR parameters

	Corn	Soybean	Wheat	Field Peas
Linear Backscatter coefficient(dB)				
C11(HH)	0.57	0.41	-0.49	0.26
C22(HV)	0.68	0.52	-0.57	0.82
C33(VV)	0.47	0.35	-0.20	0.54
T11(HH+VV)	0.36	0.23	-0.40	0.54
T22(HH-VV)	0.70	0.56	-0.36	0.31
Intensity ratio				
HH/VV	0.51	0.16	-0.22	-0.46
HV/HH	0.43	0.45	-0.15	0.82
HV/VV	0.67	0.49	-0.56	0.51
Freeman-Durden decomposition parameters				
Single	-0.61	-0.38	0.15	-0.26
Double	-0.49	0.24	0.17	-0.72
Volume	0.68	0.52	-0.57	0.82
Cloude-Pottier decomposition parameters				
Entropy	0.79	0.42	-0.05	0.18
Alpha (deg.)	0.79	0.47	-0.11	0.01
Anisotropy	0.04	-0.23	0.51	-0.75
Polarimetric variables				
PH	0.71	0.54	-0.40	0.62
Total power	0.59	0.44	-0.45	0.59

(2) Corn

The volume scattering indicative parameters, such as HV and the volume scattering from the Freeman-Durden decomposition parameters, are sensitive to the corn height. The volume scattering values increased as the corn height increased. Large amount of rainfall accumulated on June 24 might also contribute to the high volume scattering value.

The Entropy and Alpha parameters were more sensitive to the change in corn height (r=0.79) than the other parameters. The variation of the corn height was well characterized by the change of Entropy value, even at the late of corn growing season. A minor decrease of Entropy was observed at the corn maturation stage, which might be a result of the withering of most leaves.

The change of Alpha angle indicates the change of dominant scattering mechanism. In the early stage of the corn growing season (stalk initiation and development) the dominant mechanism was surface scattering since the plants could barely cover the ground. The Alpha increased from 40 to 50 degrees during the period from the tasseling to the maturity of corn, which indicates that volume scattering was the main scattering mechanism in the corn fields. High canopy densities of corn were also observed in the in-situ investigation during that period. At the corn maturation stage, the Alpha was approaching to 50 degrees, which indicated that increasing double bounce scattering was also observed. As the canopies were less dense than before, more reflectance was backscattered from the semi-double-faced geometry between stalks of corn and the surface.

In sum, both Entropy and Alpha angle from Cloud-Pottier decomposition parameters and HV scattering are good indicators of corn height.

(3) Soybeans

The values of both Pedestal height (Ph) and HH-VV (T22) correlated well with the height of soybeans. Pedestal height is an indicator of the presence of an unpolarized scattering component, and the randomness of scattering. A high pedestal height value indicates that the volume scattering or multiple-surface scattering is the dominant from of scattering in

the targets. Researchers reported that (Evans, et al. 1988) Pedestal height was directly proportional to vegetation density.
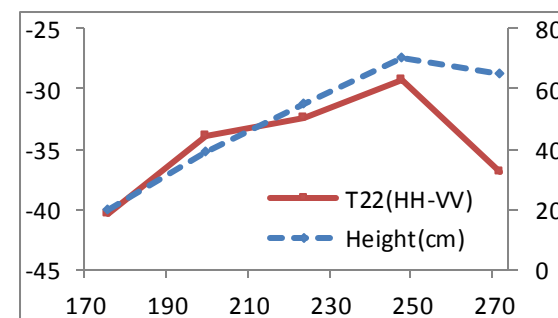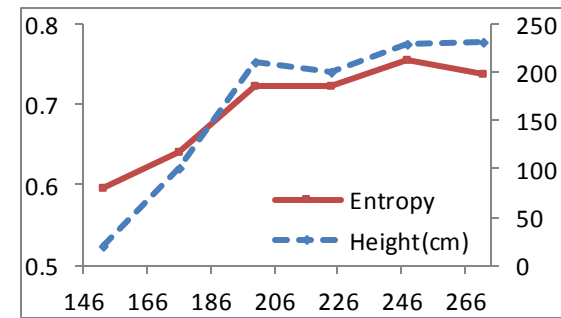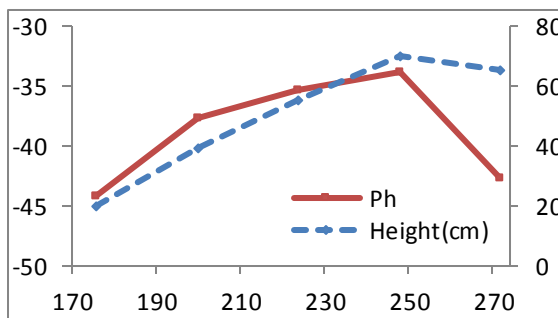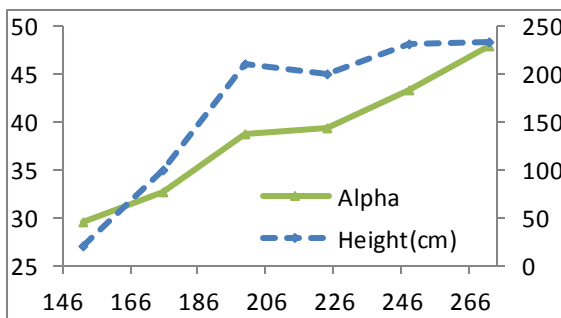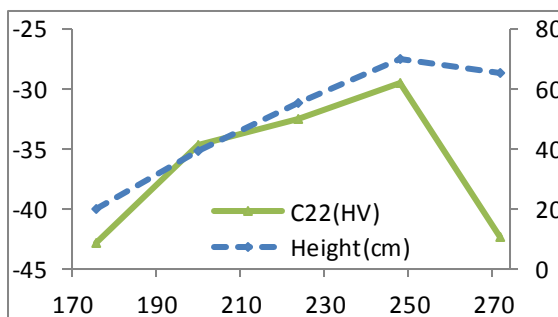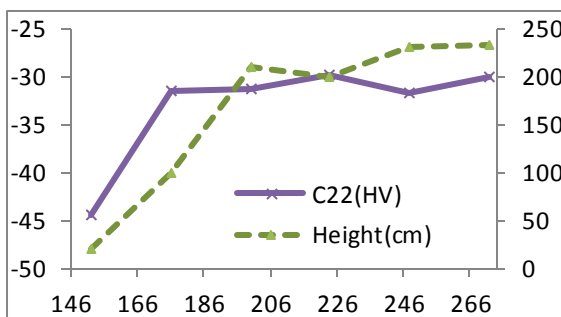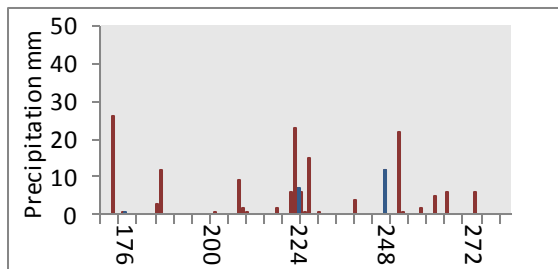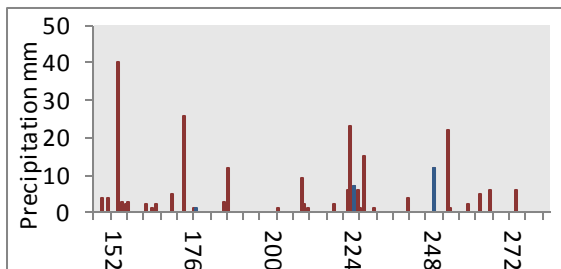
Day of Year 2012 over corn

Day of Year 2012 over Soybeans

Figure 3.6 Temporal evolution of the SAR responses over corn and soybeans. SAR parameters are presented together with crop height and precipitation amounts.

The sensitivity of Ph to soybean height was observed in this study. However, the decrease in Ph value was much greater than the drop of height after the maturation of soybeans. Over the course of growing season, the foliage of most soybean plants became sparse as most leaves defoliated at the maturation stages. The decrease of soybean plant density resulted in the decrease of overall crop density, and consequently a decrease in Ph value. Similar results were also observed in the HV and HH-VV parameters, which are the indicators of volume and double scattering, respectively.

(4) Wheat and Field Peas

Figure 3.7 shows that the backscattering in the HH polarization channel of RADARSAT-2 is negatively correlated with the wheat height. HH is an indicator of surface scattering. The value of HH decreased as the wheat leaves and stems developed, and dropped to the lowest value when the biomass was at its highest. The temporal change in HH indicated that, as wheat grew, the signals scattering from the underlying bare soil were less intensive. The value in the Anisotropy of Cloude-Pottier decomposition is positively correlated with the wheat height. Anisotropy represents the relative power of the second and third eigenvectors of the covariance matrix.

The value of HV and the HV/HH positively corresponded to the growth of the peas. The rise in the value of HV/HH and HV indicated that volume scattering, instead of surface scattering, became the dominant component as the pea's biomass increased.

(a) Day of Year 2012 over wheat (b) Day of Year 2012 over peas
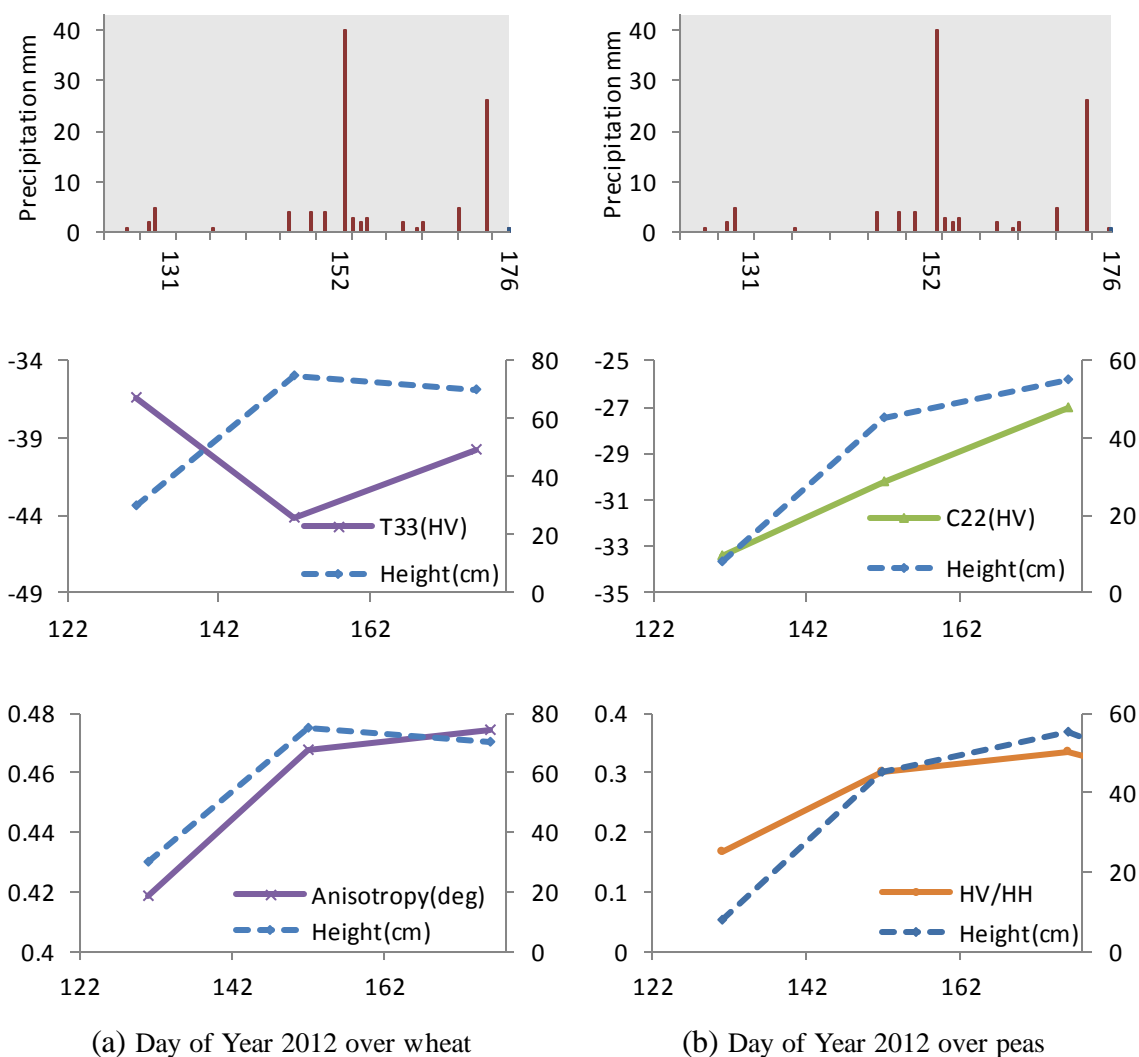
Figure 3.7 Temporal evolution of the SAR responses over wheat (a) and peas (b). SAR parameters presented together with crop height and precipitation received.

3.4.3 Correlation Analysis between RADARSAT-2 Polarimetric SAR Data and Crop NDVI

The NDVI maps of both soybeans and corn crops were generated from multi-temporal RapidEye images. The segmentation results give the basic units for the correlation analysis. In the following sections, (1) the NDVI segmentation results, (2) the correlation between NDVI and basic polarimetric parameters, as well as (3) the correlation between NDVI and polarimetric decomposition parameters, were analyzed and presented.

(1) NDVI Segmentation

The statistics between NDVI and RADARSAT-2 polarimetric parameters were conducted on the object level. Four NDVI maps were generated from the images acquired on the dates of June 7th, July 16th and 24th, August 5th, and August 25th, 2012. Each NDVI map was segmented into homogeneous objects at the scale of 15(Table 3.3). The number of objects included in the statistics is 212 for June 7th, 365 for July 16&24th, 382 for August 5th, and 295 for August 25th. The correlation analyses were independently conducted for the fields of corn and soybeans using the images taken on the FQ7 or FQ21 angle.

Table 3.3 Samples show the segmentation results for soybeans and corn fields superimposed on the June 7th (a), July 16th and 24th (b), August 5th (c), and August 25th (d) 2012, NDVI maps.

(a)soybean	(b)soybean	(c)soybean	(d)soybean
(a) corn	(b)corn	(c)corn	(d) corn

NDVI:1   0

0   250   500   1,000   Meters
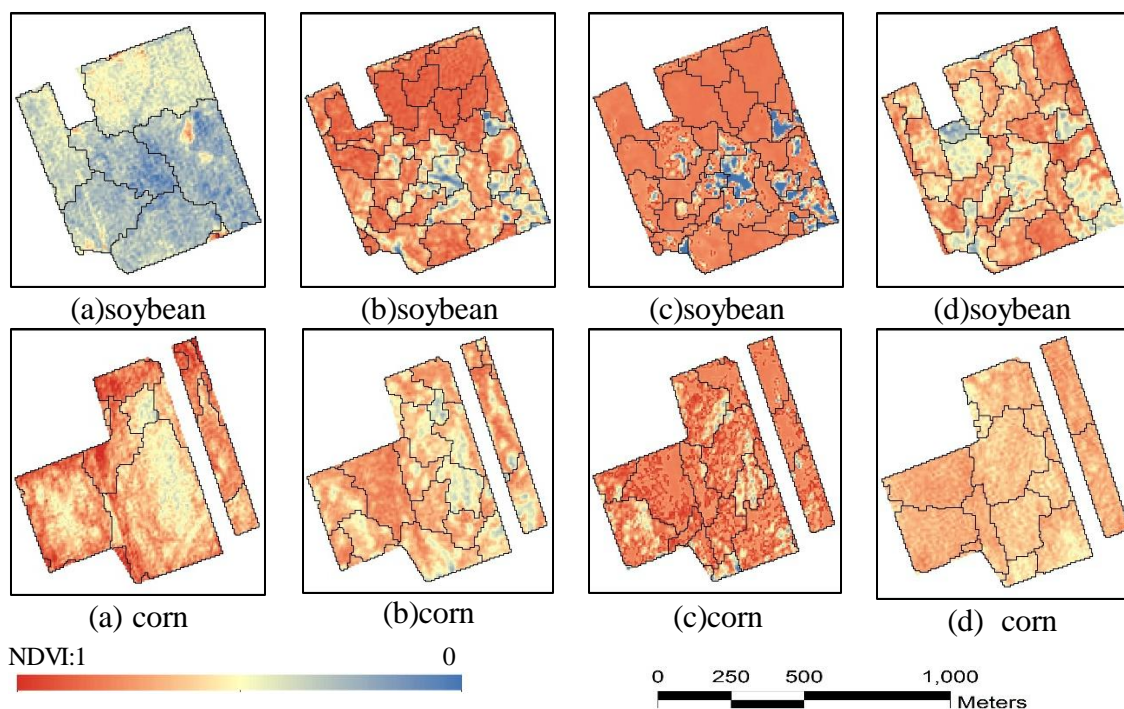
3.4.3.1   Basic Polarimetric Parameters

For both corn and soybean crops, significant correlations between HV and NDVI were observed at FQ7 and FQ21 images. Also, strong correlations were observed between the T22 (HH-VV) and the NDVI at FQ7 (r= 0.89 for corn, 0.9 for soybeans). At FQ21, however, the correlations between T22 (HH-VV) and NDVI was slightly lower for both corn(r=0.83)

and soybeans(r=0.83). In Figure 3.8, the HV and HH-VV parameters are plotted against NDVI for both corn and soybean crops. HV is associated with volume and HH-VV represents double or even-bounce scattering from within the target. The significant correlation between HV, HH-VV and NDVI reflects that both HV and HH-VV are sensitive to the physical structure of crops. Early in the crop growing season, most scattering originated from the soil surface. Thus, both volume and multiple scatterings were low during that period. With the growth of leaves and stems of plants as the crop matured, more scattering was resulted

Table 3.4 The correlation between soybean and corn NDVI to basic polarimetric parameters in FQ7 and FQ21

	R(FQ7, NDVI)		R(FQ21,NDVI)	
	Soybean	Corn	Soybean	Corn
Linear Backscatter coefficient(dB)				
C11(HH)	0.42	0.56	0.80	0.79
C22(HV)	0.93	0.92	0.89	0.93
C33(VV)	0.43	0.43	0.79	0.75
T11(HH+VV)	0.25	0.38	0.73	0.75
T22(HH-VV)	0.89	0.90	0.83	0.83
Intensity Ratio				
HH/VV	-0.90	-0.80	-0.07	0.48
HV/HH	0.63	0.74	0.67	0.65
HV/VV	0.76	0.78	0.63	0.73

The saturation of HH-VV to NDVI was observed once the NDVI reached 0.8 at the FQ21 angle for both soybean and corn crops (Fig 3.8). As Fig 3.8 (f) shows, once the NDVI in the corn fields were higher than 0.7, the positive correlations between T22 and NDVI disappeared. The low correlations might be explained based on the principle that after the maturation of most corn, the NDVI decreased due to the drop in chlorophyll in the plant. In the meantime, the occurrence of double bounce scattering increased when most leaves were dry. Stronger signals were reflected from the semi-double-faced geometry between

corn stalks and soil surface. For the soybeans, the sensitivity of HH-VV to NDVI matured when the NDVI values were higher than 0.8, particularly in FQ21 images. The FQ21 images were taken in a shallower incidence angles, and were less able to penetrate into the canopy. Therefore, parameters derived from FQ21 images are less sensitive to NDVI than those from FQ7.

(a)

(b)

(c)

(d)
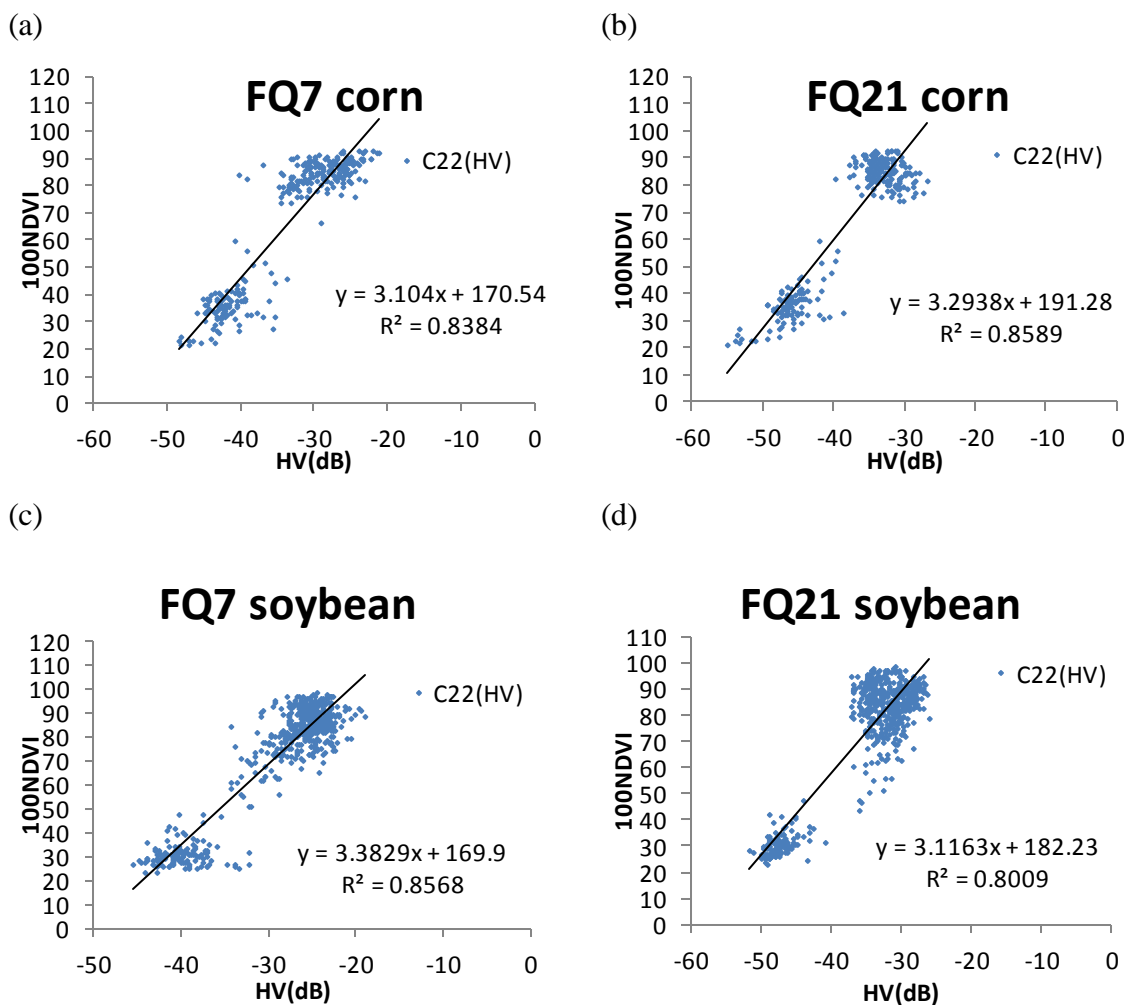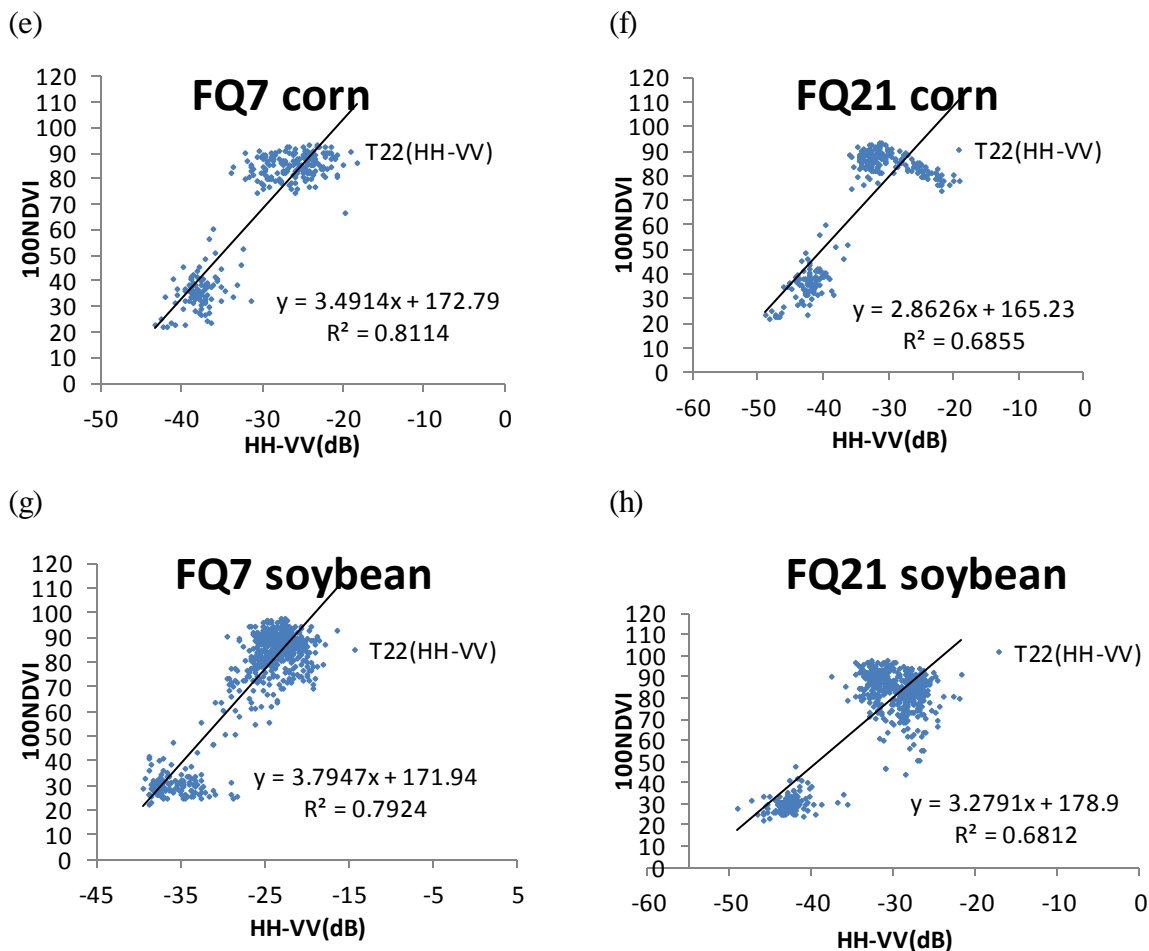
Figure 3.8 Correlation between the HV, HH-VV from the RADARSAT-2 FQ7 and FQ21 and NDVI for corn and soybeans

3.4.3.2   Decomposition Polarimetric Parameters

(1) Freeman-Durden and Pedestal Height

The volume scattering of Freeman-Durden decomposition parameters was significantly correlated with NDVI for both soybeans and corn. In addition, pedestal height was highly correlated with NDVI for both crops. Pedestal height describes the degree of polarization of a scattered wave. Studies demonstrate that pedestal height is directly proportional to vegetation density (Evans, et al. 1988). In this study, the pedestal height is also positively correlated with the NDVI of soybeans and corn. Also, the saturation of Pedestal height to

NDVI was observed when the NDVI of crop samples was higher than 0.75, particularly in the FQ21 images.

	R(FQ7, NDVI)		R(FQ21,NDVI)	
	Soybean	Corn	Soybean	Corn
Freeman-Durden decomposition parameters				
Single	-0.41	-0.37	-0.34	-0.44
Double	-0.40	-0.42	0.31	0.41
Volume	0.93	0.92	0.89	0.93
Cloude-Pottier decomposition parameters				
Entropy	0.83	0.82	0.76	0.82
Alpha (deg.)	0.82	0.82	0.69	0.79
Anisotropy	-0.35	-0.14	-0.46	-0.23
Polarimetric variables				
PH	0.90	0.91	0.87	0.89
Total power	0.58	0.62	0.85	0.84

Table 3.5 The correlation between soybeans and corn crop NDVI to polarimetric decomposition parameters in FQ7 and FQ21

(2) Entropy

A slightly weak correlation was reported between Entropy and crop NDVI. Entropy characterizes the randomness of scattering occurring within a target. The randomness increases as crops develop, due to scattering from the soil, the vegetation, as well as the soil-vegetation interaction all contribute to the total scattering of radar signals. As Table 3.5 shows, the correlation between Entropy and NDVI is slightly higher in soybeans fields than that in corn fields. It might be interpreted from the figure that the Entropy is more sensitive to the low biomass crops, such as soybeans, than crops with high biomass.

(3) Overall

In summary, the sensitivity of NDVI to polarimetric parameters varied from parameter to parameter. The correlation between the same parameter to the crop NDVI also depends on the crop types and incidence angles at which imagery is obtained. In general, parameters that are indicative of volume and multi-scattering, such as HV, HH-VV, and volume scattering from Freeman-Durden decomposition, are relatively highly related to the value of NDVI. Also, parameters related to the density and randomness of plants, like the Pedestal height and Entropy in the Cloude-Pottier decomposition, are correlated with the NDVI. However, due to the lack of high quality optical images obtained in mid-June, the NDVI values of most samples were clustered either in the high or the low value zones. The statistical results might be more convincing if NDVI maps from various dates were available.

(a)

FQ7 corn

$y = 7E\text{-}06x^2 + 0.0039x + 0.2437$

$R^2 = 0.6678$

Entropy

100NDVI

Entropy

(b)

FQ21 corn

$y = -5E\text{-}05x^2 + 0.0098x + 0.2894$

$R^2 = 0.6956$

Entropy

100NDVI
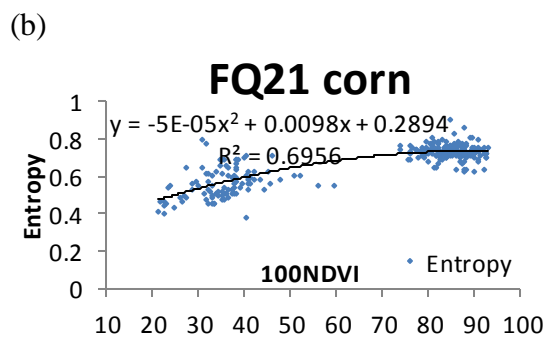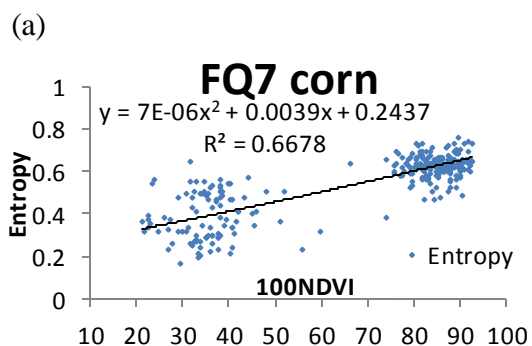
Entropy

(c)

(d)
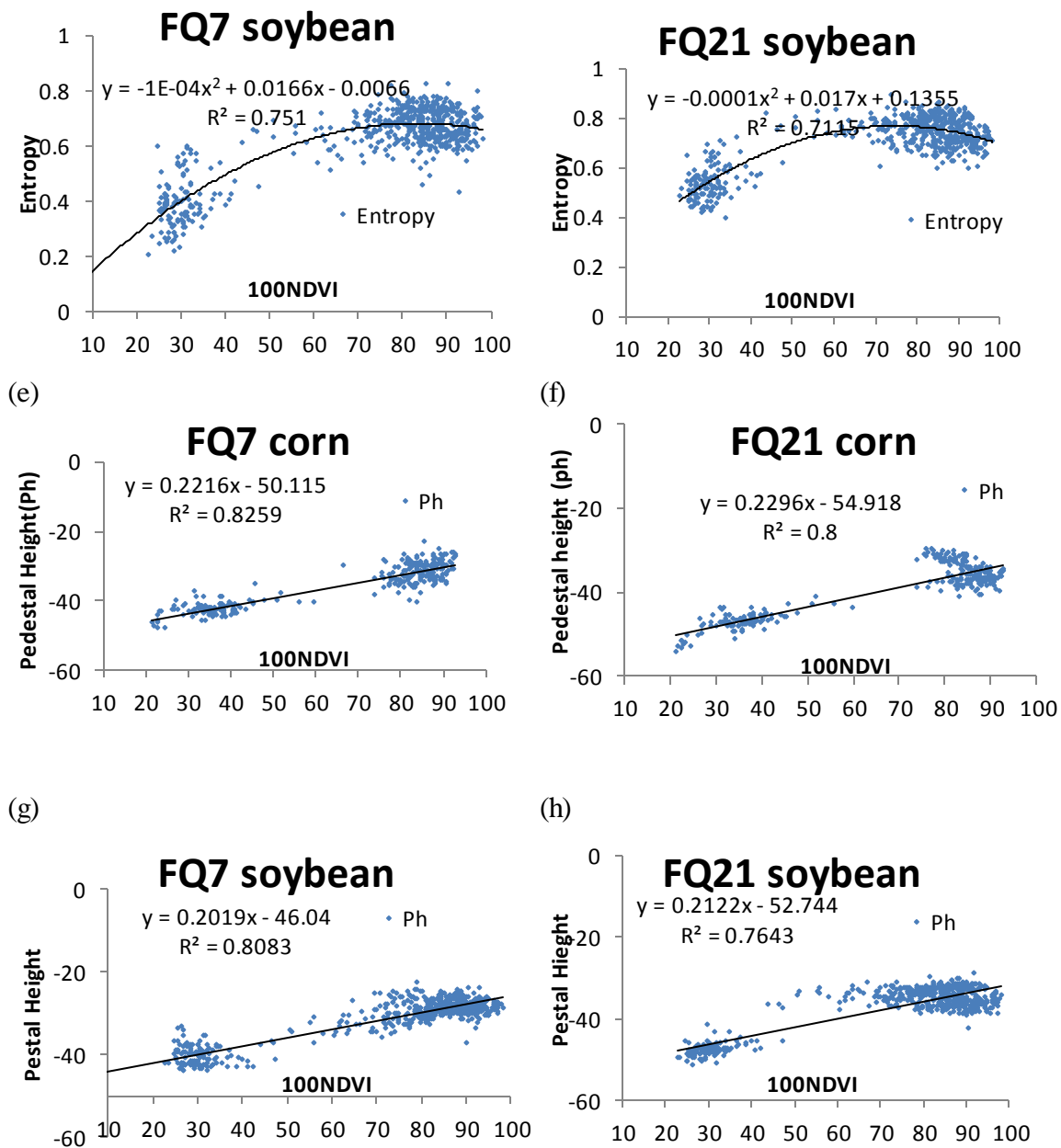
Figure 3.9 Scatter plots between the Entropy, Pedestal and NDVI for corn and soybeans at FQ7 (a, c, e, g), and FQ21 (b, d, f, h) image.

3.4.3.3 Comparison of all Polarimetric Parameters

By comparing the correlation between NDVI and polarimetric parameters, the rankings of the coefficients for soybeans and corn are shown and analyzed below.

(1) Soybeans

For soybeans, the volume scattering derived from HV intensity and Freeman-Durden decomposition parameters are significantly correlated to the value of NDVI, with a Pearson's r of 0.93. The Pedestal height and HH/VV are also very sensitive to the NDVI values of soybeans with the same Pearson's r of 0.9. The correlation between T22 (|HH-VV|) and NDVI is in the third place, with a Pearson's r o f 0.89.

As discussed in the above sections, serious saturations were observed while using FQ21 images, due to reduced canopy penetration of canopy. Parameters derived from FQ7 images, obtained at a steeper incidence angle, have higher correlation to NDVI than those from FQ21.

Table 3.6 the ranking of correlation coefficients between polarimetric parameters and NDVI for soybeans

Ranking	Recommended parameters	Optimal Mode	r
1	C22 (HV)	FQ7	0.93
1	Freeman(Vol)	FQ7	0.93
2	PH	FQ7	0.9
2	HH/VV	FQ7	-0.9
3	T22(HH-VV)	FQ7	0.89

(2) Corns

The volume scatterings from HV intensity and Freeman-Durden decomposition are strongest correlated to corn NDVI among all the parameters, with the Pearson's r as high as 0.93. Pedestal height and T22 are also very sensitive to NDVI values.

The preverable mode for volume scatterings is FQ21, and that for Ph and T22 is FQ7. However, the difference between FQ7 and FQ21 is not significant, which is less than 0.02. Therefore, no absolute optimal angle mode for obtaining imagery was found in this study.

Table 3.7 The ranking of correlation coefficients between polarimetric parameters and NDVI for corn.

Ranking	Recommended parameters	Better Mode	r
1	C22(HV)	FQ21	0.93
1	Freeman(Vol)	FQ21	0.93
2	PH	FQ7	0.91
3	T22(HH-VV)	FQ7	0.9

3.5   Conclusion

This study investigates the sensitivity of RADARSAT-2 polarimetric SAR signals to structural changes of wheat, field peas, soybeans, and corn during the 2012 growing season, Southwestern Ontario. Several conclusions have been drawn from this study:

(1) Polarimetric SAR data are able to provide complement information for optical data in time critical agricultural applications, such as crop condition monitoring, when high quality optical data are not available under unfavorable weather conditions.

(2) The potential of polarimetric SAR parameters in characterizing the temporal changes of field peas and corn height have been amply demonstrated in this study. The high correlation coefficients of 0.82 and 0.79 were observed in peas and corn. The recommended parameters for field pea height estimation are Freeman-Durden volume scattering and HV/VV. Corn height estimation is best performed with Entropy and Alpha parameters.

(3) Strong correlation coefficients have been observed between polarimetric parameters and NDVI values for both corn and soybeans. The highest correlation coefficient is 0.93, between HV, Freeman-Durden Volume and NDVI for both corn and soybean crops. Pedestal height is also sensitive to crop NDVI; the correlation coefficients are 0.9 and 0.91 for soybeans and corn, respectively.

(4) Marginal differences were observed between the images taken at FQ21 and FQ7 incidence angles. FQ7 is slightly better than FQ21 in estimation of soybean NDVI from some polarimetric SAR parameters, such as HH-VV, HH/VV, Pedestal Height, and volume scattering.

The potential of deriving NDVI from RADARSAT-2 polarimetric SAR data has been demonstrated in this study. Further research should focus on investigating the relationship between the SAR parameters and other plant parameters, such as LAI and biomass, so as to facilitate crop yield estimation applications.

3.6   References

Baghdadi, N., et al. (2009). "Potential of SAR sensors TerraSAR-X, ASAR/ENVISAT and PALSAR/ALOS for monitoring sugarcane crops on Reunion Island." Remote Sensing of Environment, Vol.113, pp.1724-1738.

Chakraborty , M., M ANJUNATH , K.R., P ANIGRAHY , S., K UNDU , N. and P ARIHAR , J.S. (2005),Rice crop parameter retrieval using multi-temporal, multi-incidence angle Radarsat SAR data. ISPRS Journal of Photogrammetry and Remote Sensing, 59, pp. 310–322.

Cloude, S. R. and E. Pottier (1996). "A review of target decomposition theorems in radar polarimetry." Geoscience and Remote Sensing, IEEE Transactions on 34(2): 498-518.

Cloude, S. R. and Pottier, E., 1997. An entropy based classification scheme for land applications of polarimetric SAR. IEEE Transactions on Geoscience and Remote Sensing, 35(1).

Eitel , J.U.H., Long , D.S., Gessler , P.E. and Smith , A.M.S., (2007), Using in-situ measurements to evaluate the new RapidEye satellite series for prediction of wheat nitrogen status. International Journal of Remote Sensing, 28, pp. 4183–4190.

Eitel , J.U.H., Long , D.S., Gessler , P.E. and Hunt , E.R., (2008), Combined spectral index to improve ground-based estimates of nitrogen status in dryland wheat. Agronomy Journal, 100, pp. 1694–1702.

Ferrazzoli, P., S. Paloscia (1997). "The potential of multifrequency polarimetric SAR in assessing agricultural and arboreous biomass." Geoscience and Remote Sensing, IEEE Transactions on 35(1): 5-17.

Freeman, A. and Durden, S. L., 1998. A three-component scattering model for polarimetric SAR data. IEEE Transactions on Geoscience and Remote Sensing, 36(3), pp. 963-973.

Gerighausen, H., et al. (2007), DEMMIN—A test site for the validation of remote sensing data products: General description and application during AgriSAR 2006, in Proceedings of the AGRISAR and EAGLE Campaigns Final Workshop,Eur. Space Res. and Technol. Cent., Noorwijk, Netherlands.

Haboudane, D., Miller , J.R., Tremblay , N., Zarco-Tejada, P.J. and Dextraze , L., (2002), Integrated narrow-band vegetation indices for prediction of crop chlorophyll content for application to precision agriculture. Remote Sensing of Environment, 81, pp. 416–426.

Jiao, X., et al. The sensitivity of RADARSAT-2 polarimetric SAR data to corn and soybean leaf area index (2011). Canadian Journal of Remote Sensing, Vol. 37, pp. 69-81.

Lee, J.S., and Pottier, E. 2009. Polarimetric radar imaging: from basics to applications. Taylor & Francis Group, New York.

Li , Y., Liao , Q., Li , X., Liao , S., Chi , G. and Peng , S. (2003). Towards an operational system for regional-scale rice yield estimation using a time-series of Radarsat ScanSAR images. International Journal of Remote Sensing, 24, pp. 4207–4220.

Lievens, H., Verhoest, N., De Keyser, E., Vernieuwe, H., Matgen, P., Alvarez-Mozos, J., & De Baets, B. (2011). Effective roughness modelling as a tool for soil moisture retrieval from C-and L-band SAR. Hydrology and Earth System Sciences, 15(1), 151-162.

Liu, J., E. Pattey, et al. (2012). Assessment of vegetation indices for regional crop green LAI estimation from Landsat images over multiple growing seasons. Remote Sensing of Environment 123(0): 347-358.

Longtin, K., (2006). An overview of the Canadian food system. Research and Analysis Directorate, Strategic Policy Branch, Agriculture and Agri-Food Canada, Ottawa, Ontario, 120 pp.

Lopez‐Sanchez, J. M., & Ballester‐Berman, J. D. (2009). Potentials of polarimetric SAR interferometry for agriculture monitoring. Radio Science, 44(2).

McNairn, H., and Brisco, B. (2004), The application of C-band polarimetric SAR for agriculture: A review, Can. J. Remote Sensing, 30(3).

McNairn, H., Champagne, C., Shang, J., Holmstrom, D.A., and Reichert, G(2009a). Integration of optical and Synthetic Aperture Radar (SAR) imagery for delivering operational annual crop inventories. ISPRS Journal of Photogrammetry and Remote Sensing, 64, pp. 434–449.

McNairn, H., J. van der Sanden, R. Brown, and J. Ellis (2000) The potential of RADARSAT-2 for crop mapping and assessing crop condition, in Proceedings of the 2nd International Conference on Geospatial Information in Agriculture and Forestry, vol. 2, pp. 81 – 88, Veridian ERIM Int. Conf.,Ann Arbor, Mich.

McNairn, H., Shang, J., Jiao, X., et Champagne, C. (2009b). The Contribution of ALOS PALSAR Multi-polarization and Polarimetric Data to Crop Classification. IEEE Transactions on Geoscience and Remote Sensing, 47(12, Article No. 5233805), p. 3981-3992.

Paloscia,S. (1998). "An empirical approach to estimating leaf area index from multifrequency SAR data." International Journal of Remote Sensing 19(2): 359-364.

Rouse, J. W., Haas, R. H., Jr., Schell, J. A., & Deering, D. W. (1974). Monitoring vegetation systems in the Great Plains with ERTS. Third ERTS-1 Symposium (pp. 309–317). Washington, DC: NASA.

Shang, J., McNairn, H., Champagne, C., and Jiao, X. (2009). «Contribution of multi-frequency, multi-sensor, and multi-temporal radar data to operational annual crop mapping. », IEEE Geoscience and Remote Sensing Letters, 3(1), p. III378-III381. doi : 10.1109/IGARSS.2008.4779362

Shao , Yun, Fan , X., Liu , H., Xiao , J., Ross , S., Brisco , B., B Rrown , R. and S Taples , G. (2001) Rice monitoring and production estimation using multitemporal RADARSAT. Remote Sensing of Environment, 76, pp. 310–325.

Steffen Gebhardt , Juliane Huth , Lam Dao Nguyen , Achim Roth and Claudia Kuenzer (2012): A comparison of TerraSAR-X Quadpol backscattering with RapidEye multispectral vegetation indices over rice fields in the Mekong Delta, Vietnam, International Journal of Remote Sensing, 33:24, 7644-7661.

Viña, A., Gitelson, A. A., Nguy-Robertson, A. L., & Peng, Y. (2011). Comparison of different vegetation indices for the remote assessment of green leaf area index of crops. Remote Sensing of Environment, 115(12), 3468-3478.

Wilcox, R. R. (2012). Introduction to robust estimation and hypothesis testing. Academic Press.

Chapter 4

4   Conclusions

4.1   Summary

The successful management of land use/land cover (LU/LC) planning and agricultural applications depends on continuous monitoring of LU/LC changes and crop growing conditions. Timely information about land surface is critical in the urban rural fringe areas in Southwestern Ontario, Canada, where rapid urban expansion has great influence on the agricultural production and the resultant economy. Frequent monitoring permits complete and accurate assessments of the impacts of urban development on the local and regional agriculture. Remote Sensing provides an efficient and effective tool for this purpose.

The commonly available optical remote sensing data are not reliable for crop type identification and conditions monitoring during the growing seasons due to frequent overcast and rainy weather. SAR images provide an alternative data source to optical images. In addition, the newly available polarimetric SAR data contain full polarization information, and have greater potential compared with the traditional single polarization SAR data for the applications in LU/LC mapping and crop monitoring.

Chapter 2 presented a classification procedure for the LU/LC mapping of urban/rural fringe areas using multi-temporal polarimetric RADARSAT-2 images. Nine classes were identified with a high overall accuracy over 90%. The classification results were compared and analyzed from four aspects: decomposition parameters, classifiers, multi-date image combinations, and post-classification processing methods.

Chapter 3 described the sensitivities of RADARSAT-2 polarimetric parameters to vegetation parameters over the crop growing season from two aspects: (1) the responses of polarimetric parameters to the change of crop heights in different phenological stages. And (2) the relationship between polarimetric parameters and NDVI values for selected crops.

4.2   Conclusions and Results

The research presented in this thesis provided response to the questions posed in the introduction:

1. How accurately can LU/LC be classified in this urban/rural fringe areas from the fine beam multi-temporal RADARSAT-2 satellite images?

   An accurate LU/LC map of the urban and rural fringe area of the City of London, Ontario has been generated with a high accuracy of 91.0% (OA) at 0.888 (Kappa). The results are satisfactory considering the complex natural of the boundary areas and various kinds of crop types in this area.

2. What is a good classification procedure for LU/LC classification in urban/rural fringe areas using RADARSAT-2 satellite images?

   The classification procedure using the log transformed Pauli decomposition parameters and Gaussian distribution MLC yielded better classification results than other parameters or the Wishart based MLC methods.

3. What is a suitable multi-date combination of polarimetric RADARSAT-2 images in LU/LC classification?

   The classification accuracy can be significantly improved through carefully selecting and combining multi-date images. An overall accuracy of 91% was achieved by using five-date images combinations. Satisfactory classification accuracy (over 87%) can also be achieved using images from three date data, as long as these combinations included images obtained at key points in plant development during the season. The images retrieved in the early and middle portion of the growing seasons provided better classification results than those from other parts of the growing season.

4. What is the potential of polarimetric RADARSAT-2 for monitoring crop height changes?

The temporal and spatial variation of crop height over the season of crop growing was well characterized by the polarimetric SAR parameters. The curves of entropy, HH-VV, and Anisotropy, as well as HV/VV were shown to be closest to the temporal profile of height in corn, soybeans, wheat, and field pea crops respectively.

5. How sensitive are RADARSAT-2 polarimetric parameters to crop biophysical parameters, such as NDVI?

Strong correlations were observed between the NDVI values and HV, volume scattering in Freeman-Durden decomposition, and Pedestal height for both soybeans and corn crops. Insignificant differences were observed between the images taken at FQ21 and FQ7 incidence angles. However, polarimetric SAR parameters, such as HH-VV, HH/VV, and pedestal height, in FQ7 were slightly more sensitive to plant parameters than those in FQ21.

4.3   Research Contributions

4.3.1 Technical Contribution

Chapter 2 demonstrated the capabilities of Gaussian based Maximum Likelihood Classifier (MLC) in polarimetric SAR image classification. The classification results indicated that Gaussian distribution was an effective method of characterizing distribution of log transformed Pauli decomposition parameters.

4.3.2 Practical Contribution

The main contributions of the study in Chapter 2 are demonstrated in two aspects:

(1) An operational procedure has been provided for LU/LC classification in the urban/rural fringe areas using polarimetric RADARSAT-2 data. Using this procedure, detailed LU/LC classes, including crop types and urban land use classes, can be classified with a high degree of accuracy.

(2) An accurate and economic combination strategy of multi-date data for LU/LC classification has been recommended. This strategy can be used for detailed crop inventory in Southwestern Ontario, particularly in the urban/rural fringe areas.

The main contribution in Chapter 3 is that it explored the potential of polarimetric RADARSAT-2 data for crop condition monitoring in Southwestern Ontario, Canada.

(1) Some polarimetric parameters are shown to be responsive to the variation of crop plants in Southwestern Ontario, and thus might be used for vegetation change monitoring.

(2) High correlation between RADARSAT-2 polarimetric parameters and NDVI of corn and soybean crops in Southwestern Ontario have been demonstrated. Several polarimetric parameters with high correlation coefficients were recommended for NDVI estimation.

4.4   Possible Future Research

 (1) Texture Analysis and Object Classification

The advantages of an object-based method are not obvious when merely applied in post-classification processing. Further research would be worthwhile in terms of studying the benefits of applying object-based methods to multi-temporal polarimetric RADARSAT-2 data classification. Additionally, texture information that can be retrieved from SAR images, such as gray-level co-occurrence matrices (GLCM), within each object might be useful in improving classification accuracy. Future research could focus on using texture features extracted from the polarimetric SAR data in an object-based classification.

(2) Correlation Analysis with Other Agricultural Parameters

Crop height and NDVI are two of the important parameters that describe crop growing conditions. However, in order to both accurately estimate the biomass of crops and give early prediction of crop yields, more information is necessary. The correlation between the polarimetric SAR parameters and other crop biophysical parameters, such as Leaf Area Index, enhanced vegetation index, and soil moisture, deserve more study.

Appendices

A. Polarimetric Decomposition Theorem and Results

A1 H/Alpha/A Decomposition and Pedestal Height

H/Alpha/A Decomposition method was proposed by Cloude and Pottier in 1997. This method is based on an eigenvector analysis of 3X3 coherency T3 matrix.

The Entropy (H) indicates the randomness of scattering surface. It is given by Eq.(A1)

$$H = \sum_{i=1}^{3} -P_i log_3 P_i \quad Where \quad P_i = \frac{\lambda_i}{\sum_{j=1}^{3} \lambda_j}$$

λ_i is the coherency metrix eigenvalues. $\hspace{4cm}$ (A1)

The alpha angle identified scattering types. It is defined by Eq. (A2)

$$\vec{e_i} = \exp(i\phi_i) \begin{bmatrix} \cos\alpha_i \\ \sin\alpha_i \cos\beta_i \exp(i\delta_i) \\ \sin\alpha_i \sin\beta_i \exp(i\gamma_i) \end{bmatrix}$$

where $\vec{e_i}$ is the coherency matrix eigenvalues.

δ is the phase difference between $S_{HH} + S_{VV}$ and $S_{HH} - S_{VV}$.

γ is the phase difference between $S_{HH} + S_{VV}$ and S_{HV}.

ϕ is the decomposition phase $S_{HH} + S_{VV}$.

The mean alpha angle is defined by: $\bar{\alpha} = P_1\alpha_1 + P_2\alpha_2 + P_3\alpha_3$.

The α_i is the alpha angle corresponding to the $\vec{e_i}$ eigenvector. $\hspace{2cm}$ (A2)

The anisotropy is defined by Eq. (A3)

$$A = \frac{\lambda_2 - \lambda_3}{\lambda_2 + \lambda_3} \; ; \lambda_i \; is \; the \; coherency \; metrix \; eigenvalues, \lambda_1 > \lambda_2 > \lambda_3 \hspace{1cm} (A3)$$

The Pedestal Height is defined by Eq. (A4)

$$PH = \frac{\lambda_3}{\lambda_1} \qquad\qquad (A4)$$

A 2 Freeman Decomposition

The Freeman-Durden decomposition is a method for converting the polarimetric SAR observations into a physically based, three-component scattering model, without any ground truth measurements (Freeman & Durden, 1998). The scattering model is composed of surface, double- or even- bounce and volume scatter.

$$R_H = \frac{cos\theta - \sqrt{\varepsilon_r - sin^2\theta}}{cos\theta + \sqrt{\varepsilon_r - sin^2\theta}} \; , \qquad R_V = \frac{(\varepsilon_r - 1)\{sin^2\theta - \varepsilon_r(1 + sin^2\theta)\}}{(\varepsilon_r cos\theta + \sqrt{\varepsilon_r - sin^2\theta}\;)^2},$$

$$S = \begin{bmatrix} R_H & 0 \\ 0 & R_V \end{bmatrix}, \quad F_S = |R_V|^2,$$

$$S = \begin{bmatrix} e^{2j\gamma_H} R_{TH}R_{GH} & 0 \\ 0 & e^{2j\gamma_V} R_{TV}R_{GV} \end{bmatrix}, \qquad F_D = |R_{TV}R_{GV}|^2 \; , \quad F_V = \frac{3}{2}\langle R_{VH} R_{HV}{}^* \rangle.$$

where θ is the local incidence angle, ε_r is the relative dielectric constant of the surface

. $R_{TV}R_{TH}$ are the reflection coefficients from vertical trunk surface for vertical and

horizontal polarizations, respectively. $R_{GV}R_{GH}$ arethe reflection coefficients from

Fresnel reflection coefficients for vertical and horizontal polarizations, respectively.

γ_V and γ_H represent any propagation attenuation and phase change effects in vertical

and horizontal polarizations, respectively.

B. Reference Data and Samples

The reference data used in this study including air photo imagery, RapidEye optical imagery, as well as pictures and height measurements taken in the field.

B1 Optical Images
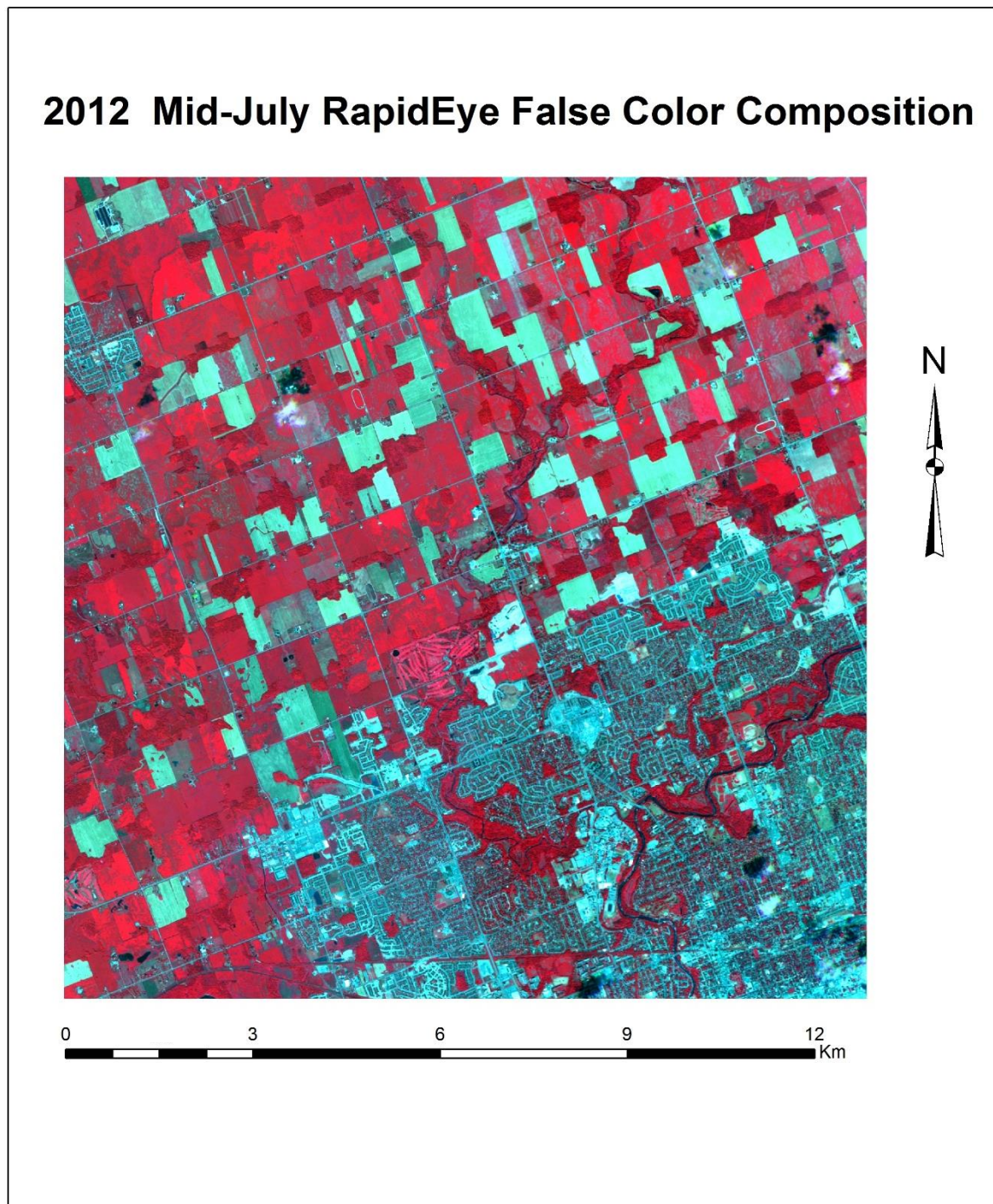
Figure B.1 The RapidEye image by false color composition taken in July, 2012

Figure B.2 Air photo of London, Ontario taken in 2009

B2 Training Samples and Testing Samples
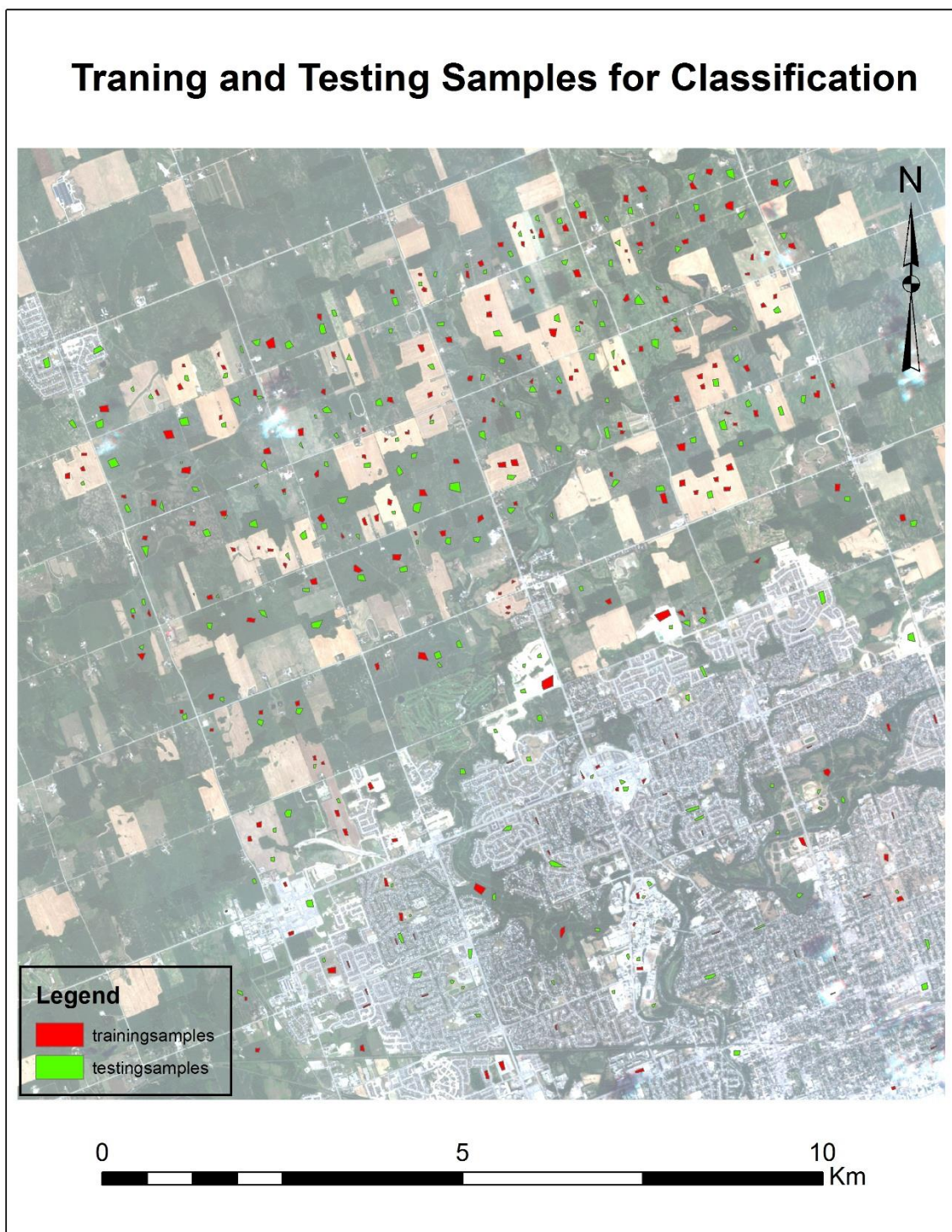
Figure B.3 Training and testing samples shown in RapidEye image fro reference
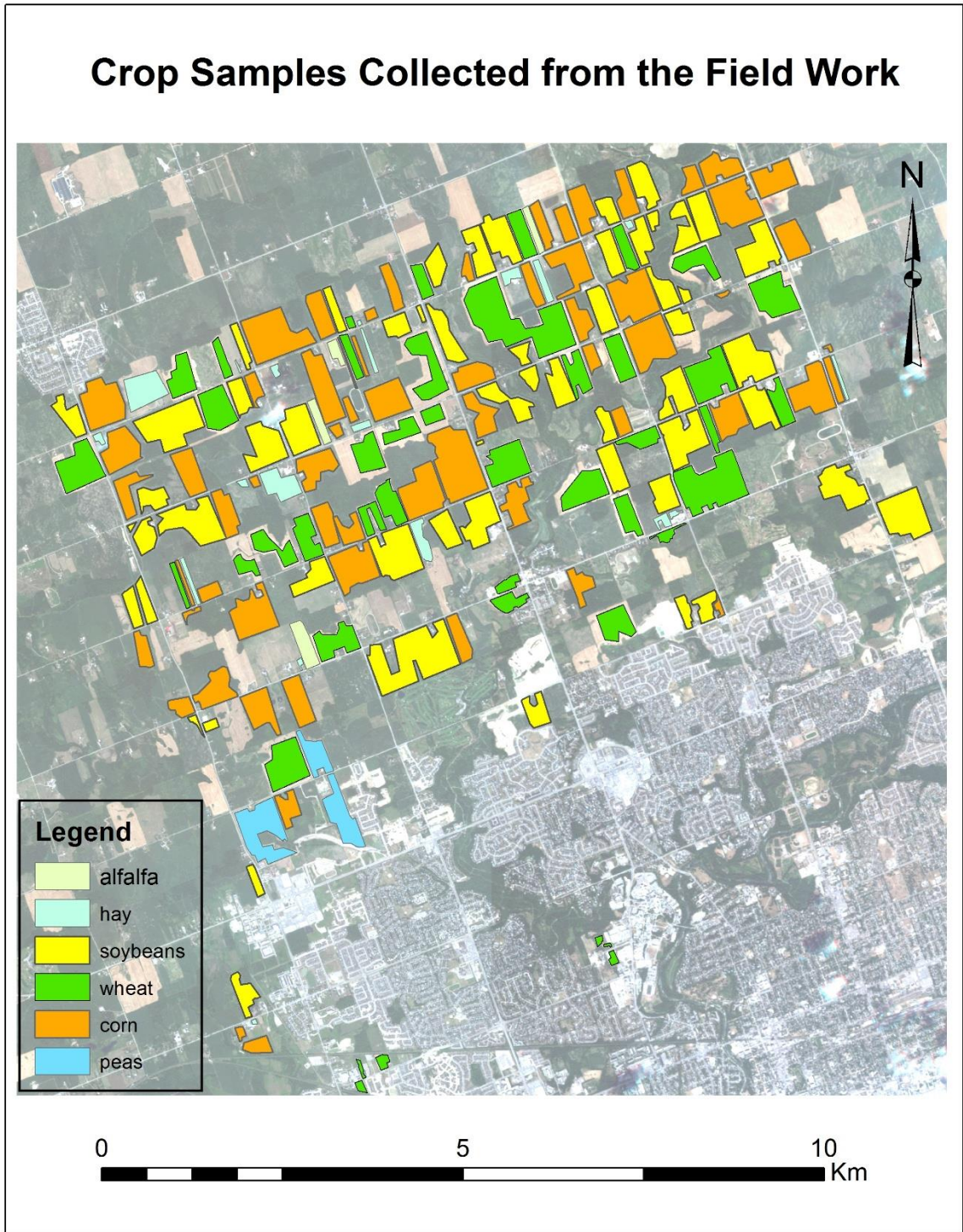
Figure B.4 Crop samples collected from the fields shown in a RapidEye image

B3 LU/LC Classes and Field Work Pictures

Figure B.6 LU/LC classes photographs, (a) commercial area, (b) construction site, (c) industrial areas
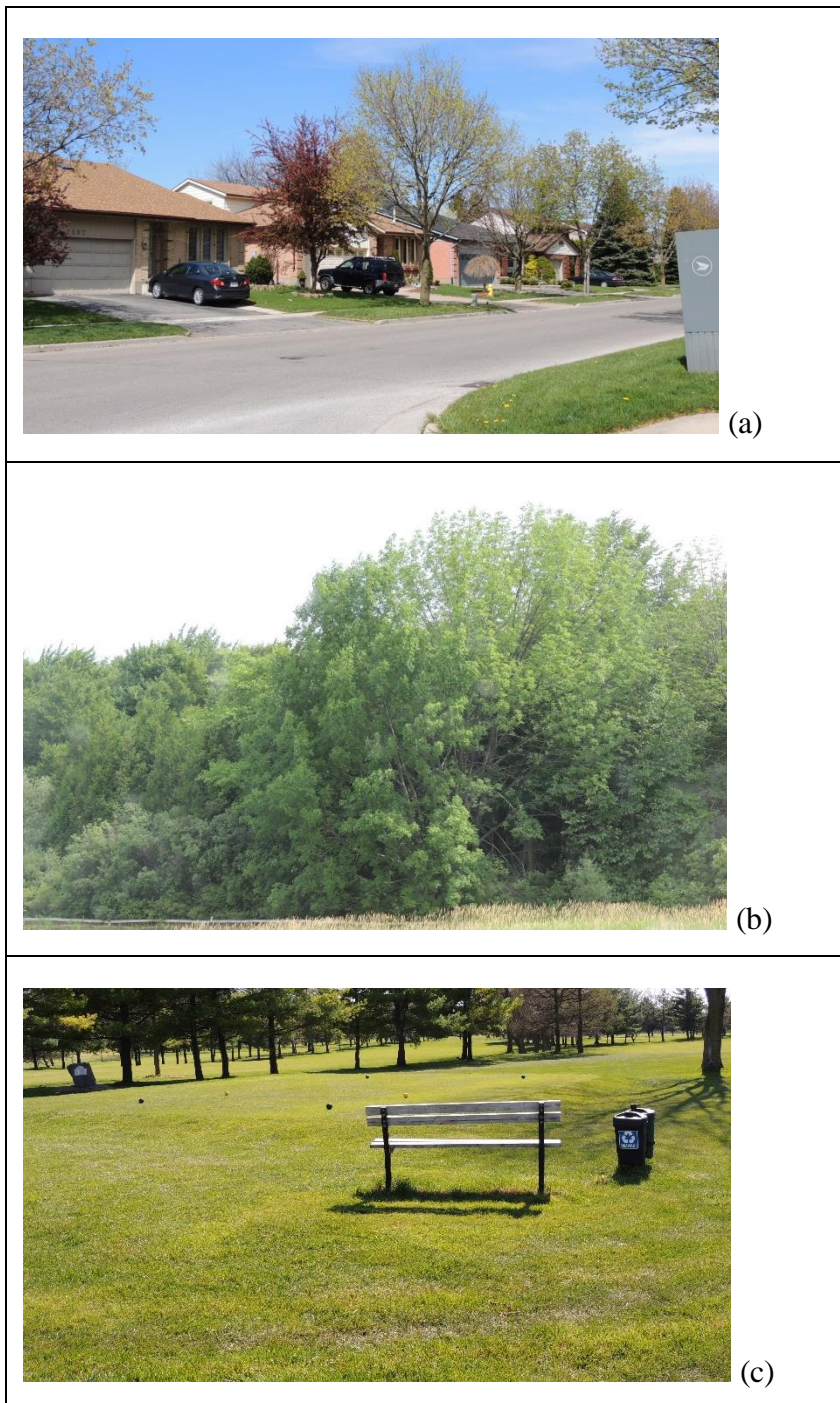
Figure B7 LU/LC classes photographs, (a) residential area, (b) forest, (c) lawn

B 4 Crop Height Measurements

Table B.1 Height measurement fieldwork data. (Cut: Harvested crop, Gr: Grass and forage H: Height (cm), NSb: new soybeans, Sb: Soybeans, Soil: bare soil, Wt: Wheat)

field name		May 4-May 7	May 28-May 31	June 21-June 24	July 16-July 18	Aug.8-Aug.11	Sep.2-Sep.5	Sep.25-Sep.28
1	Type	Wt	Wt	Wt	Wt Cut	Wt Cut	Wt Cut	Wt Cut
	H	30	75	70		<30		<20
2	Type	Wt	Wt	Wt	Wt Cut	Wt Cut		Wt Cut
	H	30	75	70		<30		<20
3	Type			Sb	Sb	Sb	Sb	Sb
	H			20	39	55	70	65
4	Type		Sb	Sb	Sb	Sb	Sb	Sb
	H			20	37	70	80	65-75
5	Type	Soil	corn	corn	corn	corn	corn	corn
	H		20	76	180	190	230	215
6	Type	Soil	corn	corn	corn	corn	corn	corn
	H		20	80-120	210	200	230	232
7	Type	Soil	Sb	Sb	Sb	Sb	Sb	Sb
	H			25	43	63	70	60
8	Type	Soil	corn	corn	corn	corn	corn	corn
	H		35	80-120	210	215	230	Cut

9	Type			Wt Cut	Gr	Gr	Gr	Gr
	H			<15	35	<15	50	
10	Type	Cut corn		Sb	Sb	Sb	Sb	Sb
	H			20-25	40	65	50	50
11	Type	Wt	Wt	Wt	Wt Cut	NSb	NSb	N Sb
	H	25	70	50-60	<10	<15	33	45
12	Type	Cut corn		Sb	Sb	Sb	Sb& Gr	Sb& Gr
	H			33-40	50	60	70	Cut
13	Type	Wt	Wt	Wt	Wt Cut			
	H	28	53	70				
14	Type		Wt			NSb	NSb	NSb
	H		55				43	55
15	Type		corn	corn	corn	corn	corn	corn
	H		30	100	225	235	250	175
16	Type	Gr	Gr	Gr cut	Gr	Gr	Gr	Gr
	H		60	<15			<15	25
17	Type	Soil	corn	corn	corn	corn	corn	corn
	H		25	100-120	210	230	275	220
18	Type	Wt	Wt	Wt	Wt Cut			
	H	30	70	66				
19	Type	Wt	Wt	Wt	Wt Cut			
	H	30	70	69				

20	Type			Sb	Sb	Sb	Sb& G	Sb& G
	H			27	57	60	155	100
21	Type			Sb	Sb	Sb	Sb	Sb Cut
	H			26	45	63	60	
22	Type		Sb	Sb	Sb	Sb	Sb	Sb Cut
	H			30	55	65	65	
23	Type	Soil	Sb	Sb				Sb
	H			30	55	65	65	100
24	Type	Wt	Wt	Wt	Wt Cut			
	H	24	73	90				
25	Type	Soil	corn	corn	corn	corn	corn	corn
	H		25	150	200	220	Cut	Cut
26	Type	Soil	corn	corn	corn	corn	corn	corn
	H		25	120-130	200	220	240	Cut
27	Type			Soil	corn	corn	corn	corn
	H				<15	60	160	Cut
28	Type			Sb	Sb	Sb	Sb	Sb
	H			24	53	57	45	Cut
29	Type	Wt	Wt	Wt	Wt Cut			
	H		72	70				
30	Type	Gr	Gr	Gr	Gr	Gr	Gr	Gr
	H		72	<15	15	35	<10	25

105

31	Type	Wt	Wt	Wt	Wt Cut			
	H	24	60	60				
32	Type	Soil	corn	corn	corn	corn	corn	corn
	H		25	120	190	200	210	210
33	Type	Wt	Wt	Wt	Wt Cut	Wt Cut	Gr	
	H	45	75	77			40	
34	Type	Wt	Wt	Wt	Wt Cut	Wt Cut	Gr	
	H	50	74	74			60	
35	Type	Wt	Wt & Gr	Wt & Gr	Wt Cut	Wt Cut	Gr	
	H	50	90	80			80	
36	Type	Wt	Wt	Wt Cut				
	H	23	50					
37	Type	Wt	Wt	Wt Cut				
	H	33	60					
38	Type	Wt	Wt	Wt	Wt Cut			
	H	31	68	40				
39	Type			Sb	Sb	Sb	Sb	Sb
	H			22	63	75	80	Cut
40	Type	Gr	Gr	Gr	Gr	Gr	Gr	Gr
	H			70	160	160	160	160
41	Type		corn	corn	corn	corn	corn	corn
	H		20	120	210	275	310	300

42	Type		Sb	Sb	Sb	Sb	Sb	Sb
	H			20-22	48	66	67	55
43	Type	peas	peas	peas	NSb	NSb	NSb	NSb
	H	8	45	55	<10	30	63	75
44	Type		corn	corn	corn	corn	corn	corn
	H		20	64				
45	Type	peas	peas	peas	Cut peas		N Pea	Cut Pea
	H	8	35	34			20	
46	Type	peas	peas	peas	Cut peas			
	H	8	35	30				
47	Type			Sb	Sb	Sb	Sb	Sb
	H			20	47	53	50	Cut
48	Type			Sb	Sb	Sb	Sb	Sb
	H			18	47	53	50	Cut
49	Type	Sb		Sb	Sb	Sb	Sb	Sb
	H			30	63	65	63	Cut
50	Type	Sb		Sb	Sb	Sb	Sb	Sb
	H			35	55	60	63	Cut
51	Type			Sb	Sb	Sb	Sb	Sb
	H			25	50	47	Cut	Cut
52	Type			corn	corn	corn	corn	corn
	H			70	190	220	220	230

53	Type			corn	corn	corn	corn	corn
	H			80-100	210	220	250	220

C Classification Results

The comparisons of classification results are compared in four aspects, Gaussian V.S. Wishart distribution, four sets of polarimetric parameters, different time combinations, and three different post-processing methods.

C.1 Gaussian MLC and Wishart MLC

Table C.1 Error matrix for Wishart MLC using May 28, July 15, and September 1 images

Reference Data										
class	Hay	wheat	peas	soybeans	corn	built-ups	CS	forest	lawn	**UA**
Hay	56	0	0	0	0	0	4	7	63	43%
wheat	0	659	0	6	1	0	7	0	0	98%
peas	0	13	61	0	0	11	6	0	1	66%
soybeans	0	0	0	1072	325	1	14	16	3	75%
corn	1	0	0	591	1585	0	9	10	0	72%
built-ups	4	7	0	0	9	1197	8	5	15	96%
CS	0	0	0	0	5	0	106	0	5	91%
forest	0	0	0	0	8	358	1	793	5	68%
lawn	9	0	0	0	1	16	0	0	77	75%

PA	80%	97%	100%	64%	82%	76%	68%	95%	46%	
OA	0.78		KP	0.73						

Table C.2 Error matrix for Gaussian MLC using May 28, July 15, and September 1 images

Reference Data									
class	Hay	wheat	peas	soybeans	corn	built-ups	CS	forest	lawn	**UA**
Hay	43	0	0	0	0	0	0	2	7	83%
wheat	4	732	0	0	5	5	23	0	0	95%
peas	0	0	68	0	0	0	0	0	0	100%
soybeans	8	0	0	1553	396	0	17	27	15	77%
corn	0	0	0	219	1636	0	3	0	0	88%
built-ups	0	0	0	0	2	1479	4	7	3	99%
CS	5	0	0	0	1	0	121	0	0	95%
forest	0	2	0	0	11	226	3	855	6	78%
lawn	13	6	0	0	0	40	0	0	178	75%
PA	83%	95%	100%	77%	88%	99%	95%	78%	78%	
OA	0.86		**KA**	0.83						

C.2 PolSAR Parameters

Table C. 1 Error matrix for Gaussian MLC using all T3 elements from May 4, May 28, June 21, and July 15 images

class	Hay	wheat	peas	soybeans	corn	built-ups	CS	forest	lawn	UA
Reference Data										
Hay	4	23	0	0	0	0	0	0	1	14%
wheat	47	1368	0	0	2	15	7	4	5	94%
peas	1	25	85	0	7	0	0	0	0	72%
soybeans	9	12	2	1328	272	49	4	246	10	69%
corn	19	2	0	180	2013	15	0	4	0	90%
built-ups	0	0	0	10	0	1321	5	22	26	95%
CS	3	0	0	0	0	14	97	0	6	81%
forest	21	9	0	71	4	79	0	949	34	81%
lawn	8	4	0	0	0	45	4	0	256	81%
PA	4%	95%	98%	84%	88%	86%	83%	77%	76%	
OA	0.85		**KP**	0.81						

504_528_621_715 T3all MLC LU/LC Map

Legend:
- alfalfa
- wheat
- hay
- peas
- soybeans
- corn
- residential
- construction site
- high_building
- lawn
- forest

Scale: 0 — 3 — 6 — 9 — 12 Km

N
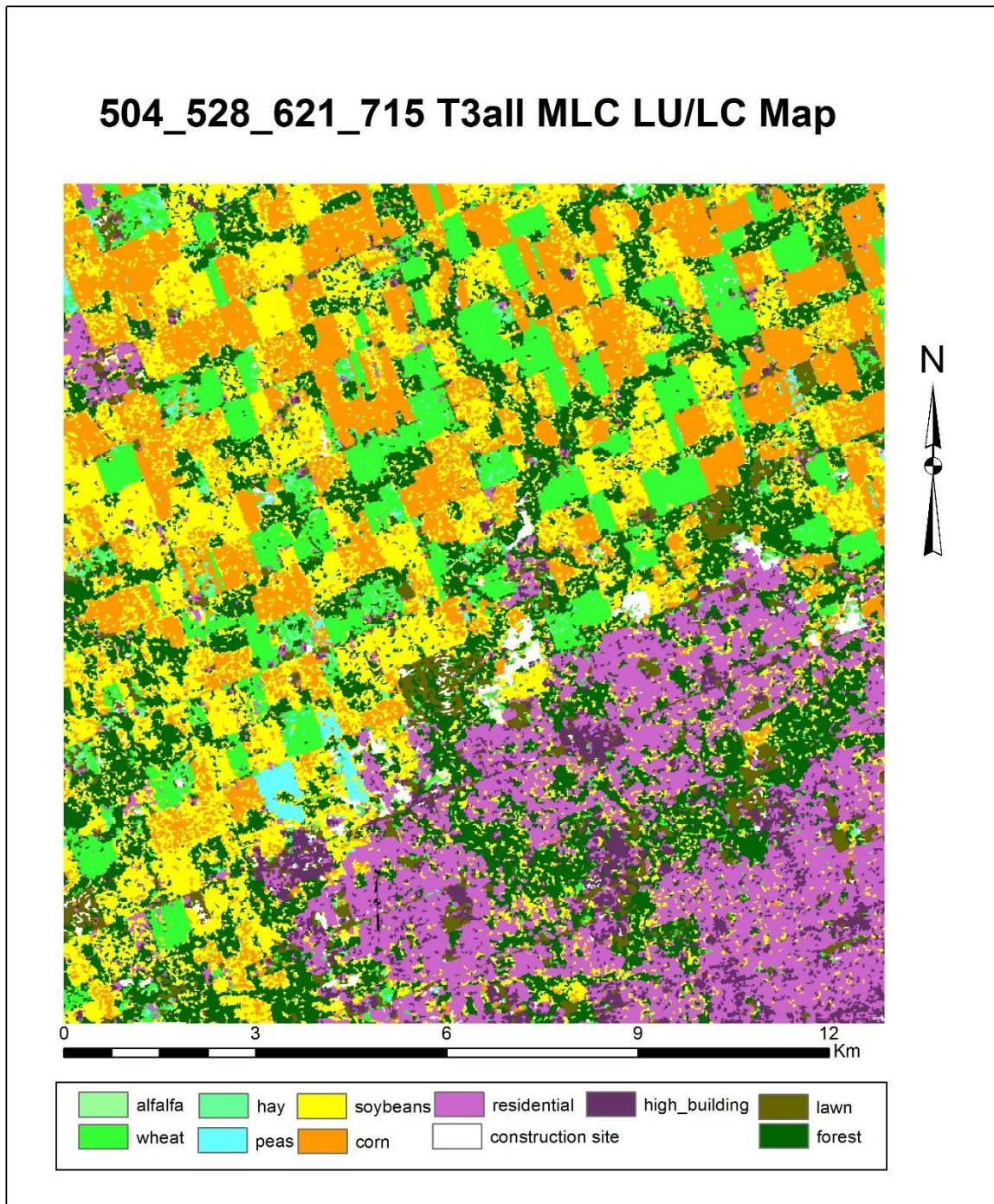
Figure C.1 classification map for Gaussian MLC using all T3 elements from May 4, May 28, June 21, and July 15 images

Table C.4 Error matrix for Gaussian MLC using Pauli3 elements from May 4, May 28, June 21, and July 15 images

class	Hay	wheat	peas	soybeans	corn	built-ups	CS	forest	lawn	UA
Reference Data										
Hay	4	23	0	0	0	0	0	0	1	66%
wheat	47	1368	0	0	2	15	7	4	5	97%
peas	1	25	85	0	7	0	0	0	0	100%
soybeans	9	12	2	1328	272	49	4	246	10	78%
corn	19	2	0	180	2013	15	0	4	0	94%
built-ups	0	0	0	10	0	1321	5	22	26	92%
CS	3	0	0	0	0	14	97	0	6	90%
forest	21	9	0	71	4	79	0	949	34	85%
lawn	8	4	0	0	0	45	4	0	256	80%
PA	19%	99%	100%	94%	85%	88%	70%	92%	74%	
OA	0.89		**KP**	0.87						

504_528_621_715 Pauli3 MLC LU/LC Map

Legend:
- alfalfa
- hay
- soybeans
- residential
- high_building
- lawn
- wheat
- peas
- corn
- construction site
- forest
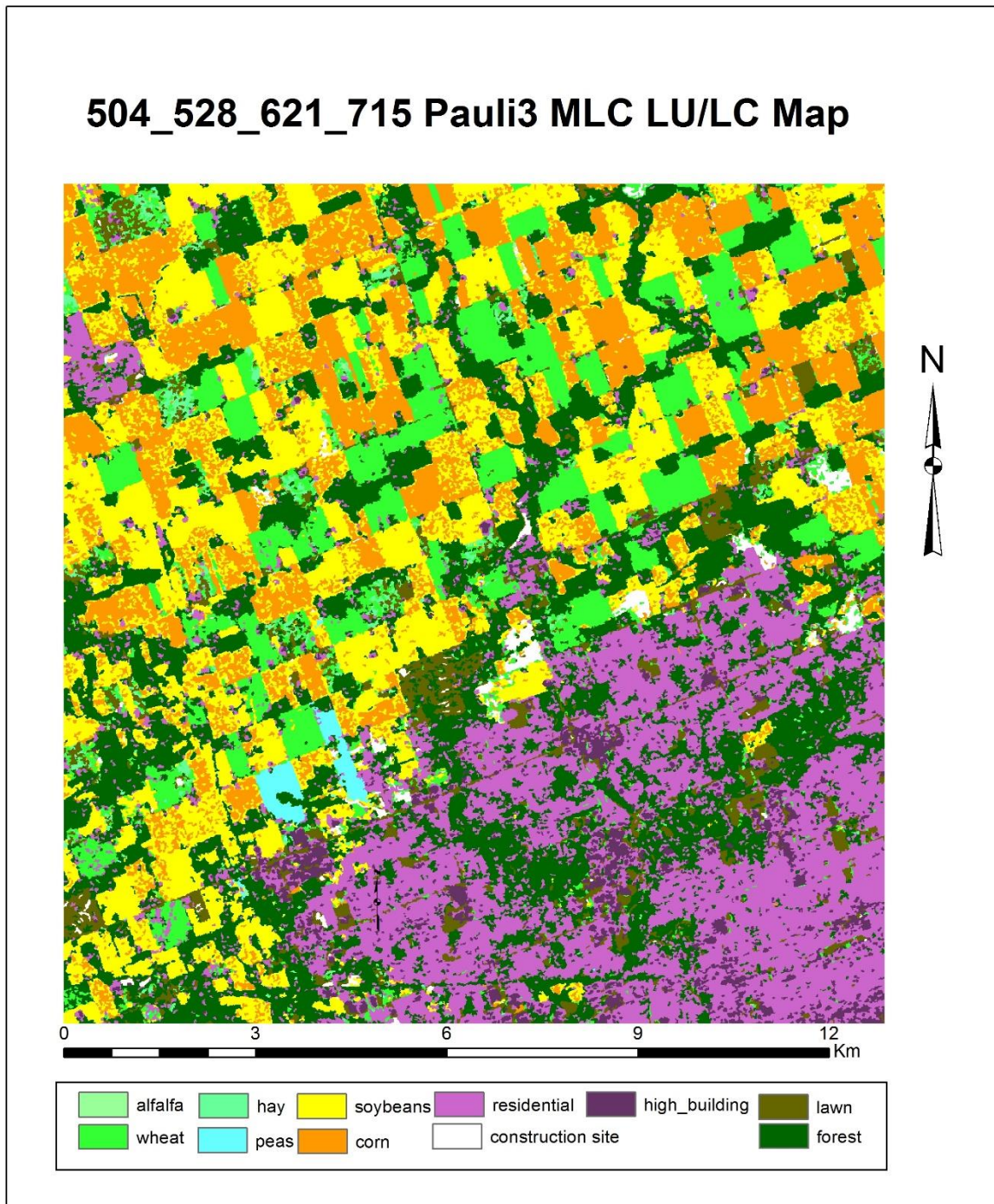
Figure C.2 classification map for Gaussian MLC using Pauli3 elements from May 4, May 28, June 21, and July 15 images

Table C.5 Error matrix for Gaussian MLC using Freeman Durden elements from May 28, June 21, and July 15 images

class	Hay	wheat	peas	soybeans	corn	built-ups	CS	forest	lawn	UA
				Reference Data						
Hay	56	109	0	0	4	12	20	15	9	25%
wheat	20	578	0	2	0	87	45	5	19	76%
peas	0	0	69	0	0	3	0	13	0	81%
soybeans	0	14	0	1511	615	2	1	34	1	69%
corn	0	4	0	333	1507	2	1	2	1	81%
built-ups	0	11	4	1	7	1516	14	132	9	89%
CS	0	0	0	12	6	0	84	0	0	82%
forest	0	18	0	0	4	184	0	737	1	78%
lawn	6	21	0	0	0	46	14	4	173	66%
PA	68%	77%	95%	81%	70%	82%	47%	78%	81%	
OA	0.77		**KP**	0.71						

528_621_715 Freeman MLC LU/LC Sieve Map

Legend:
- alfalfa
- hay
- soybeans
- residential
- high_building
- lawn
- wheat
- peas
- corn
- construction site
- forest
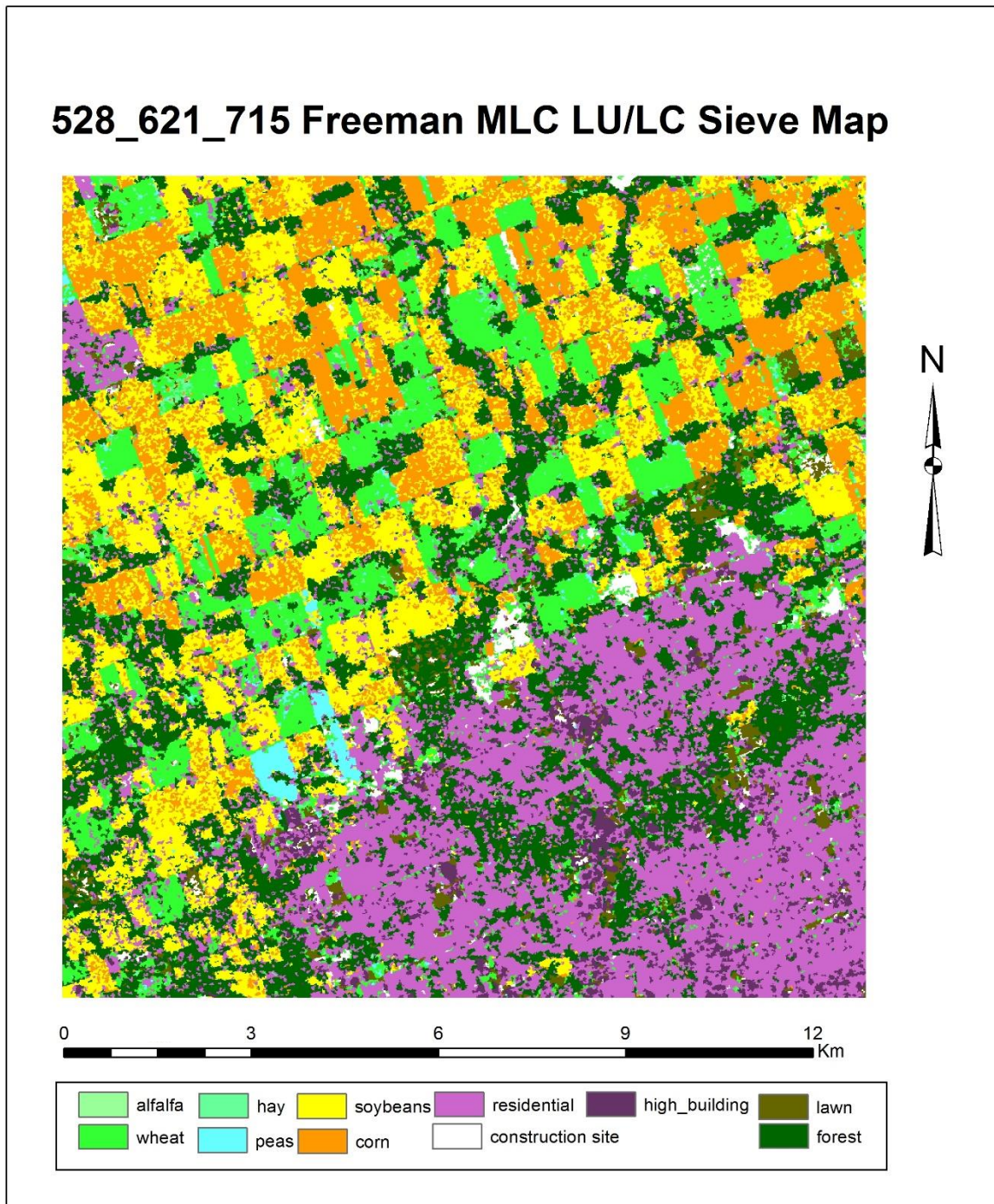
Figure C.3 classification map for Gaussian MLC using Freeman-Durden decomposition parameters from May 28, June 21, and July 15 images

Table C.6 Error matrix for Gaussian MLC using H/Alpha/A elements from May 5, May 28, June 21, and July 15 images

	Reference Data									
class	Hay	wheat	peas	soybeans	corn	built-ups	CS	forest	lawn	UA
Hay	62	2	0	0	0	0	0	3	6	85%
wheat	2	754	0	0	6	17	13	0	0	95%
peas	0	0	72	0	0	0	0	0	0	100%
soybeans	6	0	0	1575	619	0	0	28	14	70%
corn	0	0	0	264	1493	0	0	0	0	85%
built-ups	0	0	0	0	0	1534	4	3	10	99%
CS	5	0	0	1	0	0	154	0	1	96%
forest	0	4	0	3	8	256	9	900	8	76%
lawn	6	0	0	0	0	39	0	0	179	80%
PA	77%	99%	100%	85%	70%	83%	86%	96%	82%	
OA	0.83		**KP**	0.79						

528_621_715 HAlphaA MLC LU/LC Sieve Map

Legend:
- alfalfa
- hay
- soybeans
- residential
- high_building
- lawn
- wheat
- peas
- corn
- construction site
- forest
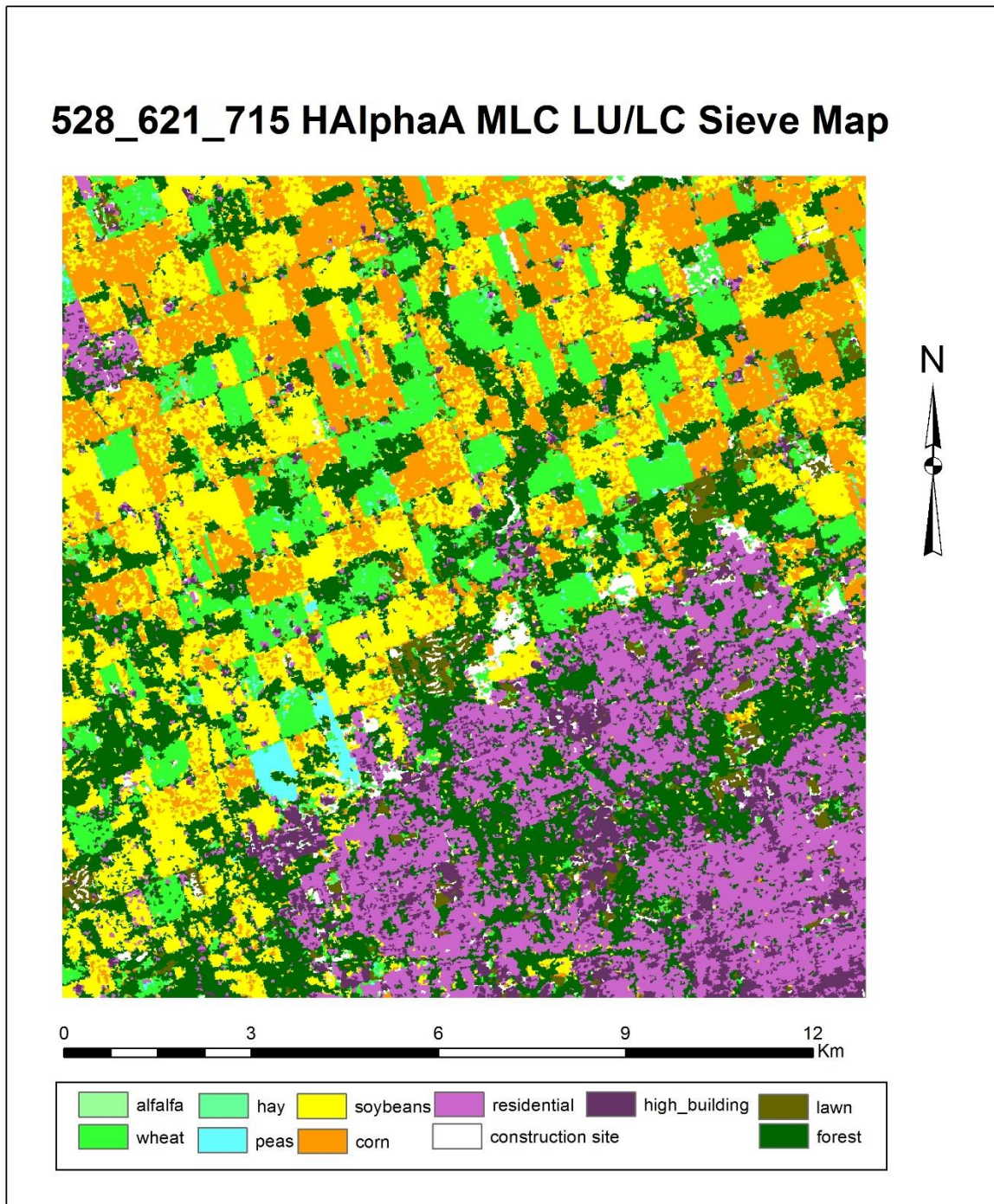
Figure C.4 classification map for Gaussian MLC using H/Alpha/A decomposition parameters from May 28, June 21, and July 15 images

C.3 Time Combinations

Table C.7 Error matrix for Gaussian MLC Pauli elements from May 4, May 28, June 21, July 15 and September 1 five- date images

	Reference Data									
class	Hay	wheat	peas	soybeans	corn	built -ups	CS	fores t	law n	**UA**
Hay	31	0	0	0	0	0	0	0	0	100%
wheat	25	740	12	0	4	5	24	0	7	91%
peas	0	0	56	0	0	0	0	0	0	100%
soybean s	4	0	0	1646	211	6	4	24	6	87%
corn	0	0	0	126	1827	0	0	3	2	93%
built- ups	0	0	0	0	4	1577	11	20	9	97%
CS	2	0	0	0	0	0	131	0	0	98%
forest	0	0	0	0	5	138	1	844	5	85%
lawn	11	0	0	0	0	24	0	0	180	84%
PA	42%	100%	82%	93%	89%	90%	77%	95%	86%	
OA	0.91		**KP**	0.89						

504_528_621_715_901 Pauli3 LU/LC Sieve Map

N

	Km
0	3	6	9	12

	alfalfa		hay		soybeans		residential		high_building		lawn
	wheat		peas		corn		construction site				forest
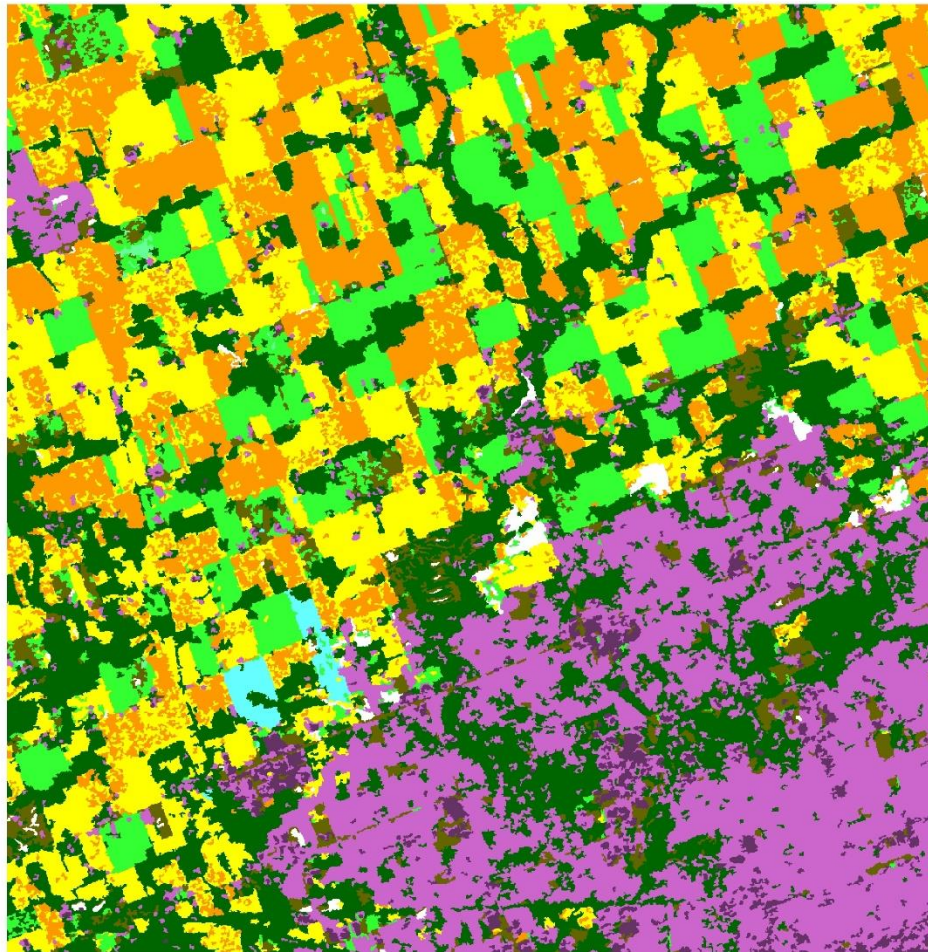
Figure C.5 classification map using Pauli3 from May 4, May 28, June 21, July 15 and September 1 images

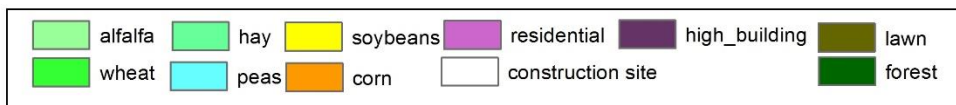**Table C.8 Error matrix for Gaussian MLC Pauli elements from May 4, May 28, July 15 and September 1 four-date images**

class	Hay	wheat	peas	soybeans	corn	built-ups	CS	forest	lawn	UA
Reference Data										
Hay	33	0	0	0	0	0	0	0	3	92%
wheat	13	740	13	0	1	1	7	0	0	95%
peas	0	0	55	0	0	0	0	0	0	100%
soybeans	3	0	0	1617	269	0	21	27	9	83%
corn	1	0	0	155	1768	0	13	0	0	91%
built-ups	0	0	0	0	7	1540	8	11	4	98%
CS	2	0	0	0	1	0	121	0	0	98%
forest	0	0	0	0	5	184	1	853	9	81%
lawn	21	0	0	0	0	25	0	0	184	80%
PA	45%	100%	81%	91%	86%	88%	71%	96%	88%	
OA	0.89		**KP**	0.87						

504_528_715_901 Pauli3 LU/LC Sieve Map

N

alfalfa	hay	soybeans	residential	high_building	lawn
wheat	peas	corn	construction site		forest

0   3   6   9   12 Km

Figure C.6 classification map using Pauli3 from May 4, May 28, July 15 and September 1 images

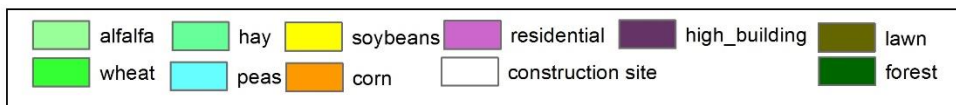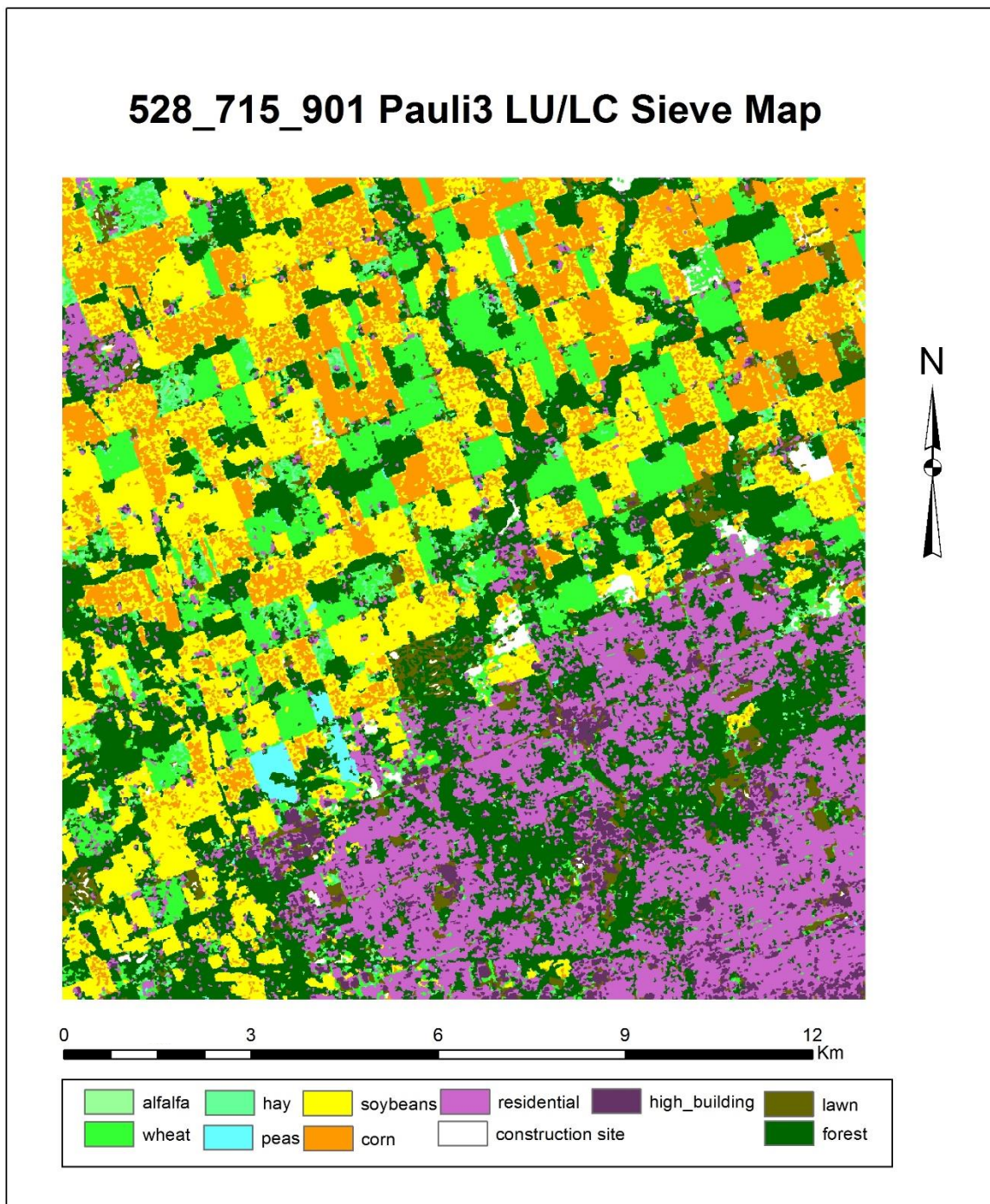**Table C.9 Error matrix for Gaussian MLC Pauli elements from May 28, July 15 and September 1 three-date images**

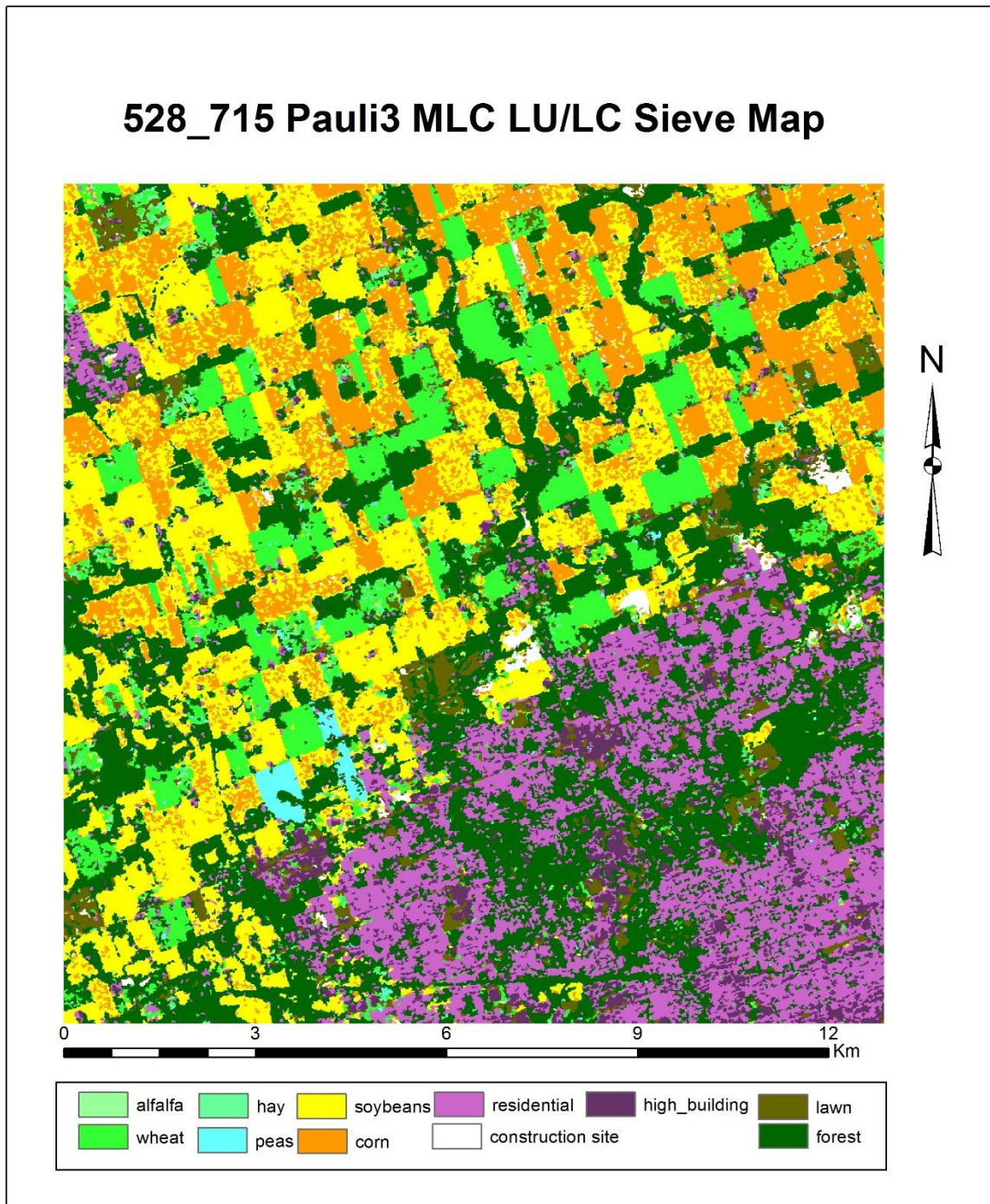| class	Reference Data									
	Hay	wheat	peas	soybeans	corn	built-ups	CS	forest	lawn	UA
Hay	43	0	0	0	0	0	0	2	7	83%
wheat	4	732	0	0	5	5	23	0	0	95%
peas	0	0	68	0	0	0	0	0	0	100%
soybeans	8	0	0	1553	396	0	17	27	15	77%
corn	0	0	0	219	1636	0	3	0	0	88%
built-ups	0	0	0	0	2	1479	4	7	3	99%
CS	5	0	0	0	1	0	121	0	0	95%
forest	0	2	0	0	11	226	3	855	6	78%
lawn	13	6	0	0	0	40	0	0	178	75%
PA	59%	99%	100%	88%	80%	85%	71%	96%	85%	
OA	0.86		KP	0.83						

Figure C.7 classification map using Pauli3 from May 28, July 15 and September 1 images

Table C.10 Error matrix for Gaussian MLC Pauli elements from May 28 and July 15 images

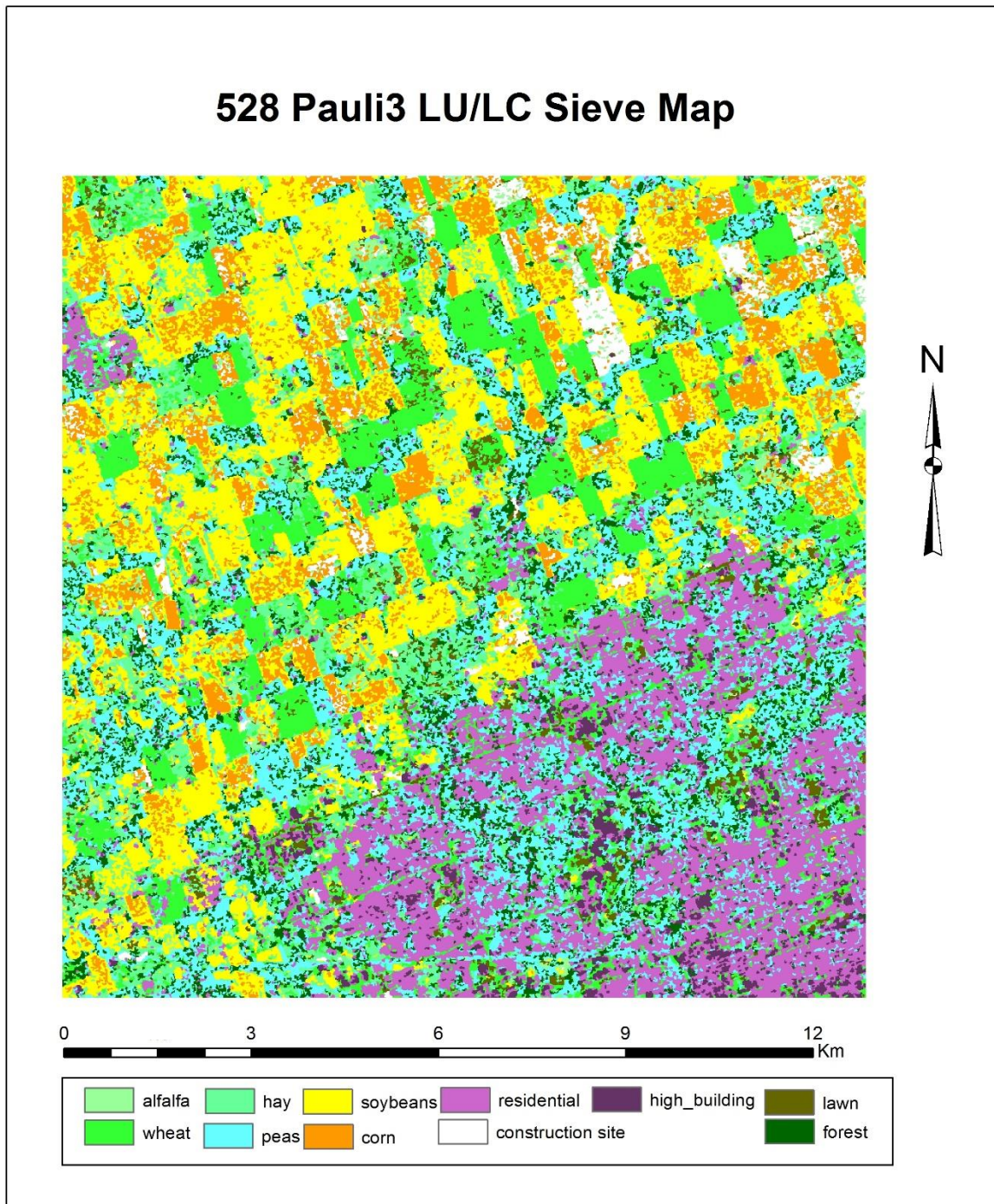| class	Hay	wheat	peas	soybeans	corn	built-ups	CS	forest	lawn	UA
				Reference Data						
Hay	58	9	0	0	0	0	0	0	10	75%
wheat	9	706	0	0	0	0	10	0	0	97%
peas	0	9	72	0	0	0	0	0	0	89%
soybeans	0	0	0	1556	711	0	6	21	15	67%
corn	0	0	0	287	1681	0	0	0	0	85%
built-ups	0	0	0	0	0	988	0	0	0	100%
CS	0	0	0	15	3	0	143	0	0	89%
forest	0	6	0	1	0	80	0	677	0	89%
lawn	12	35	0	0	0	11	0	0	136	70%
PA	73%	92%	100%	84%	70%	92%	90%	97%	84%	
OA	0.83		**KP**	0.78						

Figure C.8 classification map using Pauli3 from May 28 and July 15 images

Table C.11 Error matrix for Gaussian MLC Pauli elements from May 28 one-date image

class	Hay	wheat	peas	soybeans	corn	built-ups	CS	forest	lawn	UA
Hay	46	14	0	197	126	4	7	2	50	10%
wheat	8	711	0	4	0	79	0	0	6	88%
peas	0	0	57	0	0	57	0	452	0	10%
soybeans	4	0	0	1332	932	0	80	19	1	56%
corn	0	0	0	220	981	0	45	2	0	79%
built-ups	0	0	0	2	0	903	0	29	0	97%
CS	5	0	0	88	350	0	27	0	0	6%
forest	0	0	15	0	0	29	0	194	0	82%
lawn	16	40	0	16	6	7	0	0	104	55%
PA	58%	93%	79%	72%	41%	84%	17%	28%	65%	
OA	0.60		KP	0.51						

The header above the class rows spans: **Reference Data**
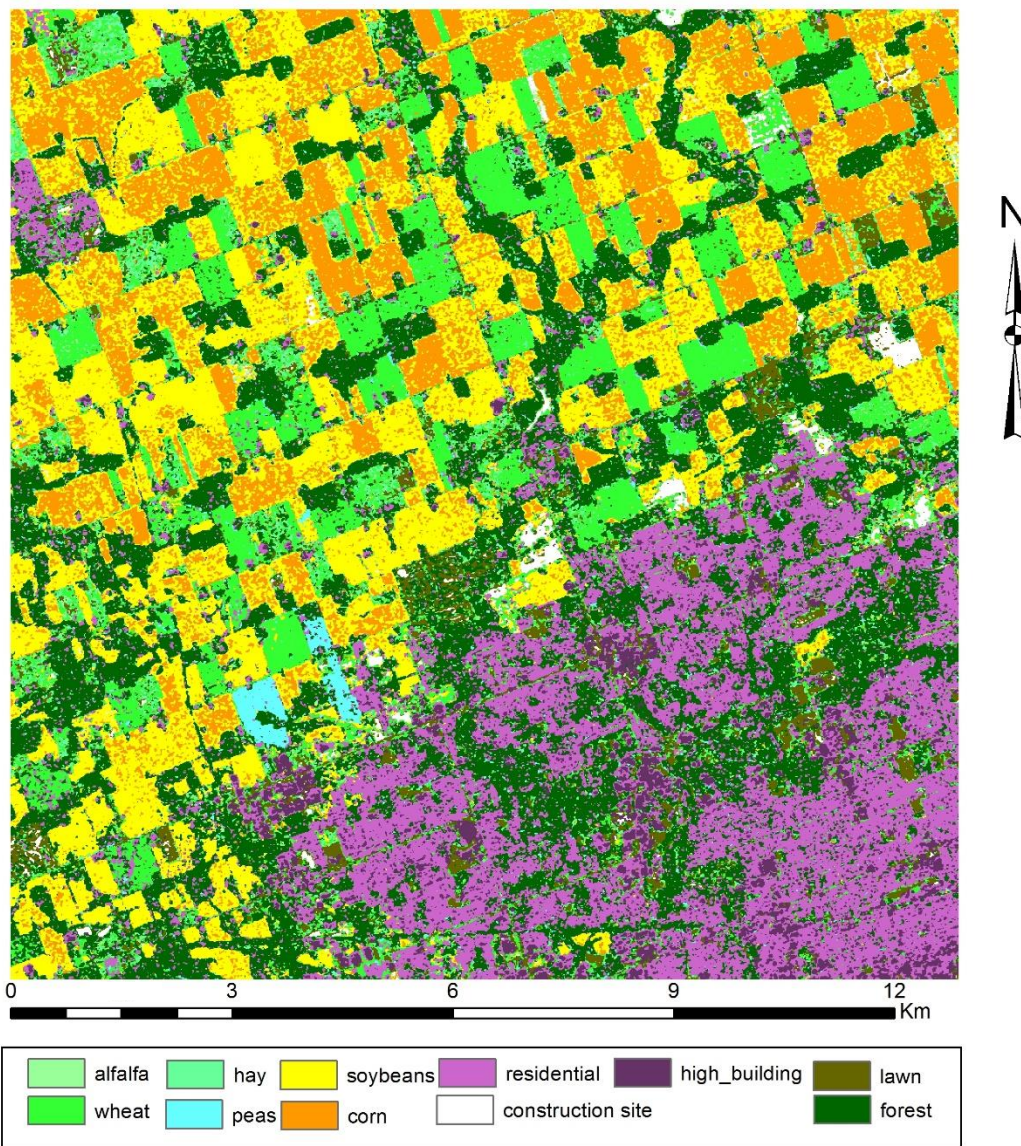
Figure C.9 classification map using Pauli3 from May 28 images

C.4 Post-classification Processing

Table C.12 Error matrix for five-date images results without post-classification processing

class	Hay	wheat	peas	soybeans	corn	built-ups	CS	forest	lawn	UA
				Reference Data						
Hay	30	2	0	0	0	0	0	0	0	94%
wheat	17	682	11	0	0	11	20	0	6	91%
peas	0	0	50	0	0	0	0	0	0	100%
soybeans	2	0	1	1429	340	0	0	21	3	80%
corn	0	1	0	211	1841	0	0	1	0	90%
built-ups	0	0	0	0	0	868	10	36	0	95%
CS	4	0	0	2	0	2	107	0	0	93%
forest	1	1	0	0	0	54	0	552	4	90%
lawn	7	1	0	0	0	13	0	0	120	85%
PA	49%	99%	81%	87%	84%	92%	78%	90%	90%	
OA	0.88		KP	0.84						

Figure C.10 classification map May 28, June 21 and July 15 images without any post-classification processing

Table C.13 Error matrix for five-date images results after sieve filtering

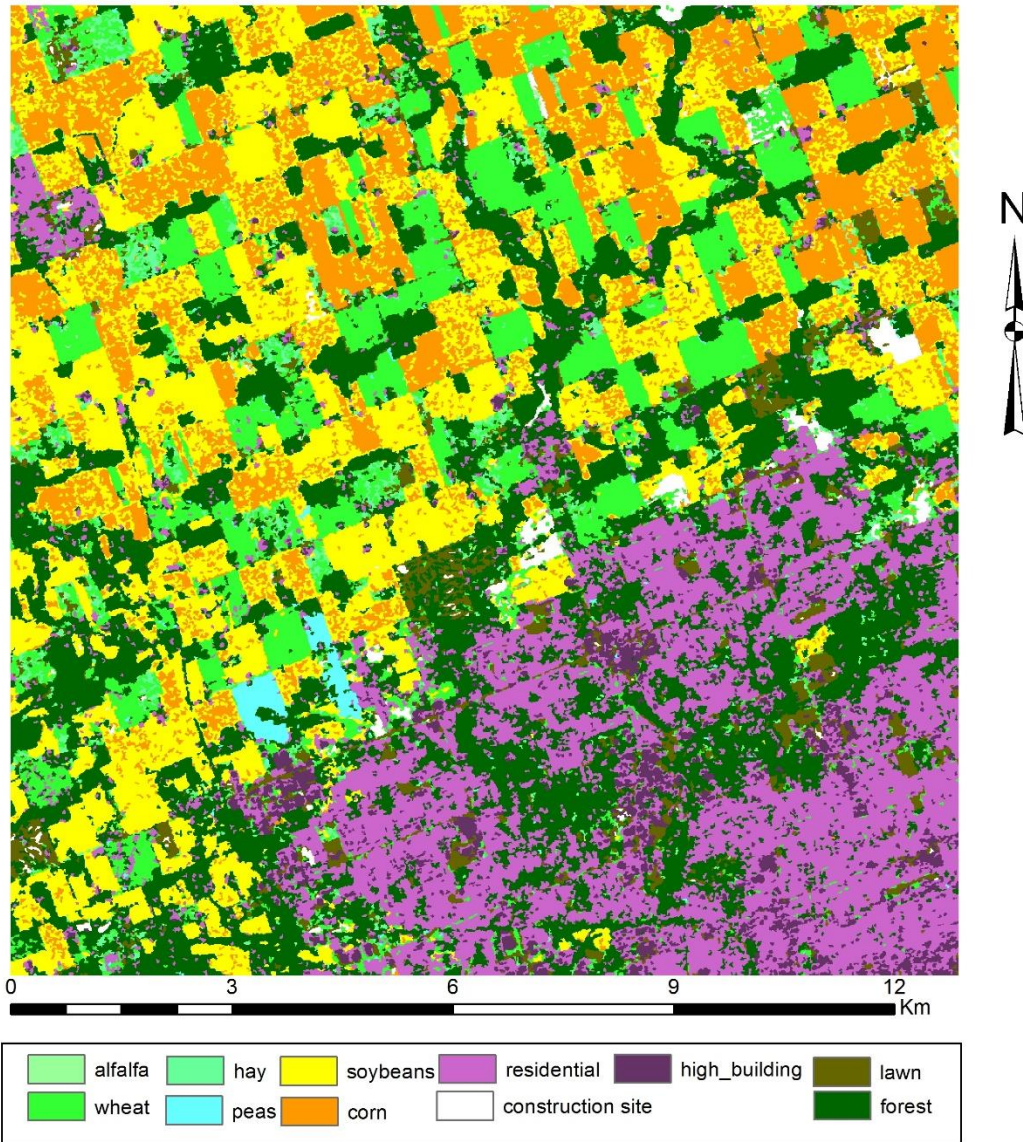| class	Hay	wheat	peas	soybeans	corn	built-ups	CS	forest	lawn	UA
				Reference Data						
Hay	31	0	0	0	0	0	0	0	0	100%
wheat	25	740	12	0	4	5	24	0	7	91%
peas	0	0	56	0	0	0	0	0	0	100%
soybeans	4	0	0	1646	211	6	4	24	6	87%
corn	0	0	0	126	1827	0	0	3	2	93%
built-ups	0	0	0	0	4	1577	11	20	9	97%
CS	2	0	0	0	0	0	131	0	0	98%
forest	0	0	0	0	5	138	1	844	5	85%
lawn	11	0	0	0	0	24	0	0	180	84%
PA	42%	100%	82%	93%	89%	90%	77%	95%	86%	
OA	0.91		KP	0.89						

Figure C.11 classification map May 28, June 21 and July 15 images after sieving

Table C.14 Error matrix for five-date images results after segmentation

	Reference Data									
class	Hay	wheat	peas	soybeans	corn	built-ups	CS	forest	lawn	UA
Hay	4	0	0	0	0	0	0	0	0	100%
wheat	62	760	0	0	3	0	15	0	0	90%
peas	0	0	72	0	0	0	0	0	0	100%
soybeans	0	0	0	1721	137	0	1	26	16	91%
corn	0	0	0	113	1985	0	0	0	0	95%
built-ups	0	0	0	0	0	1670	4	16	4	99%
CS	5	0	0	0	0	0	160	0	0	97%
forest	0	0	0	9	1	160	0	892	12	83%
lawn	10	0	0	0	0	16	0	0	186	88%
PA	5%	100%	100%	93%	93%	90%	89%	96%	85%	
OA	0.92		**KP**	0.90						
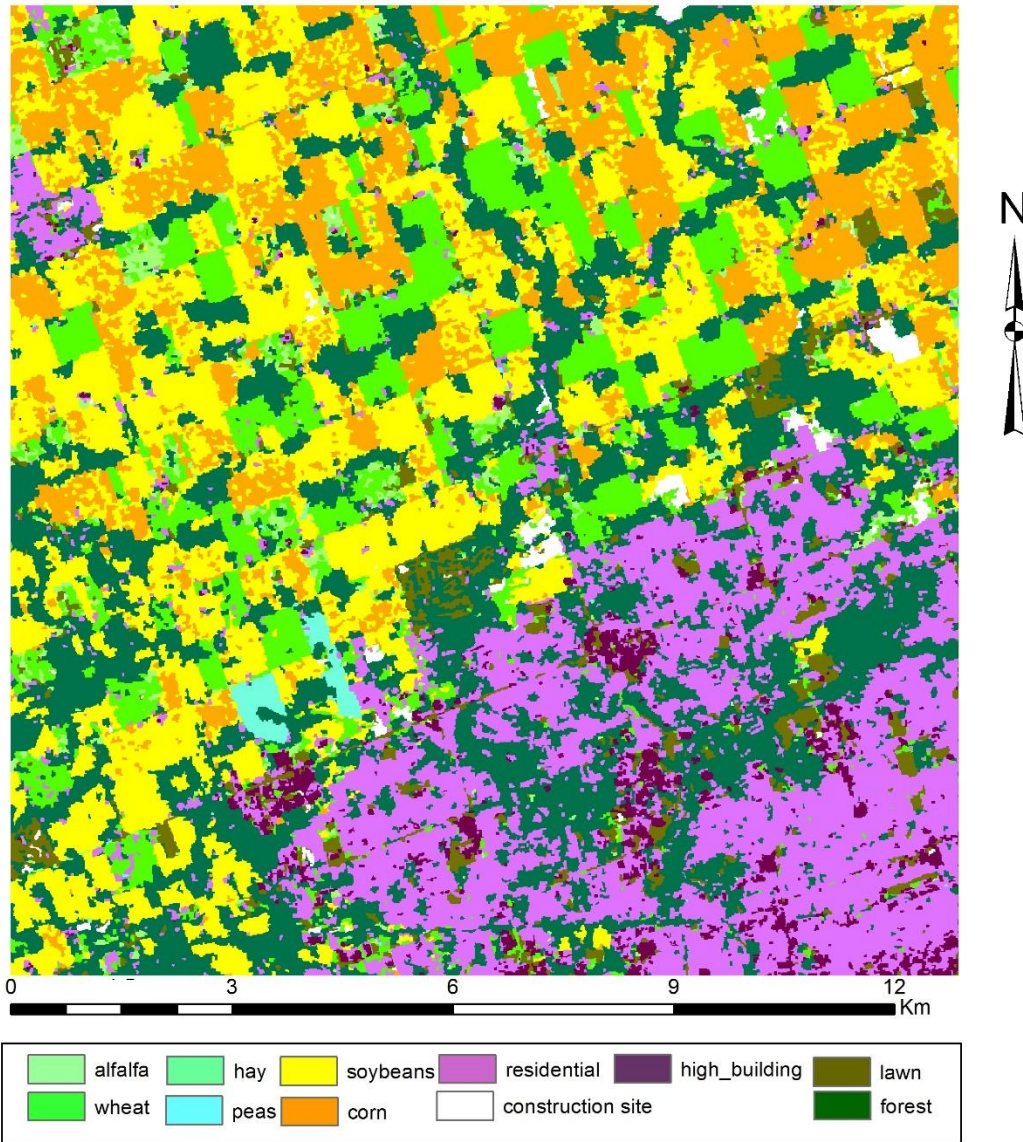
Figure C.12 classification map from May 28, June 21 and July 15 images after segmentation

Curriculum Vitae

Name: Qin Ma

Post-secondary Education and Degrees:

Nanjing University

Nanjing, Jiangsu, China

2007-2011

B.Sc. Geography

The University of Western Ontario

London, Ontario, Canada

2011-2013 M.Sc. Geography (GIS and Remote Sensing)

Honors and Awards:

Western Graduate Research Scholarship,

UWO 2011-2013

Related Work Experience

Teaching Assistant, Research Assistant

The University of Western Ontario, Department of Geography

2011-2013